MODELING AND ANALYSIS OF CONTINUOUS POWDER BLENDING

by

YIJIE GAO

A Dissertation submitted to the

Graduate School-New Brunswick

Rutgers, The State University of New Jersey

in partial fulfillment of the requirements

for the degree of

Doctor of Philosophy

Graduate Program in Chemical & Biochemical Engineering

written under the direction of

Fernando J. Muzzio, Ph.D

Marianthi, G. Ierapetritou, Ph.D

and approved by

_____

_____

_____

_____

New Brunswick, New Jersey

OCTOBER, 2012

ABSTRACT OF THE DISSERTATION

MODELING AND ANALYSIS OF CONTINUOUS POWDER BLENDING

By YIJIE GAO

Dissertation Director:

Fernando J. Muzzio, Ph.D

Marianthi, G. Ierapetritou, Ph.D

The main focus of our research is to investigate continuous powder blending. The unit operation of powder blending is widely used to reduce the heterogeneity degree of product mixture in the manufacture of catalysts, cement, food, metal parts, and many other industrial products. Currently in pharmaceutical industry, continuous powder blending has received more attention as an efficient alternative to the traditional batch blending of powders due to its ability in handling high-flux continuous tablet manufacturing. Numerous previous approaches have been performed focusing on investigating the applicability of continuous manufacturing system. However, the development of reliable industrial system is limited by the inaccuracy of mixing index, the complicated effects of operating conditions and the black-box characterization method, all of which result from the lack of a theoretical model that can quantitatively characterize the whole continuous powder mixing process. Therefore, the overall research objective of this work is to develop

a general standard method for quantitative process design and control. In this context, three different specific aims are accomplished. We analyze and distinguish different heterogeneity sources in the continuous blending process and develop a general model of continuous blending. Fourier series is applied to characterize the axial blending component, and a periodic section model is developed to capture the cross-sectional blending component. Based on the modeling work, efficient design, control, and scale-up strategies applicable for practical blending of pharmaceutical powders are determined. The effectiveness of the methodology is demonstrated in particle blending simulations and experiments using industrial mixing apparatuses to check its applicability and robustness in pharmaceutical industrial use.

ACKNOWLEDGEMENTS

This work was supported by National Science Foundation Engineering Research Center on Structured Organic Particulate Systems, through grant NSF-ECC 0540855, and NSF-0504497. I would not have been able to complete this work without the guidance and resources provided by both my advisors Marianthi G. Ierapetritou and Fernando J. Muzzio. They are always responsible and supportive; teach me a lot not only on academic research activities but also on many other aspects that I believe are very helpful in my future career.

I also would like to thank my committee members: Professor Rohit Ramachandran and Professor Alberto Cuitino for their time, carefully reviewing my work, and providing suggestions. I have had the pleasure to work with several following graduate students and post-docs whom I would like to acknowledge for teaching me particular methods providing helpful advice: Patricia Portillo, Fani Boukouvala, Bill Engisch, Juan Osorio, Atul Dubey, and Aditya Vanarase. Further, I would like to acknowledge the Ierapetritou group for the wonderful friendship we built together during my graduate career.

I want to thank my parents for their unconditional support during my graduate research. Undoubtedly, I would not have been able to get this PhD degree without the support of my wife Yuze Shang. Thank you.

Contents

Lists of tables

List of illustrations

Chapter 1

Introduction

1.1 Batch and continuous powder blending

Powder mixing is widely used in pharmaceutical, cement, food, and other industries in which product mixtures need to satisfy typical performance criteria. In the pharmaceutical processing, a homogenized powder mixture is required to produce tablets with minimum variability, which is critical to meet strict regulatory constraints. This goal is usually realized using batch mixing, which is an easily implemented process in which two or more initially segregated materials are mixed, typically in a tumbling blender. Besides traditional batch methods, continuous mixing has been studied in recent years as an efficient alternative in high flux manufacturing (Marikh et al., 2006).

The role of continuous mixing is to reduce segregation of fluxes that are fed continuously into the system. This process includes two parts (Pernenkil and Cooney, 2006): firstly, two or more initially segregated components mix locally in the radial directions, which is similar to batch mixing. Secondly, axial mixing smoothes out feed rate fluctuations so that the requirement of uniform flowing streams can be met (Williams, 1976). Focusing on the second part, earlier studies of continuous mixers involved the definition of variance reduction ratio (VRR), which was first introduced (Beaudry, 1948; Danckwerts, 1953) as the ratio of variances for the input and output material flow rates in fluid continuous mixing systems. The case of perfect gas mixing was analyzed in a model of a single continuous stirred tank (Danckwerts and Sellers, 1951), where feed rates with regular periodic fluctuations and completely random fluctuations were investigated. In solid mixing, batch

to batch variability reduction was researched on semi-continuous blenders (Goldsmith, 1966). A predictive formula for variability of the output flow was then tested on free flowing non-segregating powders (Williams and Rahman, 1972a, b) where the sampling size was large enough to shield the contribution of local segregation to the experimental output variance. Extension of this formula was also investigated in continuous mixing of segregating powders (Williams and Richardson, 1982) in a fluidized bed, where the variance component of powder segregation was first considered in the prediction of experimental output variance.

Many different types of equipment are available to perform continuous mixing. In fluidized bed mixers, mixing is achieved by the random movement of particles in "gravity free" conditions caused by the pressurized fluid moving upward through the particle medium. Although this process unit is typically used in batch mode, it has been applied in continuous mixing where continuous feeding and removing of powders are desired (Williams and Richardson, 1982). In rotary cylinder mixers(Abouzeid et al., 1980; Sudah et al., 2002a), particles move forward due to the fill level gradient through the cylinder. Mixing takes place around the cylinder surface due to the frictional stress between the surface and the particles (Sherritt et al., 2003), which can be improved when lifters are involved in the process (Geng et al., 2009). Convective continuous mixers are closer in design to rotary cylinders with lifters (Portillo et al., 2008b). They consist of impellers rotating around a shaft, which cause particle displacement to the regions they cannot reach through free flowing movement. While convective mixers can be operated in either batch or continuous mode, different blade configurations and rotary speeds can cause dense or

fluidized particle movement, which makes this kind of mixer suitable in processing both free-flowing and cohesive particles.

1.2 Residence time distribution (RTD)

In chemical engineering and related fields, the Residence Time Distribution (RTD) is defined as the probability distribution of time that solid or fluid materials stay inside one or more unit operations in a continuous flow system. It is a crucial index in understanding the material flow profile, and is widely used in many industrial processes, such as the continuous manufacturing of chemicals, plastics, polymers, food, catalysts, and pharmaceutical products. In order to achieve satisfactory output from a specific unit operation, raw materials are designed to stay inside the unit under specific operating conditions for a specified period of time. This residence time information is usually compared with the time necessary to complete the reaction or process within the same unit operation. For example, in continuous powder mixing processes, powder is mixed in a continuous mixer. The local mixing rate coupled with the time the powder stays inside the mixer determines the unit performance. If the time required for local mixing is longer than the actual residence time powder stays in the system, the process cannot provide a complete mixture, and it fails its designed purpose (Gao et al., 2012). In other words, the performance of any continuous unit operation is determined by the competition of the two sub-processes: a batch process or reaction superimposed by an axial flow. Therefore, the characterization of the RTD in different continuous unit operations is the first step in the design, improvement, and scale-up of many manufacturing processes in the chemical engineering industry.

The research on the RTD in chemical engineering fields has focused on the influence of operation conditions, materials, and the unit geometry on the RTD profile, the improvement of measurement methods, and the improvement of predictive modeling on different processes and units. Most studies investigated continuous unit operations by using the RTD; few extended to the correlation between the RTD and the reaction or process performance, which is usually case-sensitive. For example, a continuous polymer foaming process was studied in an extruder (Larochette et al., 2009), where the thermal decomposition rate of chemical blowing agent was compared with the RTD to investigate the optimization of the foam density; a chemical-looping combustor was investigated in both continuous and batch mode, in which the RTD was used to develop a model for predicting the mass-based reaction rate constant for char conversion (Markström et al., 2010); the production of polypropylene was characterized in a horizontal stirred bed reaction by considering the RTDs of catalyst and polymer separately, which strongly depend on the temporal catalyst activity (Dittrich and Mutsers, 2007); the emulsification process in polymer mixing was studied in a twin-screw continuous extruder, where the RTD and the morphology profile of the mixture was examined simultaneously in one pulse test (Zhang et al., 2009); the Cr(VI) reduction in wastewater treatment was investigated in an electrochemical tubular reactor by applying CFD and velocity profile, where the performance was coupled with the axial flow rate (2010).

Modeling of continuous blending process has received significant attention in the literature mainly through applications of residence time distribution (RTD) theory. These studies were able to model the dispersion of particles along the direction of powder delivery (Danckwerts, 1953). Efforts have been made using RTD as a measure for optimizing

operating conditions in solid mixing in a rotary drum (Abouzeid et al., 1980; Abouzeid et al., 1974) and in a convective continuous mixer (Marikh et al., 2008; Marikh et al., 2005). Several RTD models were introduced characterizing the experimental RTD curves (Nauman, 2008). Delay and dead volume models that linked PFR and CSTR units was used for rotating kilns (McTait et al., 1998), single screw extruders (Yeh and Jaw, 1998) and twin-screw continuous mixers (Ziegler and Aguilar, 2003); the dispersion model based on Fokker-Planck equations with specified boundary conditions were used in rotary calciners (Sudah et al., 2002a), fluidized beds (Harris et al., 2003a, b) and rotating kilns (Sherritt et al., 2003); Markov chains (Harris et al., 2002b; Marikh et al., 2006); and a compartment model (Portillo et al., 2008a) were developed which described granular mixing using a network of interconnected cells based on possible flow patterns inside different mixers.

Due to the wide scope of the RTD issue, every year a large number of papers have been published using this conception in a host of disciplines. A previous review by Nauman (2008) summarized the theoretical development history of the RTD since the beginning of the last century, especially for continuous fluid systems. Some developments have occurred since the previous review.

1.3 Challenges and outline of the dissertation

1.3.1 Lack of predictive model

Studies on continuous powder blending have been mainly focused on the influence of operating conditions (feed rate, impeller speed etc.) and geometric designs (mixer size, impeller types etc.) on the efficiency and throughput of mixers (Pernenkil and Cooney, 2006). One of the earliest studies on continuous mixing addressed the influence of different

types of mixtures on process performance (Harwood et al., 1975). This study investigated the continuous mixing of cohesive and free-flowing particles, which shows that the performance of continuous mixer is determined at least in part by the flow properties of materials. The influence of the agitator design on powder flow has been also studied (Laurent and Bridgwater, 2002), where the velocity profiles of the particle flow were characterized using positron emission particle tracking (PEPT). The influence of stirrer types on mixing heterogeneity was studied for different feed rates and blade speeds (Marikh et al., 2008). Investigation of the effect of different operating conditions on the resulting mixture quality was performed in previous studies (Portillo et al., 2008b), indicating that the cohesive properties of material did not significantly affect the convective mixing performance. Although it is clear that the role of continuous powder mixer is to mix initially segregated fluxes as well as to attenuate feeding fluctuations (Pernenkil and Cooney, 2006), the theoretical basis for design and optimization of continuous mixers, and especially the cross-sectional mixing component, requires additional work. There is still a lack of predictive models of continuous mixing processes that can be used effectively for design and optimization purposes.

As stated above, the effects of the operating factors are complicated and thus difficult to be characterized or predicted. In many of the previous studies, the continuous mixers were considered as black boxes i.e. variables were changed and responses at the outlet were observed. Since this investigating method cannot provide information about the transitional behavior in the process of mixing, questions such as whether radial mixing is complete at the outlet or whether the mixing efficiency is optimized still cannot be answered, which hinders the optimization and control of this process. Due to the black-box

studies, operations empirically optimized in one mixer may not be directly utilized in other mixing cases. This lack of generality has limited the development of systematic design methodologies and control strategies for continuous mixers. For instance, previous studies suggest that better mixing occurs when RTD is broader (Harris et al., 2003a; Marikh et al., 2006; Weineköter and Reh, 1995; Williams and Rahman, 1972a), while an inverse finding is reported based on our prior work (Portillo et al., 2008b) in which we found that the most dispersed RTD corresponds to the worst mixing in a convective continuous mixer, probably due to the low number of blade passes experienced by some of the powder as it travels along the mixer axis. In fact, the main difficulty using RTD as a measure of mixing performance is that it does not consider micromixing of the initially segregated components.

1.3.2 Integration with other unit operations

Based on the RTD theory and the previous studies of variance reduction ratio (VRR), a comprehensive formula of VRR was proposed to summarize the two parts of the continuous mixing process (Ralf Weineköter, 1995). In this formula, the variance of the output mixture consists of the remaining variability that the mixer fails to eliminate in both the axial and radial directions.

Although the VRR is widely used, several previous studies indicate its inaccuracy. Periodic feed fluctuations at different frequency lead to different VRR in the same mixer, indicating that VRR value at a single frequency of fluctuation is not sufficient to thoroughly capture the efficiency of the continuous mixer on smoothing input fluctuations. Furthermore, it is difficult to understand the contributions from either RTD or feed rate fluctuations on the value of the VRR. Little work has been done on quantifying the ability

of the system to filter feed rate fluctuations (Pernenkil and Cooney, 2006), and the relationship between the RTD profile and the filtering ability of the mixer is not clarified. It has been reported that the VRR is dramatically amplified when the input fluctuation is at a higher frequency (Ralf Weineköter, 1995). Moreover, a broader RTD curve results from larger axial dispersion, indicating better mixing performance, which is equivalent to a narrower low-pass filter (Pernenkil and Cooney, 2006). In order to define this filtering ability of the mixer to mitigate input noise as a function of frequency, Fourier series analysis is introduced into this work.

1.3.3 Thesis Objectives

As mentioned above, current limitations and challenges on this issue are inaccurate index, complicated operation and geometry effect, and black-box characterization method, all of which result from the lack of a general-purpose model that can quantitatively characterize the whole continuous powder mixing process. In this thesis, the overall research objective is to develop a general standard method in design and control of the continuous blending process. First, different heterogeneity sources in this process will be distinguished and analyzed separately; based on the analysis, a general model including the processing of different sources will be developed and validated in practical continuous mixing systems. Specifically, the research objectives are as following.

Specific Aim 1: Analysis of different heterogeneity sources in continuous powder mixing process. This aim analyzes and characterizes different variance sources of output mixture in continuous powder mixing process. Models governing both axial mixing and cross-sectional mixing are developed to understand the key factors dominantly affecting each mixing processes. DEM simulations and convective continuous mixing experiments

are performed to determine the influence of the residence time distribution, cross-sectional mixing performance, feeding characterization, operation and geometry, powder properties, and the overall continuous mixing performance. This aim is discussed in Chapter 2

Specific Aim 2: Development of toolbox for continuous powder mixing process. Based on the separated analysis of different variance sources, this research aims to develop a general toolbox characterizing continuous powder mixing process. Decay models of variance components through both axial and cross-sectional mixing are integrated. Strategies regarding optimization of operations and geometry and scaling-up are investigated by estimating the pros and cons of different factor on the two mixing components. This aim is discussed in Chapters 3, 4.

Specific Aim 3: Practical application of the toolbox. This aim tests the developed toolbox into practical continuous mixing processes such as in convective mixers and rotary calciners for industrial purposes. Influence of operations, geometry and powder properties on axial and cross-sectional mixing are separately considered and the overall mixing performance is then estimated by the integration of the separately analyzed processes. In addition, strategies developed in Specific Aim 2 will also be applied to improve the mixing performance, and scale-up the studied apparatuses. This aim is discussed in Chapters 5 -7.

Chapter 2

Characterizing continuous blending performance based on RTD modeling

In this chapter, we developed a general method using the experimentally measured RTD to quantitatively predict the performance of continuous mixing. To distinguish between the variability caused by feeder fluctuations and by the mixer itself, the contributions to the output variance from different sources were separately considered. The rest of the chapter is organized as follows. The experimental conditions and methods are presented in Section 2.1. In Section 2.2, the methods of for fitting RTD parameters, the empirical correlation between RTD and RSD and the variance analysis are presented. Based on the method developed, RTD profiles and mixing performances of several operating conditions are studied in Section 2.3 to test the feasibility of the developed method. Feed rate, blade configuration and rotary speed are studied to quantify their effects on the optimal RTD fitting parameters and the mixer performance. Section 2.4 presents conclusions and discusses the applicability of the proposed method to other configurations.

2.1 Experimental setting

2.1.1 Mixing equipment and materials

RTD measurements were carried out in a GCM 250® convective continuous mixer, provided by Gericke, shown in Figure 2.1. The impeller consists of a cylinder shaft with several blades on each side. The angle of the blades can be adjusted to 20° forward or 20° backward inclination, determining the blade pattern to be investigated. In order to hold the fill level at the desired value, a weir is used to block the lower half of the outlet section. The

rotation speed of the impeller varies between 40 RPM and 250 RPM. Since the critical speed of fluidization is around 180 RPM for this mixer, both a dense-flow regime and a fluidized regime are observed in our studies.

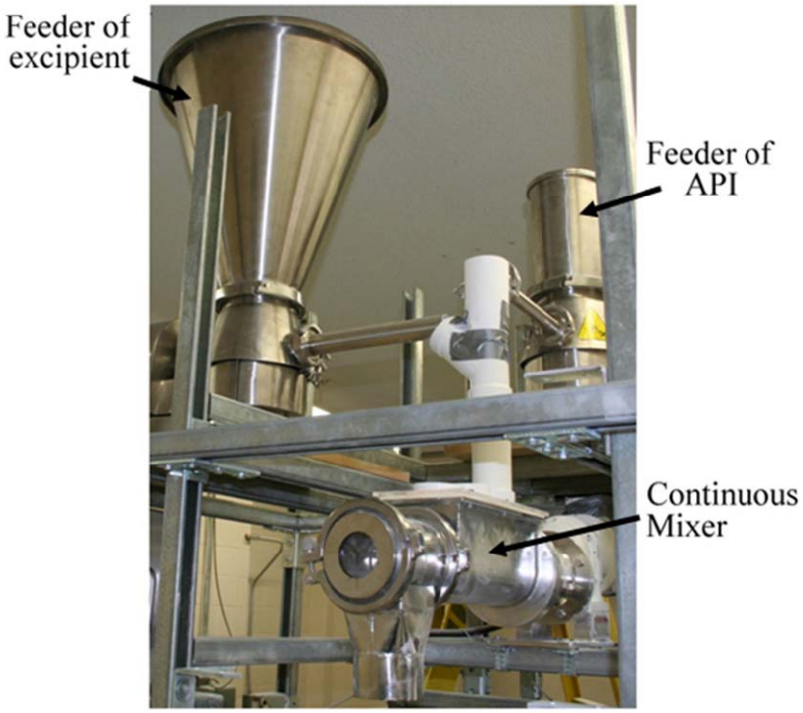

Figure 2.1 Side view of the studied continuous mixing system.

Two loss-in-weight (LIW) feeders provided by Schenck-Accurate are used to feed the mixer. Enough materials were pre-loaded in the feeders so that the experiments were not interrupted or disturbed by re-filling the feeder. The overall feed rates examined include 30 kg/h and 45 kg/h. Acetaminophen (with average particle size of 45μm), pre-blended with 0.25% SiO_2, is used as a representative active pharmaceutical engredient (API) and micro-crystalline cellulose (Avicel PH200, 240μm) is used as the main excipient. The mass fraction of API in this case study is set as 3% for all the operating conditions, which are summarized in Table 2.1.

Table 2.1 Operating conditions.

Operating parameters	
Feed rate	30, 45 kg/hr
Impeller rotation rate	40 RPM, 100 RPM, 160 RPM, 250 RPM
Design parameters	
Blade configuration (Blade angle with the shaft and blade direction)	1. All forward – All blades directing forward, blade angle – 20°
	2. Alternate – Alternate blades in forward and backward directions – 20°

2.1.2 Data collection and analysis of feeder fluctuations

In order to investigate the influence of feed rate variability to the output variance, the feed rate is measured using a catch-scale that records the weight of powder discharged by the feeder as a function of time. More specifically, a container is placed on the catch scale and powder is fed for about 30 minutes. The temporal feed rate of the feeder is then calculated based on the weight increase in the container. The power spectrum for each of the data sets was computed and compared using a MATLAB program, where the variance distribution functions $s(f)$ of the feed rates are calculated at different frequencies. The relationship between $s(f)$ and the overall variance of the feed rate fluctuations σ_{in}^2 is determined by:

$$\sigma_{in}^2 = \frac{1}{2}\int_0^{f_s/2} s(f)^2 df \qquad 2\text{-}1$$

where f_s is the frequency of feed rate measurements. Since the sampling interval is 0.1s for all the feeders, $f_s = 10Hz$. $s(f)$ is integrated between 0 and $f_s/2$ to avoid aliasing, which may introduce error in variance calculation. Note that $s(f)$ represents the contribution from different frequencies to the feed rate variance. Details of this issue can be found in Chapter 3. Figure 2.2 shows the variance distributions of API and excipient feed rates at

different frequencies for the two feed rates studied. The peak of feed rate fluctuations of API shifts from 0.16Hz to 0.24Hz when feed rate is increased. This indicates better feeding conditions, since fluctuations at higher frequency are more easily filtered out by the mixer (Weineköter and Reh, 1995). For the excipient, a sharp peak appears at 1.4 Hz at the lower feed rate, whereas smaller peaks at higher frequencies (starts from 2.1 Hz) characterize the higher feed rate. Notice that the lowest peak of feed rate fluctuations (peak at the lowest frequency) always corresponds to rotating frequency of the feeding screw. The results in Table 2.2 show that the feed rate of 45 kg/hr leads to smaller RSD of API concentration and variance components at higher frequency domains. Since continuous mixer always performs like a low-pass filter through which feeding fluctuations at higher frequencies are easier to be attenuated (Gao et al., 2011b; Pernenkil and Cooney, 2006), these results indicate better feeding performance at feed rate of 45 kg/hr.

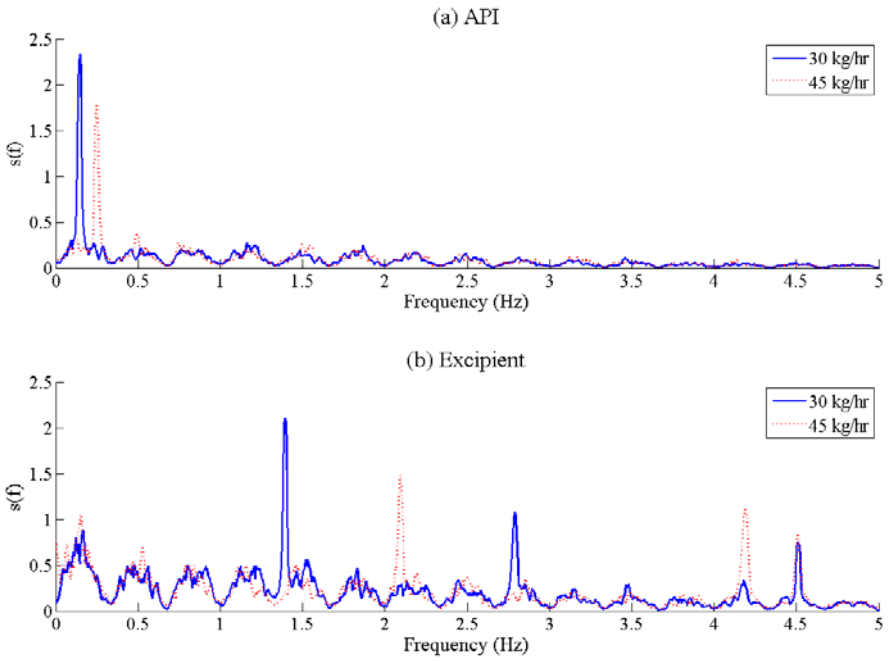

Figure 2.2 Feed rate analysis of (a) API and (b) excipient.

Table 2.2 Statistics of feed rate fluctuations of API at the investigated feed rates.

Feed rate (kg/hr)	API%		
	Average value	Standard Deviation	RSD
30	3.00	1.09	36%
45	3.02	0.64	21%

2.3 RTD and output variance measurement

RTD is measured using the method originally proposed by Dankwerts (1953). Bulk material is fed into the mixer until steady state is reached, and tracer (10 gram of APAP) is injected instantaneously into the inflow stream. Samples are collected at the outlet of the mixer at different time points. The disturbance to the bulk flow caused by the injection of the tracer is assumed to be negligible. Pulse tests are repeated twice at each condition of interest to examine the reproducibility of the RTD. The samples collected are analyzed by NIR spectroscopy to determine the concentration of acetaminophen *C(t)*. The residence time distribution *E(t)* is calculated based on the collected data of *C(t)* using the following equation:

$$E(t) = \frac{C(t)}{\int_0^\infty C(t)dt} \qquad 2\text{-}2$$

To determine the homogeneity of the product mixture, 20 samples are retrieved from the output stream of the continuous mixing process for each operating condition. The concentration of acetaminophen in each sample is measured using NIR spectroscopy, which is used to calculate to the corresponding standard deviation and the relative standard deviation (RSD) as a measure of mixing performance:

$$RSD = \frac{\sigma}{\bar{C}} = \frac{\text{Standard deviation}}{\text{Average concentration}} \qquad \sigma = \sqrt{\frac{\sum_1^N (C_i - \bar{C})^2}{N-1}} \qquad \text{2-3}$$

where $\bar{C}$ is the average concentration of N samples and C_i is the concentration of each sample.

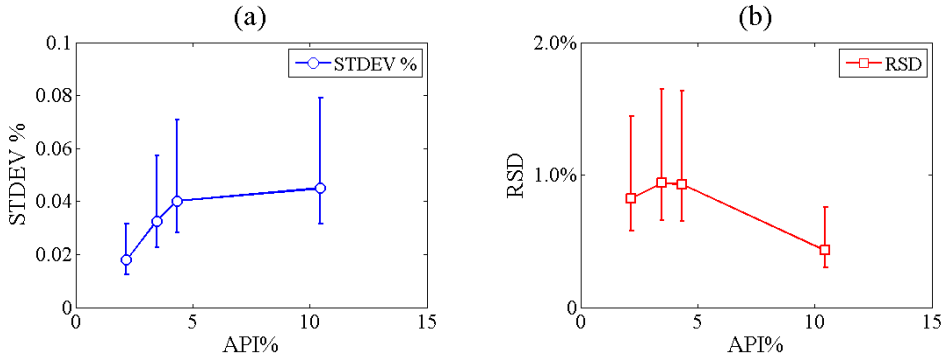

Figure 2.3 Calibration test on NIR method.

(a) Standard deviation (STDEV) (b) relative standard deviation (RSD) was measured at API% of 2%~10% and 95% confidence intervals were estimated.

2.1.4 Analysis of NIR Method Error

In order to investigate the contribution of error in the NIR method to the output variance, the following analysis is performed. Samples of 2%, 3%, 5% and 10% mass fraction of API are prepared to study the measurement variability under the 3% API mass fraction condition. Each sample is well mixed and measured ten times. The same sample is re-agitated before the next measurement so that the scanned surface of the sample is renewed. Standard deviation, RSD and 95% confidence interval are calculated. The results are plotted in Figure 2.3, where the RSD from measurements is found to be around 1% in the studied range of API%, which is insignificant compared to the output RSD

measurement (10%~20%, described in results) obtained in the continuous mixing experiments. As a result, the influence of NIR measurement error can be neglected in the analysis of output variance sources in this study.

2.2 Methodology

2.2.1 General concepts and tools

As indicated in Section 2.1, the variance of the acetaminophen concentrations measured at the mixer output is used as a measure for mixing performance. This measure typically represents two sources of variability: the variability due to fluctuations in powder feeding rate, and the variability of composition due to the non-ideality of the powder mixing process, which is dominant when ideal feeding condition is satisfied. The output variance can thus be expressed as

$$\sigma^2_{output,solid} = \sigma^2_{output,fluid} + \sigma^2_{idealfeed} \qquad 2\text{-}4$$

where $\sigma^2_{output,fluid}$ indicates the variance contribution of unfiltered feeding fluctuations, and $\sigma^2_{idealfeed}$ the contribution due to granular nature of the material (i.e., incomplete transverse mixing, finite number of particles in the sample, agglomeration, segregation, etc) (Weineköter and Reh, 1995). Early studies (Beaudry, 1948; Danckwerts, 1953) describing the variance component due to feeding directly derives variance reduction ratio (VRR) from the convolution of RTD and feeding fluctuations. Although the component of ideal feed was always ignored in these studies due to a cross-sectional sampling size (Goldsmith, 1966; Williams and Rahman, 1972a), it was investigated in a fluidized bed by Williams and Richardson (1982), where mixing of segregating particles was studied and compared

with known or without feeding fluctuations. In our present work, this variance component of ideal-feed is further decomposed as follows:

$$\sigma^2_{idealfeed} = \sigma^2_{ITM} + \sigma^2_{RTDV} \qquad 2\text{-}5$$

where the term σ^2_{ITM} represents the variance component due to incomplete transverse mixing (ITM), and the term σ^2_{RTDV} represents the component due to RTD variability (RTDV). Note that the sample size is supposed to be much smaller than the scale of cross-sectional mixing to ensure that the term σ^2_{ITM} can be detected.

While traditional variance measurements can hardly provide information about the different components of output variance, the characteristics of the RTD can reveal it. In particular, the difference between experimental and model-predicted data, or the data variability in a single RTD measurement is caused by incomplete transverse mixing, which can be used as an indicator of transverse mixing (Figure 2.4a). Low data variability indicates good transverse mixing and homogeneous API concentration in the cross-section of outlet stream. Similarly, the difference between single and multiple model-fitted RTD curves, or model variability in repeated RTD experiments indicates variance due to RTD variability (Figure 2.4b). Small difference indicates good RTD reproducibility, which leads to an insignificant output variance component σ^2_{RTDV}, since little new axial compositional heterogeneity generated in the system through superposition of RTD curves with low variability. This issue was studied in Harris *et al.* (2002a) to validate a proposed method of RTD measurement, where the first three moments of RTD were used in comparison of repeated RTD measurements. It was also investigated in an earlier work (Williams and Rahman, 1972a) in validating the ideal feed condition in a drum mixer. Since quantification of both components correlates to the model fitting process of RTD, a

RTD model that well represents the experimental data is needed to determine these components. In this study, the Taylor dispersion model is selected and described in the following sections.

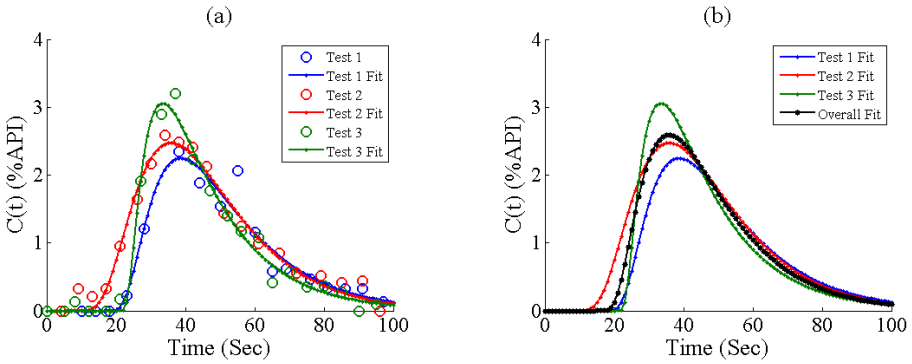

Figure 2.4 (a) Data variability and (b) Model variability of RTD measurements.

2.2.2 Model development

In the original convolution formula of continuous mixing (Danckwerts, 1953)

$$C_{out,fluid}(t) = \int_0^\infty C_{in}(t-\theta)E(\theta)d\theta \qquad 2\text{-}6$$

and $C_{out,fluid}(t)$ are the input and output concentrations. Due to the variance components described in the previous section, a time-variant fluctuation component associated to $E(\theta)$ in equation (2-6) gives the following change:

$$C_{out,solid}(t) = \int_0^\infty C_{in}(t-\theta)(E(\theta)+\varepsilon_E(\theta,t-\theta))d\theta \qquad 2\text{-}7$$

where $\varepsilon_E(\theta,t-\theta)$ represents the fluctuation of measured RTD described in Figure 2.4. Note that this new term sums the effects of data variability and model variability.

Similarly, substituting $C_{in}(t-\theta)$ by the sum of mean and time-dependent fluctuation $\overline{C}_{in}+\varepsilon_{in}(t-\theta)$, results in the following form:

$$C_{out,solid}(t)=C_{out,fluid}(t)+\int_0^\infty(\overline{C}_{in}+\varepsilon_{in}(t-\theta))\varepsilon_E(\theta,t-\theta)d\theta \qquad 2\text{-}8$$

where $C_{out,fluid}(t)=\int_0^\infty C_{in}(t-\theta)E(\theta)d\theta$. Assuming that $\varepsilon_{in}(t)$ is much smaller than $\overline{C}_{in}$:

$$C_{out,solid}(t)\approx C_{out,fluid}(t)+\int_0^\infty \overline{C}_{in}\varepsilon_E(\theta,t-\theta)d\theta \qquad 2\text{-}9$$

Since the variance componnets in the two components of equation (2-9) are independent, the output variance of the concentration equals the sum of the variance components contributed from each of them. Comparing equation (2-4) and (2-9), it is not difficult to conclude that the ideal-feed variance component $\sigma^2_{idealfeed}$ comes from the integration of RTD variability $\overline{C}_{in}\varepsilon_E$.

2.2.3 Solution approach

In order to estimate the time-invariant RTD component *E(θ)* discussed in the previous section, as well as to understand the influence of operations on axial velocity and dispersion, the Taylor dispersion model is considered as follows:

$$\frac{\partial C}{\partial\theta}+\frac{\partial C}{\partial\xi}=\frac{1}{Pe}\frac{\partial^2 C}{\partial\xi^2} \qquad 2\text{-}10$$

Equation (2-10) is the well-known one-dimensional Fokker-Planck equation that describes time evolution of particle distribution in a continuous system (Risken, 1996). Detail of its solution in different initial and boundary conditions can be found in (Levenspiel and Smith, 1957; Sherritt et al., 2003). One commonly used solution of equation (10), known as the Taylor dispersion model, is obtained with open boundary conditions, which was described

in Harris *et al.* (2003a, b) in characterizing the influence of axial gas and solid flux on axial solid Peclet number in fluidized bed:

$$C(\xi,\theta)=\frac{C_0 Pe^{1/2}}{(4\pi\theta)^{1/2}}e^{\frac{-Pe(\xi-\theta)^2}{4\theta}} \qquad 2\text{-}11$$

In equation (2-11) $\theta=(t-t_0)/\tau$ and $\xi=z/l$ are the dimensionless time and location in continuous mixing process, where t_0 represents the effect of time delay in RTD measurement, τ is the mean residence time and l is the overall length of the mixer. C_0 denotes the amount of material injected in the pulse test. $Pe=vl/E$ is the Peclet number, where v and E represent the cross-section averaged axial velocity and the axial dispersion coefficient of the system. When $\xi=1$, equation (2-11) corresponds to the RTD of the mixer.

The parameters Pe, C_0, τ and t_0 in equation (2-11) are determined to minimize the mean sum of square (MSS) error between predicted and experimentally determined values of pulse test. This parameter set is defined as follows:

$$P=[Pe,C_0,\tau,t_0] \qquad 2\text{-}12$$

Fitted pulse test data can then be expressed as $C(t,P)$. In particular, to evaluate the best fitted curve for a single pulse test the follow error is minimized:

$$MSS^2_{j,ITM}=\sum_{i=1}^{n}\frac{[C_{ij}-C(t_{ij},P_{1j})]^2}{n}=\min\sum_{i=1}^{n}\frac{[C_{ij}-C(t_{ij},P)]^2}{n} \qquad 2\text{-}13$$

which represents the MSS error of data variability of RTD due to incomplete transverse mixing. The overall MSS error of repeated RTD experiments is minimized when model fitting of multiple pulse tests are performed:

$$MSS^2 = \sum_{j=1}^{m}\sum_{i=1}^{n}\frac{[C_{ij} - C(t_{ij}, P_1)]^2}{mn} = \min\sum_{j=1}^{m}\sum_{i=1}^{n}\frac{[C_{ij} - C(t_{ij}, P)]^2}{mn} \quad 2\text{-}14$$

In this case the overall MSS represents the error of both data and model variability. In equations (2-13) - (2-14), t_{ij} and C_{ij} represents the pair of time and concentration of the i^{th} point in the j^{th} repeat of RTD pulse tests ($i = 1, 2...n$ and $j = 1, 2...m$). P_{1j} is the optimal parameter set for the j^{th} RTD test leading to the minimized mean sum of square $MSS_{j,ITM}{}^2$, while P_1 leads to the minimized MSS^2 in the multiple RTD fitting process. The relationship between MSS of single and multiple pulse tests is as follows:

$$MSS^2 = MSS_{ITM}^2 + MSS_{RTDV}^2 \quad 2\text{-}15$$

The MSS error evaluated in equations (2-13), (2-14) is then used to determine the expectation of RTD fluctuation ε_E described in Section 3.2. In particular

$$\sigma_E = \frac{MSS}{\int_0^\infty C(t, P_1)dt} = \frac{MSS}{M} \quad 2\text{-}16$$

where $C(t, P_1)$ is the fitted curve of pulse test derived from multiple RTD fitting process, and M represents the total material injected into the system. Based on equation (2-15)

$$\sigma_E^2 = \sigma_{E,ITM}^2 + \sigma_{E,RTDV}^2 \quad 2\text{-}17$$

where $\sigma_{E,ITM}$ and $\sigma_{E,RTDV}$ represent the data variability and model variability of RTD shown in Figure 2.4, respectively.

Based on equation (2-9), the variance of ideal feed is more significant when the expectation of RTD fluctuation (σ_E) is larger, and when this fluctuation lasts longer. Based on this observation, we assume that the RSD, which is the standard deviation divided by the mean concentration, can be expressed as follows:

$$RSD_{idealfeed} = k\sigma_E \Delta T \quad (2\text{-}18)$$

where k is a dimensionless coefficient describing the ratio between sum of RTD fluctuations and the corresponding RSD. ΔT represents the time interval when the RTD data were collected. In order to obtain reasonable ΔT, prolonged RTD measurements were obtained for each operating condition so that all non-zero points can be recorded. Notice that to guarantee this assumed relationship in equation (2-18), both RSD and σ_E should be determined by the sampling size. Using the experimental RTD and RSD obtained under different operating conditions, k can be empirically estimated by applying linear regression of the pairs $RSD_{idealfeed}$ and $\sigma_E \Delta T$. Then the variance components due to incomplete transverse mixing and RTD variability can be derived based on the estimation of k as follows:

$$RSD_{ITM} = k\sigma_{E,ITM} \Delta T \quad (2\text{-}19)$$

$$RSD_{RTDV} = k\sigma_{E,RTDV} \Delta T \quad (2\text{-}20)$$

Based on the estimation of the RSD components, the corresponding variance components can then be conveniently derived using equation (2-3).

2.2.4 Methodology

Based on the theoretical work developed in the previous section, the following procedure of the RTD modeling method can be established.

Step 1: Determine RTD from pulse tests, RSD at the outlet of continuous mixing process ($RSD_{out,solid}$) and feeding samples;

Step 2: Fit RTD using the Taylor dispersion model;

Step 3: Apply the fitted RTD curve as well as the feeding samples to calculate the RSD component of unfiltered feeding fluctuations $RSD_{out,fluid}$;

Step 4: Determine $RSD_{idealfeed}$ based on $RSD_{out,fluid}$ and $RSD_{out,solid}$;

Step 5: Establish the correlation between $RSD_{idealfeed}$ and the form $\sigma_E \Delta T$ which is obtained in the RTD fitting process;

Step 6: Calculate RSD_{ITM} and RSD_{RTDV} and the corresponding variance components, then analyze the effects of operations (feed rate, rotary speed, blade angle etc.) on each of them.

The analysis of step 6 can provide guidelines in order to improve the design and performance of continuous mixing systems. In the next section the proposed procedure was applied in a case study of continuous mixing in order to investigate the influence of different operations to the mixing performance.

2.3 Experimental results and modeling

2.3.1 RTD fitting results

Figure 2.5 illustrates the influence of operating conditions and blade design on RTD characteristics, as obtained experimentally for the materials considered. For each operating condition, pulse tests were repeated twice so that the influence of RTD variability could be included in the performance prediction. The Taylor Dispersion model and the non-linear regression procedure described in Section 2.2 were applied in the RTD fitting process. The curve in each plot corresponds to the best model fit using equation (2-14). It was observed that RTD is more sensitive to blade speed than to feed rate and blade configuration. Lower blade speeds and lower flow rate lead to larger mean residence time and wider RTD. When

feed rate increases from 30 kg/hr to 45 kg/hr, RTD profiles are narrower. This effect is less significant for high speed cases in which the RTD curves are hardly affected by altering feed rate. On the other hand, boarder RTD profiles are observed for the alternating blade configuration other than for the forward blade configuration, the effect of which is more significant at higher blade speeds.

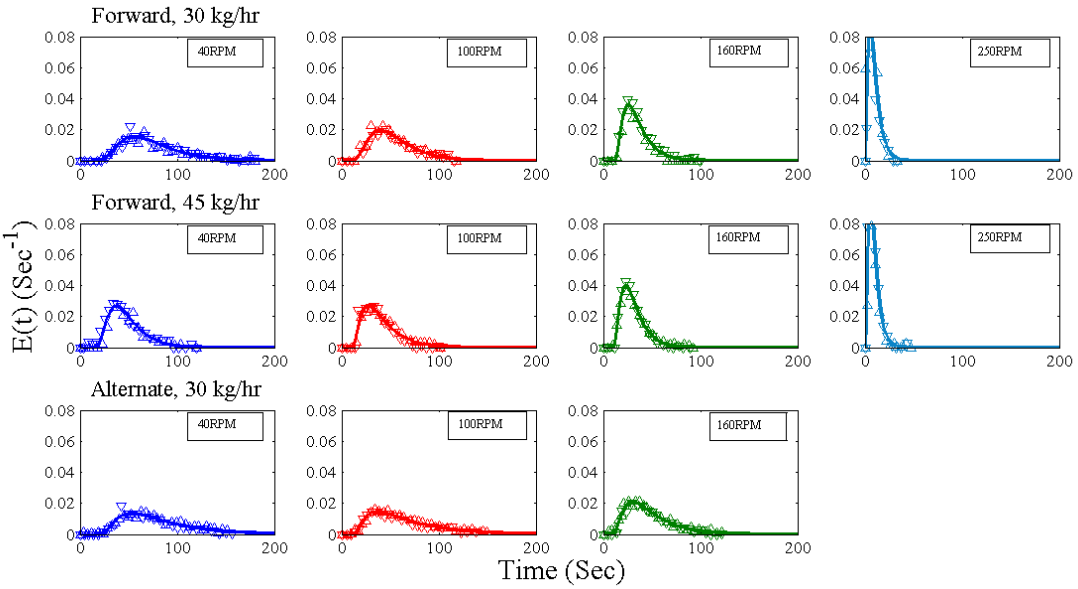

Figure 2.5 Experimental and fitted RTD curve in different operating conditions.

In order to analyze these effects in detail, the optimal axial dispersion coefficient E and axial velocity v derived from P_1 were investigated. As has been examined in several previous studies (Harris et al., 2003b; Sarkar and Wassgren, 2009), particle dispersion coefficient is closely related to fill level and blade rotating speed. Generally, moderate fill level and high blade speed improve axial dispersion (Ingram et al., 2005; Laurent and Bridgwater, 2002; Portillo et al., 2010), while an increase of feed rate or a decrease of blade speed leads to higher fill level (Marikh et al., 2005). The optimal axial dispersion

coefficients at different operating conditions are shown in Figure 2.6a, which indicates that increase of feed rate leads to larger dispersion coefficient at intermediate speed (100RPM), but makes almost no difference when the speed is larger or smaller. At moderate blade speed, the fill level increases significantly at larger feed rate. This behavior is not observed in high rotation speed (250RPM), at which fluidized particles disperse freely for both feed rates and the effect of feed rate on fill level is not significant. Similar observation occurs at low blade speed (40RPM), which is not surprising because limited particle movement severely hinders dispersion; under such conditions the influence of fill level is not significant. Larger dispersion coefficient is also found when the alternate blade pattern is used, which disperses particles better than the forward blade pattern at higher speeds due to the significant increase of backward flux in that blade configuration.

The effects of operating conditions on axial velocity are shown in Figure 2.6b. Axial velocity was found higher at the 45 kg/hr feed rate, and thus led to shorter mean residence time. This is due to the fact that the increase of fill level is slower than the increase of feed rate. This effect is offset at high speed (250RPM) due to the much faster fluidized dispersion. For the same reason as for the dispersion coefficient, limited particle movement at low blade speed hinders the change of axial velocity in different blade pattern configurations. Furthermore, increased backward flux increases the fill level in the alternate blade pattern and further increases mean residence time. Similar effect has been reported in Harris et al. (2003a) on the axial mixing study of fluidized beds, in which the effect of reflux due to the existence of riser at the exit, leads to increased mean residence time and wider RTD curves.

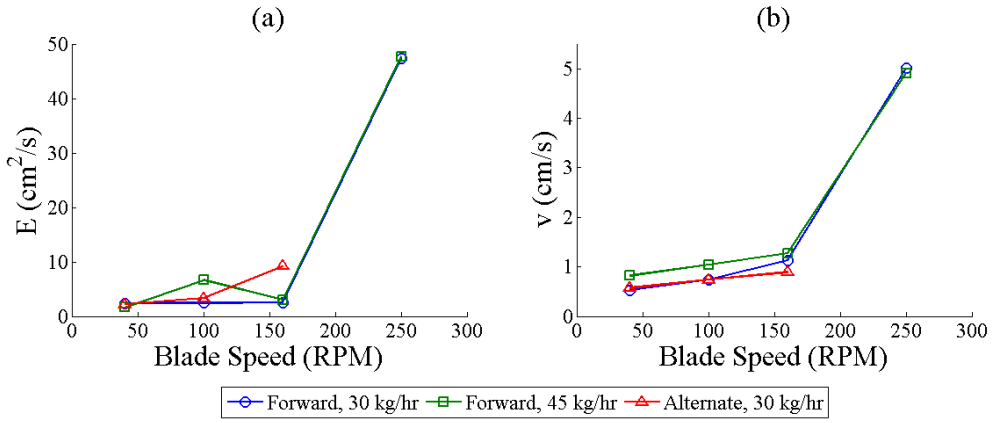

Figure 2.6 Effects of operating conditions on (a) dispersion coefficient *E* and (b) axial velocity *v*.

2.3.2 Results and Discussion

2.3.2.1 Output variance prediction

Based on equation (2-18), k was estimated to be 0.424 using 11 pairs of mixing performance and RTD data corresponding to different operating conditions. The results are plotted in Figure 2.7, in which most predicted values of RSD are located within the 95% confidence interval of the experimental values. A paired t-test ($\alpha = 0.05$) was performed to determine if there is significant difference between predictions and measurements of output RSD. Significant difference is rejected if the two tail p-value is larger than α, or the t-value of the sample size N is smaller than its critical two tail value. The results based on the data in Table 4 shows that the difference between RSD pairs (M =0.091%, SD =3.21%, N =11) is not significant, two-tail p value is 0.927 > α, t(10)=0.094 < two-tail $t_{critical}$ (2.228), providing evidence that no significant difference is observed between the pairs. A 95% confidence interval about the mean difference of RSD is (-2.06%, 2.25%). Although some

differences are observed between the experimental and predicted variance, the predicted values follow the same trends as the experimental measurements. The main sources of variation between predicted and observed values include:

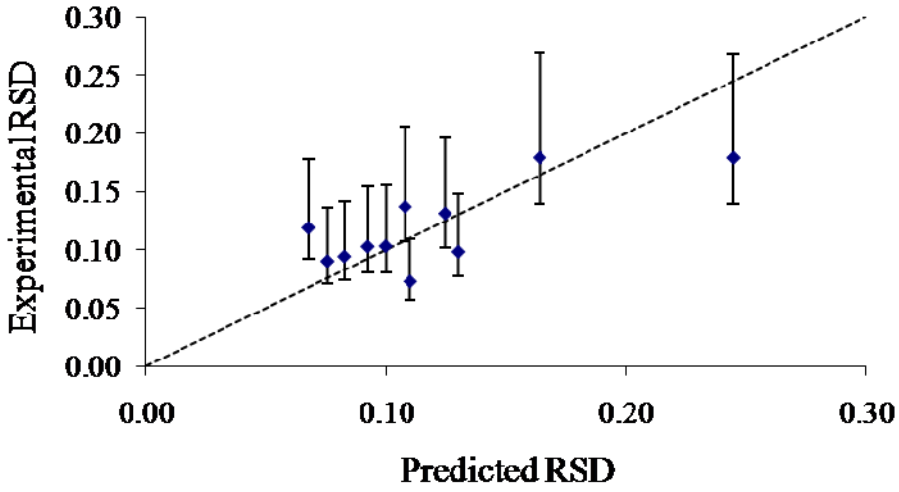

Figure 2.7 95% confidence interval of experimental RSD are calculated and compared to the predicted values.

(1) The term $\varepsilon_{in}(t-\theta)\varepsilon_E(\theta,t-\theta)$, which in equation (2-8) was assumed to be negligible, may contribute to output fluctuations in practice in the examined case study.

(2) In the RTD fitting process, the variance component due to RTD fluctuations was estimated by two repeats of pulse tests. This may introduce non-representative variability on the normalized mean sum of square σ_E and thus lead to deviations on the predicted variance.

(3) The estimated interval ΔT in the RTD modeling process might be too short, which might fail to capture fluctuations occurring outside the recorded tail of the RTD curve.

2.3.2.2 Effect of operating and design parameters

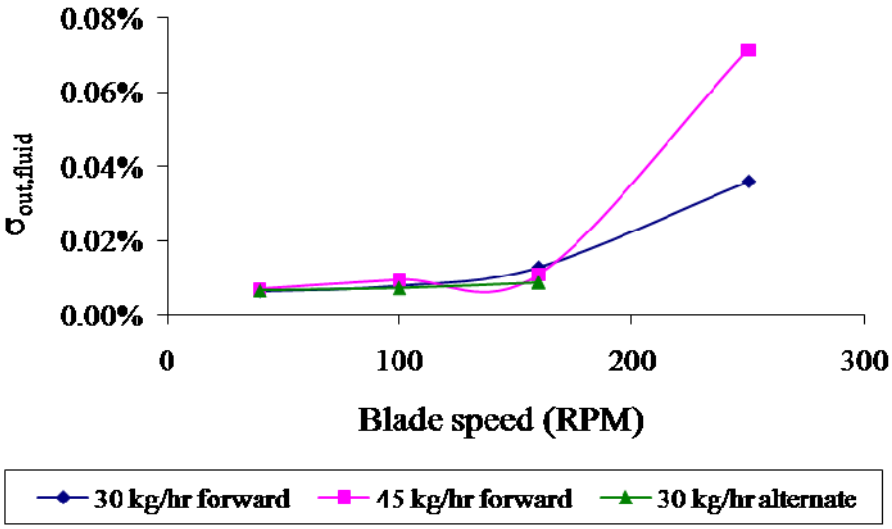

Figure 2.8 Effects of operating conditions on the variance component due to feed rate fluctuations.

The effect of feed rate, blade speed and blade angle on output variance due to feed rate fluctuations, incomplete transverse mixing and RTD variability are plotted in Figures 2.8 to 2.10. In agreement with the RSD results shown in Figure 2.7, under the experimental conditions examined here, the variance component caused by feeder fluctuations shown in Figure 2.8 is insignificant (<0.08%) when compared with the other two components (0.2%-0.8%) and is negligible (< 0.02%) in 40RPM -160RPM, as the mixer filters out most input fluctuations in this range of blade speeds. At 250RPM, the mixer exhibits much worse filtering efficiency at 45 kg/hr than at 30 kg/hr, but the contribution of input fluctuations to the overall variance is still low.

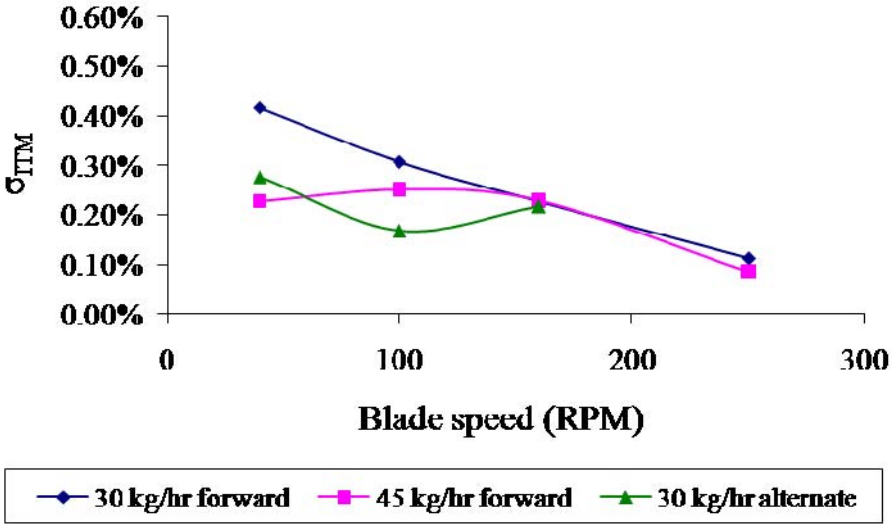

Figure 2.9 Effects of operating conditions on the variance component due to incomplete transverse mixing.

Ingram *et al.* (2005) found that the radial dispersion coefficient increased at high rotating speed and moderate high fill level in rotating drums. In agreement with their previous findings, faster decay of variance component due to incomplete transverse mixing is found here at high blade speed in the studied convective mixer (Figure 2.9). It is also observed that at low blade speed, high feed rate facilitates transverse mixing. This is due to the significant increase of fill level under such conditions, which leads to larger number of blade passes experienced by the powder and results in faster radial dispersion. Mixing is also improved in the alternate blade configuration due to the effect of reflux discussed above. Both effects are offset at high blade speed when the whole mixer is fluidized.

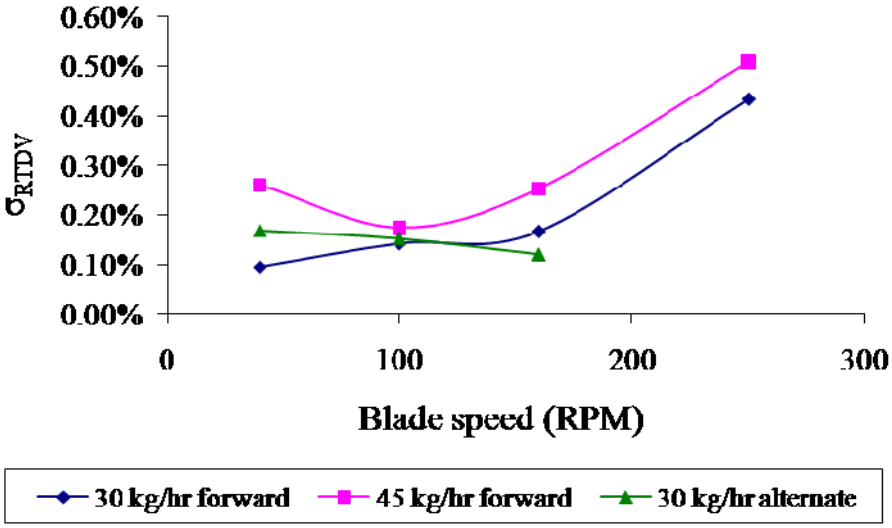

Figure 2.10 Effects of operating conditions on the variance component due to RTD variability.

Figure 2.10 shows the influence of operating conditions on the component of RTD variability. At high blade speed, short residence time and high blade speed lead to highly variable RTD profile and contribute to larger variance component. It is also noticed that high feed rate produces large RTD variability, possibly due to large fill levels and less homogeneous dispersion of particles in the axial direction. Decrease of this component in the alternate blade pattern can be explained by the increase of backward flux that facilitates axial mixing, thus leading to less variable RTD profiles.

Based on the analysis above, the influence of each operating condition on different variance components can be summarized as follows. High blade speed facilitates transverse mixing, but introduces variability on the RTD profile and is inefficient in attenuating feeder fluctuations. High feed rate increases fill level at low blade speed, increasing the number of blade passes during the residence time, which benefits transverse

mixing while results in more RTD variability. Backward mixing produced by the alternate blade pattern improves mixing due to the refluxing effect while leads to less variable RTD profiles at moderate blade speed. In summary, the alternate blade pattern at moderate blade speed generates the most efficient continuous mixing for the materials examined here, while the effects of feed rate on transverse mixing and RTD variability offset each other for the studied conditions, and thus is insignificant to the overall mixing performance.

2.4 Summary

In the present study, we have developed a method based on the experimental RTD for prediction of the mixer performance in a continuous mixing system. Different sources of output variance are separately examined using this method, which leads to better understanding of the effects of operating conditions on each of the individual variance component. Based on the established RTD-RSD correlation, the effects of two feed rates, two blade configurations and four blade speeds are analyzed. The results show that moderate RPM and alternate blade configuration facilitate mixing, while change of feed rate shows no significant influence to the overall output variance. Since the developed methodology is independent of operational conditions, sampling detection method, and mixer type, it should be applicable as a general method to investigate continuous mixing processes. Moreover, the developed variance separation method has an important advantage in understanding the behavior of different variance sources, and thus provides quantitative guidance in further studies in design and control of continuous mixer.

Chapter 3

Axial blending analysis using Fourier series method

Fourier series is a widely used mathematical tool in the applied sciences and has been applied in the field of solid mixing before. The applicability of discrete Fourier transform (DFT) has been tested on characterizing random and ordered solids mixtures (Shin and Fan, 1978). It has also been employed on the autocorrelation function to determine the scale and intensity of time-dependent segregation (Ralf Weineköter, 1995). In this chapter, we develop a general analytical method to characterize the feeder effects on continuous power mixing processes based on the definition of the VRR and the theory of Fourier series. The remainder of the chapter is organized as follows. In Section 3.1, the methodology for practical estimation of the filtering ability of the mixer is presented. The spectrum of fluctuation variance distribution and the filtering ability are defined and derived. A case study of a real feeder-mixer system was explored in Section 3.2 to practically illustrate the application of the method. A dispersion model was used to determine the RTD and the results were applied to the VRR analysis. The chapter concludes in Section 3.3 with a summary and discussion.

3.1 Methodology

3.1.1 Introduction of the variance reduction ratio (VRR)

The earliest formula of the VRR (Danckwerts, 1953) was derived to characterize the fluctuations of continuous fluid mixer:

$$\frac{1}{VRR_{fluid}} = \frac{\sigma_{out}^2}{\sigma_{in}^2} = 2\int\int_0^\infty R(r)E(\theta)E(\theta+r)d\theta dr \qquad 3\text{-}1$$

$$R(r) = \frac{\overline{\delta_{in}(t)\delta_{in}(t-r)}}{\sigma_{in}^2} \qquad 3\text{-}2$$

$$C_{in}(t) = \overline{C_{in}} + \delta_{in}(t) \qquad 3\text{-}3$$

where *R(r)* in equation (3-2) describes the autocorrelation coefficient or serial correlation coefficient. $C_{in}(t)$, expressed as sum of the mean value $\overline{C_{in}}$ and the fluctuation part $\delta_{in}(t)$ in equation (3-3), is denoted as input feed rate. *E(t)* is the normalized residence time distribution, derived from the measured residence time distribution *C(t)* using equation (2-2).

As mentioned, formula (3-1) was designed for fluid mixing. A modification suitable for solid mixing characterization was suggested based on the limited homogeneity of output mixture (Ralf Weineköter, 1995):

$$\frac{1}{VRR_{solids}} = \frac{1}{VRR_{fluid}} + \frac{\sigma_{out,idealfeed}^2}{\sigma_{in}^2} \qquad 3\text{-}4$$

where VRR_{solids} expresses the overall VRR of solid continuous mixing. The fluid mixing part, VRR_{fluids}, indicates the variance from the remainder of feed rate fluctuations that the mixer fails to smooth out. The solid mixing part, $\sigma_{out,idealfeed}^2 \big/ \sigma_{in}^2$, can be represented by the value of VRR under ideal feed rate conditions. In this study, since we focus on the contribution of feeder fluctuations to the output variance, the ideal feed part is not considered in the following sections. Several assumptions necessary for the following Fourier analysis on the fluid mixing formula of VRR are discussed below.

3.1.2 Assumptions for the Fourier series method

The standard form of Fourier series is as follows:

$$f(x) = \frac{a_0}{2} + \sum_{n=1}^{\infty} [a_n \cos(nx) + b_n \sin(nx)], x \in [-\pi, \pi] \quad 3\text{-}5$$

$$a_n = \frac{1}{\pi}\int_{-\pi}^{\pi} f(x)\cos(nx)dx\,;\; b_n = \frac{1}{\pi}\int_{-\pi}^{\pi} f(x)\sin(nx)dx \quad 3\text{-}6$$

where $f(x)$ is a real variable function with period 2π on the interval $[-\pi, \pi]$; a_n, b_n are the coefficients of the n^{th} frequency component of the sine and cosine function series. Using equation (3-5), the variance of the function can be expressed as the sum of squares of a_n and b_n, due to the orthogonal relationships of the sine and cosine functions:

$$\sigma^2 = \frac{\int_{-\pi}^{\pi} (f(x) - \overline{f(x)})^2 dx}{2\pi} = \sum_{n=1}^{\infty} \frac{a_n^2 + b_n^2}{2} = \sum_{n=1}^{\infty} \frac{s_n^2}{2} \quad 3\text{-}7$$

In equation (3-7), the n^{th} frequency variance component of *f(x)* is expressed as half of the corresponding square of frequency intensity $s_n^2 = a_n^2 + b_n^2$. One of the major advantages of equation (3-7) is that it can illustrate the frequency distribution of the feeding fluctuations. In order to apply this analysis into continuous mixing processes, three assumptions are required as follows.

Firstly, the function of residence time distribution *E(t)* is assumed to be time-invariant in the mixing process. This assumption is valid in most cases since residence time distribution is the probability distribution of a large number of particles in the pulse test. In other words, we assume that the fluctuations in composition at the entrance of the mixer do not significantly alter the flow of the powder through the mixer. It is based on the Danckwerts' formula (2-6).

Due to the definition of Fourier series, the periodic function $f(x)$ in equation (3-5) is defined on the interval $[-\pi,\pi]$; however, the definition domains for both $C_{in}(t)$ and *E(t)* are from zero to infinity while both feed rate fluctuations and RTD can only be recorded for finite times in practice. Due to these limitations, another assumption is that the magnitude of *E(t)* is negligible at the end of the RTD measurement. This makes sure that the recorded values can be truncated and transformed onto the interval $[-\pi,\pi]$ without missing significant signal information. Exception to this assumption could occur when the mixer has quasi-stagnant regions exchanging mass very slowly with the main flow. This issue is discussed later in section 3.1.4.

The last assumption concerns the Dirichlet conditions that describe the sufficient condition that guarantees existence and convergence of the Fourier series analysis. Based on this assumption, finite coefficients a_n and b_n in equation (3-6), together with the existence of finite discontinuities, maxima and minima of points in *f(x)*, are sufficient for Fourier series convergence. The Dirichlet conditions should be satisfied on the involved feed rate fluctuations, which guarantees that the reconstructed function based on the Fourier series and the original function of feeder fluctuations are consistent with each other.

3.1.3 Application of Fourier series analysis

Based on equation (3-5), and the assumptions above, the continuous functions of feed rate fluctuations $C_{in}(t)$ and the residence time distribution $E(t)$ in formula (2-6) were transformed onto the interval $[-\pi,\pi]$, and substituted by the corresponding Fourier series. The final output variance and VRR formula of Fourier series are as follows:

$$\sigma_{out}^2 = \pi^2 \sum_{n=1}^{\infty} \frac{(a_n^2 + b_n^2)(A_n^2 + B_n^2)}{2} = \sum_{n=1}^{\infty} \frac{s_n^2 F_n^2 \pi^2}{2} \qquad 3\text{-}8$$

$$\frac{1}{VRR}=\frac{\sigma_{out}^2}{\sigma_{in}^2}=\frac{\sum_{n=1}^{\infty}(a_n^2+b_n^2)(A_n^2+B_n^2)\pi^2}{\sum_{n=1}^{\infty}(a_n^2+b_n^2)}=\frac{\sum_{n=1}^{\infty}s_n^2F_n^2\pi^2}{\sum_{n=1}^{\infty}s_n^2} \qquad 3\text{-}9$$

where a_n, b_n are the Fourier series coefficients of the transformed feed rate $f_{in}(t)$ at the n^{th} frequency component, and the square of the frequency intensity is denoted as $s_n^2=a_n^2+b_n^2$; similarly, A_n, B_n and $F_n^2=A_n^2+B_n^2$ are the Fourier series coefficients and the square of frequency intensity of the RTD function. Due to the expression of VRR in equation (3-9), the filtering ability of the mixer is frequency dependent, expressed by the term $F_n^2\pi^2$. Notice that this filtering ability is not larger than one since amplification of signal fluctuations is impossible in blending process. Comparison between equation (3-1) and (3-9) indicates that the new VRR formula can clearly illustrate the contributions of either feed rate fluctuations or RTD profiles to the output variance of the system, in different frequency domains.

In order to utilize this new VRR formula in practice, we need to introduce the discrete Fourier transform, as continuous records of feed rate and RTD signals with infinite sampling frequency are not available. Moreover, since the scale of the Fourier coefficients is discrete on the frequency domain and thus is proportional to the sample length, it is difficult to compare variance distributions from feeding samples with different length. To solve these problems, procedures are described as follows.

The expressions of discrete Fourier series are shown in equations (3-10) and (3-11), where N is the number of signal points evenly sampled, and x_n is the measured value of each point and X_k is the Fourier component of the k^{th} frequency:

$$X_k = a_k + ib_k = \frac{2}{N}\sum_{n=0}^{N-1} x_n e^{-\frac{2\pi i}{N}kn}, k = 1,2,...N-1 \quad 3\text{-}10$$

$$a_k = \frac{2}{N}\sum_{n=0}^{N-1} x_n \cos\frac{2\pi}{N}kn; b_k = -\frac{2}{N}\sum_{n=0}^{N-1} x_n \sin\frac{2\pi}{N}kn \quad 3\text{-}11$$

$$\sigma^2 = \sum_{n=1}^{N/2}\frac{s_n^2}{2} \quad 3\text{-}12$$

In equation (3-12) the term s_n^2 has the same definition as that of the continuous form in Appendix. By comparing equation (3-10) with the continuous case (3-5), it is found that N is expressed as $N=T_{in}/\Delta t$. Here T_{in} denotes the length of feed rate sample, and Δt is the sampling interval, which reciprocal of the sampling frequency.

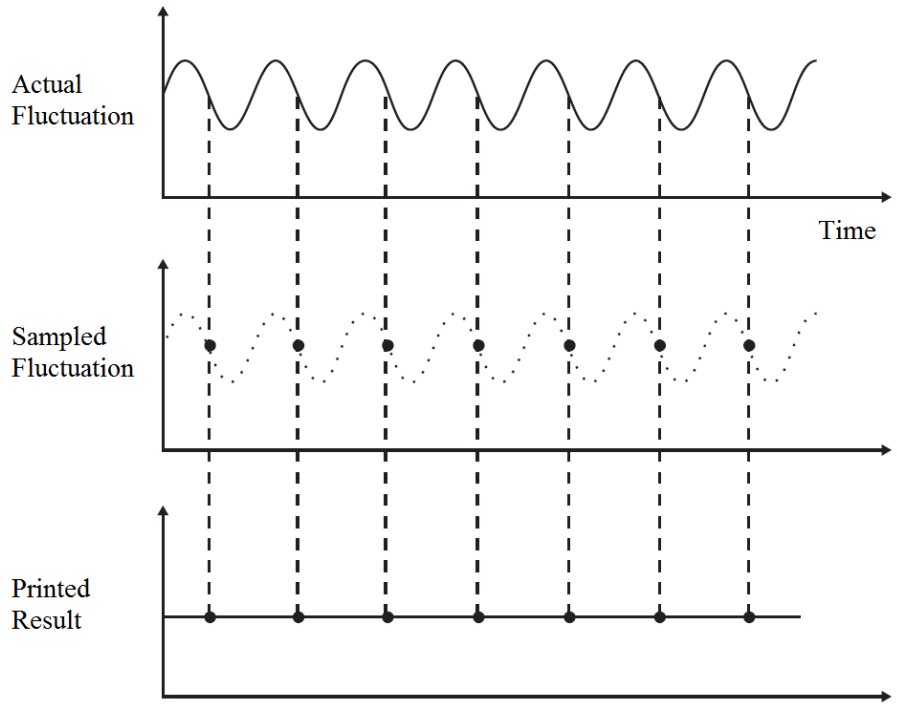

Figure 3.1 Signal fluctuation at sampling frequency may be distorted because of aliasing.

One common problem caused by the discrete manner of the data collection is what is called aliasing in the field of signal analysis, which describes the inaccuracy of fluctuation signal measurement around the sampling frequency (Figure 3.1). To eliminate measurement error caused by aliasing, the maximum frequency component we use in Fourier series is half of the sampling frequency. For example, if the sampling time interval is 0.1s, the sampling frequency is 10Hz, and the maximum frequency we can use in Fourier series calculation is 5Hz. Therefore, the $N/2 \sim N-1$ components are dropped off in equation (3-12).

Equation (3-11) indicates that the magnitude of coefficients a_k and b_k is reciprocally proportional to the number of sampling points *N*. Continuous integration formula instead of sum of squares is thus necessary to avoid inconsistence caused by different *N*:

$$\sigma^2 = \frac{1}{2}\int_0^{f_{\max}/2} s(f)^2 df \approx \sum_{n=1}^{N/2} \frac{s(n\Delta f)^2}{2}\Delta f \qquad 3\text{-}13$$

$$s(n\Delta f) = \frac{s_n}{\sqrt{\Delta f}} \qquad 3\text{-}14$$

In equation (3-14) we introduce the continuous form $s(f)$ instead of the discrete variance component series s_n. Here $\Delta f = 1/T_{in}$ is the minimal frequency interval in the Fourier series, and $f_{max}/2$ denotes half of the frequency of sampling, corresponding to the *N/2* component of the variance intensity. Equation (3-14) represents the continuous variance intensity distribution derived from the discrete series, and the scale of this distribution is independent of how long the input flow is to be tested, or how many points are sampled on the signal of feed rate.

Comparing equation (3-14) with the continuous formula of output variance or VRR in (3-8), we define the ability of a continuous mixer to filter out feed rate fluctuations as *Fe(f)*:

$$Fe(f) = F(f)\pi \qquad 3\text{-}15$$

where $F(n\Delta f) = F_n$ indicates that the magnitude of filtering ability is independent of the number of sampling points. It should be noticed that the coefficient π in equation (3-15) comes from the conversion of time scale from $t \in [0, T_{in}]$ to $x \in [-\pi, \pi]$. If this conversion step is not applied, equation (3-15) is replaced by a general form where $F(f)$ is now directly from the Fourier series of $E(t)$:

$$Fe(f) = \frac{F(f)T_{in}}{2} \tag{3-16}$$

Therefore, we derive the applicable form of output variance and VRR:

$$\sigma_{out}^2 = \frac{1}{2}\int_0^{f_{\max}/2} s(f)^2 Fe(f)^2 df \tag{3-17}$$

$$\frac{1}{VRR} = \frac{\sigma_{out}^2}{\sigma_{in}^2} = \frac{\int_0^{f_{\max}/2} s(f)^2 Fe(f)^2 df}{\int_0^{f_{\max}/2} s(f)^2 df} \tag{3-18}$$

where $s(f)$ is the variance spectrum, and $Fe(f)$ is the filtering ability of the mixer. It becomes clear that for the input variance component $s(f)^2 \Delta f/2$ at a small frequency range $[f - \Delta f/2, f + \Delta f/2]$, a fraction of $1 - Fe(f)^2$ of that variance component will be filtered out by the mixer. This formula shows its merit in clarifying the criterion for design and selection of a mixer or a feeder in an integrated system. Examples of analysis of $Fe(f)$ with different parameters and applications of equations (3-17) and (3-18) will be discussed in detail below.

3.1.4 Correction of the RTD in Fourier series analysis

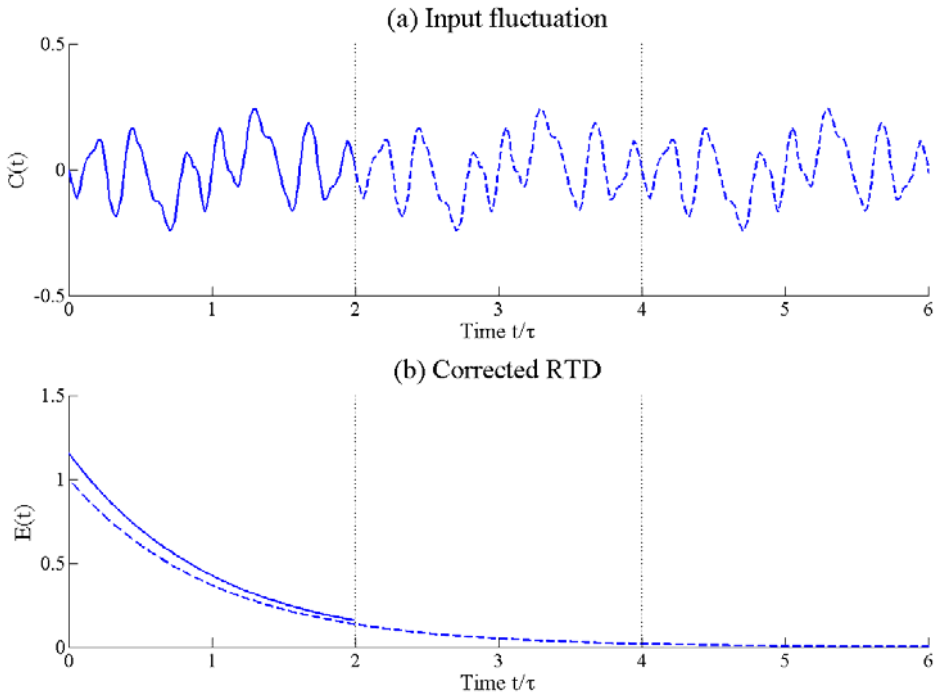

Figure 3.2 The correction of the RTD using the Fourier series.

In Section 3.1.2, we assumed that RTD is negligible on $t \in (T_{in}, \infty)$. However, this is not the case when the tail of $E(t)$ is still significant around the time point $t = T_{in}$. For instance, $E(2\tau)$ equals 0.1353 in the case of one-tank CSTR. If we select $T_{in} = 2\tau$ as the length of feed rate sample, the application of the previous analysis to this RTD will introduce error due to the truncation of the significant RTD tail. The original assumption of negligible RTD tail should be improved to eliminate this problem.

The solution for this problem can be found on the characteristics of the extended periodical function of the Fourier series. Because the feed rate fluctuation sample is assumed to be a periodic function that is extended infinitely (dash line in Figure 3.2a), the output

fluctuation is also a periodic function due to equation **Error! Reference source not found.**:

$$C_{in}(t) = C_{in}(t + iT_{in}), i \in Z \quad 3\text{-}19$$

$$C_{out}(t) = \int_0^\infty C_{in}(t + iT_{in} - \theta)E(\theta)d\theta = C_{out}(t + iT_{in}), i \in Z \quad 3\text{-}20$$

Here the period of the extended functions $C_{in}(t)$ and $C_{out}(t)$ equals the feed rate sample length T_{in}. An equivalent RTD $E'(t)$ that is negligible on the domain $t \in (T_{in}, \infty)$ is created, which leads to the same output periodic function $C_{out}(t)$ as that of the original function $E(t)$:

$$E'(t) = \begin{cases} \sum_{i=1}^{\infty} E(t + iT_{in}), t \in [0, T_{in}] \\ 0, t \in (T_{in}, \infty) \end{cases} \quad 3\text{-}21$$

$$\int_0^\infty C_{in}(t - \theta)E(\theta)d\theta = \int_0^{T_{in}} C_{in}(t - \theta)E'(\theta)d\theta \quad 3\text{-}22$$

The corrected RTD makes it possible to apply the Fourier series even if the assumption of negligible RTD is not satisfied (Figure 3.2). This analysis will be used in the case study.

3.2 Case study on continuous blending data

3.2.1 Taylor dispersion model

The mixing efficiency of RTD is most commonly characterized by its dimensionless second moment of the mean residence time (Nauman, 2008):

$$\sigma_{2nd}^2 = \frac{\int_0^\infty (t - \tau)^2 E(t)dt}{\tau^2} \quad 3\text{-}23$$

where the subscript *2nd* is used to distinguish this metric from the variance discussed in the previous sections. It has been reported that in PFR $\sigma_{2nd}^2 = 0$ and in CSTR $\sigma_{2nd}^2 = 1$, but

little regarding the mixing efficiency has been discussed when the value of σ_{2nd}^2 is between zero and one. In this subsection, the filtering ability index developed in this work is used to characterize the influence of parameters to the filtering ability of the Taylor dispersion model (2-11).

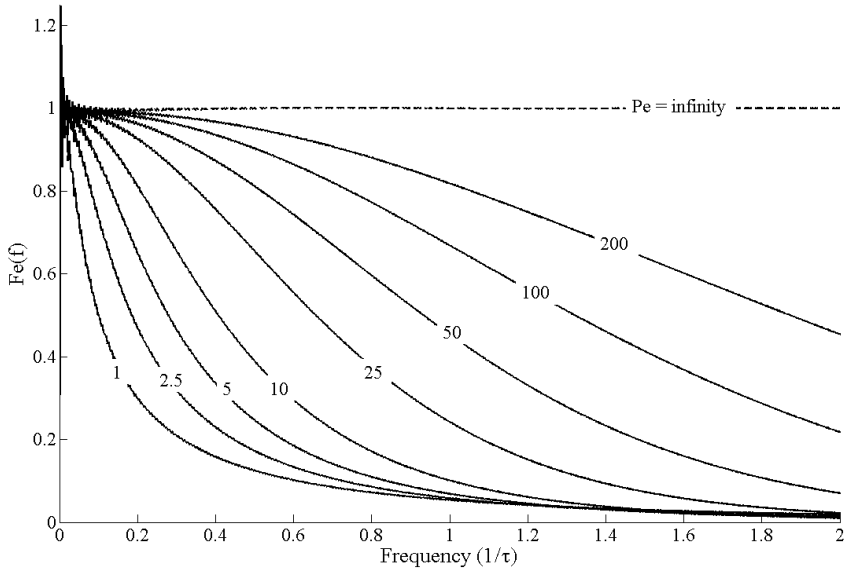

Figure 3.3 Filtering ability of the Taylor Dispersion model with different Peclet numbers from one to infinite.

In this model, the concentration $C(\xi = 1, \theta)$ at the outlet of the continuous mixer is only a function of θ, which can be normalized to deduce residence time distribution with only one parameter *Pe*. The filtering ability *Fe(f)* of the RTD modeled by Taylor Dispersion model are plotted in Figure 3.3, with different Pe. The plots indicate that better filtering ability of the mixer occurs for smaller Pe due to lower and narrower $Fe(f)$ curve. On the other hand, the model acts more like a PFR when Pe is large, in which no smoothing takes place in the mixer. $Fe(f)$ equals one for all frequency components in PFR, while all other curve

profiles with finite Peclet numbers are below it. Figure 3.3 indicates the advantage of the proposed method when compared with the form σ_{2nd}^2.

3.2.2 A real feeder-mixer combination

In this section the developed methodology is applied using data obtained from a continuous feeder-mixer integrated system. Feed rate data $C_{in}(t)$ of excipient (Lactose) and active pharmaceutical ingredient or API, as well as experimental resident time distribution, are collected.

A GCM 250® convective continuous mixer is used, which is operated at a blade speed of 250RPM with all blade angles 20° forward. Two loss-in-weight (LIW) feeders provided by Schenck-Accurate are used to feed the mixer. Acetaminophen (with average particle size of 45μm), pre-blended with 0.25% SiO_2, is used as a representative active pharmaceutical ingredient (API) and micro-crystalline cellulose (Avicel PH200, 240μm) is used as the main excipient. In the continuous mixing process, the mass fraction of API in this case study is set as 3%, and the overall mass feed rate is 66.2 kg/hr. The feed rate variability of API and excipient are separately measured at the corresponding feed rates, using a catch-scale that records the weight of powder discharged by the feeder as a function of time. More specifically, a container is placed on the catch scale and powder is fed for about 30 minutes. With a sampling frequency of 10 Hz, the temporal feed rates of both components $C_{in}(t)$ are then calculated based on the weight increase in the container. Several feed rate samples of 100 seconds are then randomly selected from the 30 minutes record. The continuous variance spectrums $s(f)$ of these samples are calculated. Since no significant difference is observed between these spectrums, a feed rate sample of 100 seconds is long enough to represent the variability characteristics for either API or excipient feeding, and

the feed rate sample measured by the catch-scale is eligible to represent the feed rate fluctuations in real continuous mixing process.

In the correspoding RTD measurement, 10 grams of API is used as the pulse. The feed rate of excipient is equal to the sum of feed rates of the exicipent and the API in the continuous mixing process. After the pulse is injected at the input, samples are manually collected at the output of the mixer at a sampling frequency of 0.25 Hz. The disturbance to the bulk flow caused by the injection of the tracer is assumed to be negligible. As samples are collected, they are analyzed by NIR spectroscopy to determine the concentration of acetaminophen ($C(t)$). The residence time distribution ($E(t)$) is then calculated based on the collected concentration data. To exclude the influence of irregular fluctuations, a curve fitting process is applied on raw RTD data utilizing the Taylor dispersion model. The parameters Pe and τ in the dispersion model are optimized so that the mean sum of square of the residuals between the fitted curve and experimental data is minimized:

$$\min MSS = \sum_{i=1}^{n} \frac{[C_i - C(t_i, Pe, \tau)]^2}{n} \qquad 3\text{-}24$$

where n is the number of measurement points in one RTD test, and t_i, C_i and $C(t_i, Pe, \tau)$ represent the time, experimental concentration and the fitted concentration of the i^{th} point respectively. The fitted curve represented by the optimized set of parameters is used in the developed method.

$E(t)$ and $C_{in}(t)$ obtained in continuous mixing experiments are converted to the filtering ability $Fe(f)$ and the continuous variance spectrum $s(f)$ for both excipient and API. They can be analyzed directly to clarify the performance of the system, and thus provide some guidelines for improvement.

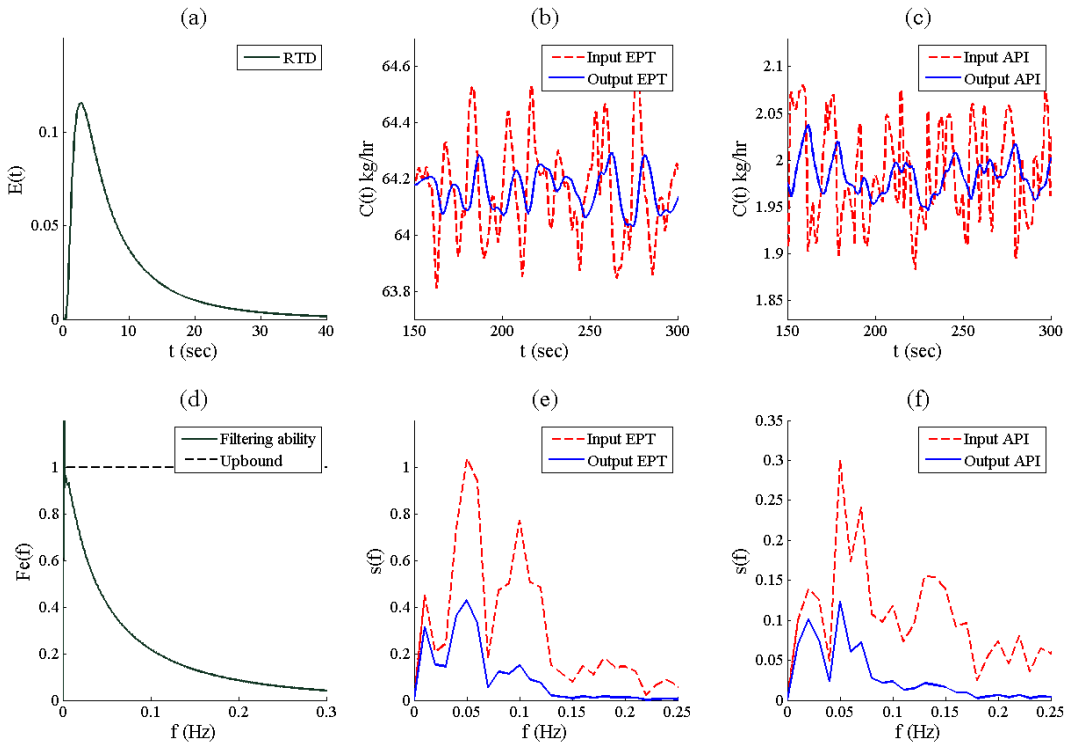

Figure 3.4 Summary of the case study.

(a) Fitted RTD curve, representing the mixer performance in the operation conditions of flow rate 66.2 kg/hr, blade angle 20 degrees forward and rotary speed 250 RPM. (b) Mass flow rate fluctuation of the excipient (EPT) at input and output streams. (c) Mass flow rate of the API. (d) Filtering ability $Fe(f)$ of the fitted RTD curve. (e) Continuous variance spectrum $s(f)$ of the excipient. (f) Continuous variance spectrum $s(f)$ of the API.

In Figure 3.4a the fitted RTD function $E(t)$ is characterized by the optimized parameters $Pe = 1.86$ and $\tau = 9.51\text{sec}$. The filtering ability profile $Fe(f)$ is shown in Figure 3.4d. It is observed that the fluctuations at frequencies higher than 0.25Hz are almost completely filtered out, while below 0.1Hz the mixer is not so efficient at filtering out fluctuations. In Figure 3.4b, c, dashed lines represent the feed rate samples $C_{in}(t)$ of excipient (denoted as

EPT in the figure) and API. The length of of the samples are 100 seconds, as described above. By applying equation (2-6), the fluctuation of the output mass flow rate $C_{out}(t)$ can be calculated (Figure 3.4b, c, solid lines). Notice that since the feed rate samples $C_{in}(t)$ here are not feed rates in real conitnuous mixing experiments, the calculated $C_{out}(t)$ are estimations of the output flow rates. Complete validation of the prediction of $C_{out}(t)$ can be performed only when simutanuous measurements at input and output are available. However, as the feed rate samples and the RTD measurements could represent the feeding and filtering features of the process, the reliability of the unvalidated prediction of $C_{out}(t)$ is guaranteed.

Based on the feed rate samples and output flow rate predictions, a detailed variance reduction profile is illustrated in the continous variance spectum $s(f)$ in Figure 3.4e, f. It can be observed that the output varince component is negligible at frequency larger than 0.25Hz in this case study. For both excipient and API, peaks of fluctuations are significant at 0.05Hz in the input feed rate, while as much as 40% of the peaks survive through the mixing process. In this perspective the system is not in its optimal set. Based on the profile of $s(f)$ and $Fe(f)$, either shifting the peaks of feeder fluctuations to a frequency higher than 0.25Hz, or increasing the filtering ability below 0.1Hz or both improve the efficiency of the system. For instance, the attenuation of the same excipient feed rate sample by alternative RTDs, measured at 160 RPM and 40 RPM rotary speeds, are shown in Figure 3.5. The fitting parameters are $Pe = 14.77$, $\tau = 29.17 Sec$, and $Pe = 7.40$, $\tau = 52.17 Sec$, respectively. Compared with the 250 RPM case in Figure 3.4, it can be seen that better

filtering occurs at the lower rotary speeds. The varaince peak of the feed rate sample at 0.05 Hz is almost completely attenuated due to the small values of $Fe(f)$ at that frequency.

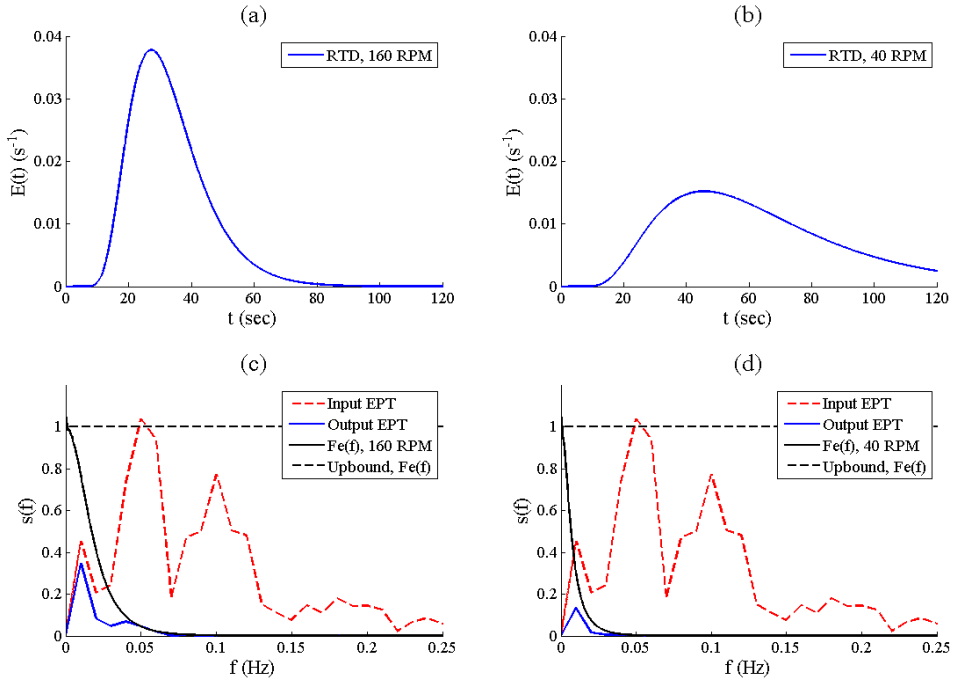

Figure 3.5 Filtering process using alternative RTDs.

(a) Fitted RTD curve at 160 RPM. (b) Fitted RTD curve at 40 RPM. (c) Filtering of variance spectrum by the RTD at 160 RPM. (d) Filtering of variance spectrum by the RTD at 40 RPM. The excipient feed rate sample in Figure 4 is used.

The input, output variance as well as the VRR can be calculated based on the integration of variance spectrums in Figure 3.4e, f. These values can also be calculated based on the traditional time domain method. Results using the two methods are consistent with each other (Table 1), indicating the convergence of the variance spectrum or the assumption of Dirichlet conditions in Section 2.2 is valid in this developed method.

Table 3.1 Validation of case study on the experimental data.

Component		Frequency domain method	Time domain method
Excipient	σ_{in} (kg/hr)	.164	.164
	σ_{out} (kg/hr)	.067	.067
	VRR	6.01	6.02
API	σ_{in} (kg/hr)	.051	.051
	σ_{out} (kg/hr)	.023	.023
	VRR	4.91	4.91

3.3 Summary

In this chapter, the variance reduction ratio was further analyzed by applying Fourier series methods. Input and output variance, as well as the filtering ability of the mixer, were decomposed into different frequency components. The discrete form of the Fourier series was developed. The coefficients of the Fourier series transformation were converted into continuous spectrum which can be easily used to evaluate the system when different feeders and mixers were integrated.

The relationship between the filtering ability and the parameter of the Taylor dispersion model was studied. In the dispersion model, increasing the Peclet number reduces the filtering ability significantly, and extremely large Peclet numbers convert the system into a PFR, where the mixer fails to smooth out any input variability. The derived conception of filtering ability can also be applied in characterizing other RTD models where the influence of model parameters can clearly be estimated. Experimental feed rate and RTD data were used to test the applicability of this method. Based on the developed variance spectrum and filtering ability, the efficiency of the feeder-mixer integration can be evaluated and this provided crucial input for system improvement. Since the feeder

fluctuations that cannot be filtered out are an essential contribution to the overall output variance of the feeder-mixer system, this work provided a novel approach for improving the design and quality control of continuous mixing system for industrial manufacturing.

Chapter 4

Cross-sectional blending analysis using periodic section modeling

To elucidate the cross-sectional blending performance of the continuous mixer, in this chapter we assumes convective continuous blending as a combination of transverse blending and axial movement. Moreover, it is assumed that the mixing process shares similar characteristics as a batch mixing process within any transverse periodic section of the mixer. The axial movement can be characterized by the residence time distribution of the mixer. Thus, mixing along the axis of a continuous mixer composed of a series of periodic sections can be estimated. Non-segregating and segregating particles are used to test this idea. The rest of the chapter is organized as follows: the method, the description of the DEM environment, and the simulation design are presented in Section 4.1. Section 4.2 illustrates the periodic section modeling. Results are discussed in Section 4.3, which shows satisfactory prediction of both non-segregating and segregating continuous mixing processes. We conclude with the applicability of the modeling in Section 4.4.

4.1 Material and method

4.1.1 Periodic section

As indicated in the last chapter, batch mixing inside one periodic section of a convective continuous mixer is used to illustrate the continuous mixing process. The main characteristic of the proposed periodic section is that each particle that exits through one side of the periodic section reenters the section from the other side. This periodicity results in the main advantage of this method in studying the flow pattern of the continuous mixer:

because the volume of the section is smaller than a whole mixer, the approach allows faster simulations with fewer particles, which limits the computational cost. The effects of operating conditions on flow and dispersion of continuous mixing process has been studied based on the utilization of periodic section (Sarkar and Wassgren, 2009). Earlier, this approach was used to increase the resolution of liquid mixing simulations in static mixers (Hobbs et al., 1998; Zalc et al., 2002). Based on these studies, the batch mixing performance of periodic section is discussed here.

In this work, the convective continuous mixing process is regarded as the combination of the batch mixing in one of the periodic sections in the continuous mixer, and its axial movement along the whole mixer. On one hand, the axial movement is consisted of the axial velocity v_x and dispersion coefficient E_x, resulting in a residence time distribution at the outlet; on the other hand, we consider the periodic section as a batch due to the definition of batch mixing, in which no net exit or entrance of particles takes place once mixing starts. Since particles are in the same space through the process, mixing in the periodic section is only a function of time, the same as in batch. Meanwhile, steady state can be reached in a continuous mixer composed of a series of periodic sections. In this case, the distance the powder travels, instead of the time the particles stays inside the batch mixer, can be regarded as the measure of mixing process.

4.1.2 Computational environment

It is difficult to experimentally design a system that allows investigation of the batch-like mixing in a periodic section. Instead, the discrete element method (DEM) is used to simulate the process. DEM refers to a family of numerical methods for computing the motion of large number of particles like molecules or grains of sand, by solving Newton's

equation of motion for each particle. In this work, the software EDEM® from DEM Solutions is the computational environment used to develop the desired geometry and model of particle motion. In this work, particles are modeled as monodisperse spheres, while the contact forces are calculated using the Hertz-Mindlin no slip contact model (Mindlin, 1949). The physical and numerical parameters used in this simulation are summarized in Table 4.1. The values are chosen so that complete mixing can be achieved in the time interval of simulation.

Table 4.1 Physical and numerical parameters used in the DEM model.

Parameter	Value		
	Particle 1	Particle 2	Particle 3
Particle diameter	3×10^{-3}m	2×10^{-3}m	4×10^{-3}m
Particle density	1×10^{3}kg m^{-3}	2×10^{3}kg m^{-3}	0.5×10^{3}kg m^{-3}
Poisson's ratio	0.25		
Shear modulus	3×10^{8}Pa		
Coefficient of restitution	0.5		
Coefficient of static friction	0.5		
Coefficient of rolling friction	0.01		
Simulating time step	10^{-6}s		
Recorded time step	0.01s		
Sampling time interval	0.1s		

4.1.3 Materials, geometry and simulation studies

In order to investigate different mixing behaviors, three kinds of particles with different diameters and densities were used in the simulation (Table 4.1) to investigate how segregating and non-segregating particles influence the relationship between mixing in the periodic section and in the corresponding continuous mixer. In the present study, we investigate two case studies: a first mixture consisting of only particles type 1, having different colors, and a second mixture of particles type 2 and 3. The first case is

representative of a non-segregating mixture, while the second case will result in segregation, where the smaller, higher density type 2 particles will sink downward through the gaps between the larger, lighter type 3 particles.

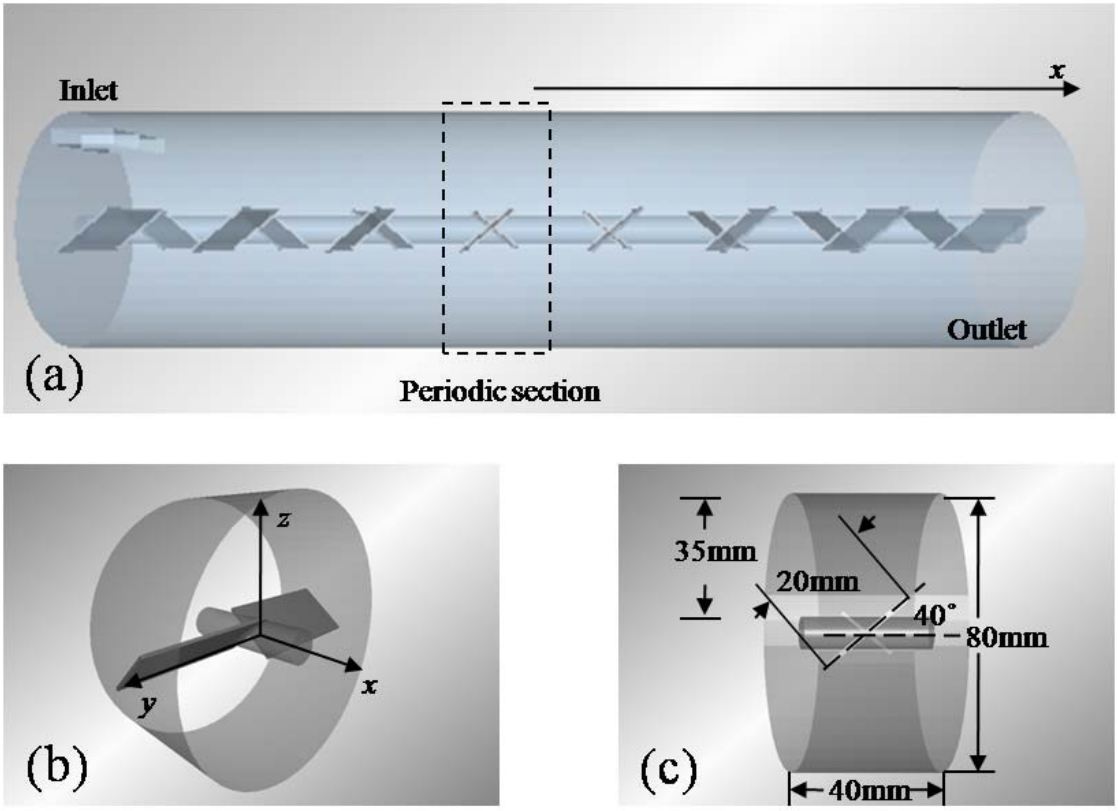

Figure 4.1 Simulated geometry of the mixer composed of eight periodic sections.
(a) Side view of the mixer, blades rotate counter-clockwise and push particles forward along x axis, from the inlet to the outlet, (b) isometric view of one section, (c) side view of one section with displayed dimensions.

To compare the similarity between batch-like mixing in the periodic section and the corresponding continuous mixing in a full blender, simulations of both processes are performed. In the current study, a convective continuous mixer composed of eight sections

with the same geometry was considered. The mixing zone consists of a horizontal cylinder, in which two opposing blades are located on the inner shaft at the middle of each section (Figure 4.1). The detailed geometry of these sections is shown in Figure 4.1b, c. Blades are oriented 40˚ at the cylinder axis to propel particles forward, as well as to mix particles in the transverse directions. Particles are fed side-by-side continuously from the top of the first section, and leave the mixer at the open end on the right side of the last section (Figure 4.1a). The left side of the mixer is closed to avoid material leakage. In steady state, feed rate at the inlet should equals to the flow rate everywhere inside the mixer. As no weir is used at the outlet of the mixer, no backward flux should be observed in the last several sections. This indicates similar flow patterns (all forward) in the continuous mixing case, and in the batch mixing case of the corresponding periodic section. Meanwhile, the absence of weir could lead to much lower fill level in the last two or three sections than the rest. As mixing efficiency depends significantly on fill level (Portillo et al., 2006; Sarkar and Wassgren, 2009), the mixing efficiency in the last several sections should be different from the rest. This will be considered in the development of the periodic section modeling in Section 4.2.

The batch mixing in the corresponding periodic section also needs to be characterized. Notice that the periodic section shares the same geometry with each single section of the full mixer. Instead of feeding continuously at the top of the section, particles are initially loaded side-by-side through the blade shaft (Figure 4.2). This insures that the main compositional gradients at the beginning of the mixing process are in the same transverse direction as the corresponding continuous process where different materials are fed in a similar side-by-side style. The loaded fill level and component ratio in the periodic section

are set to be the same as the steady state continuous mixing. While batch mixing takes place in the periodic section, a net forward flux due to the two forward blades is generated in the mixing space. This leads to flow pattern and mixing condition in the periodic section similar to those in the corresponding continuous case. However, for the periodic section, the time-dependent batch mixing process needs to be converted to a location-dependent continuous process in order to characterize the mixing of the whole mixer.

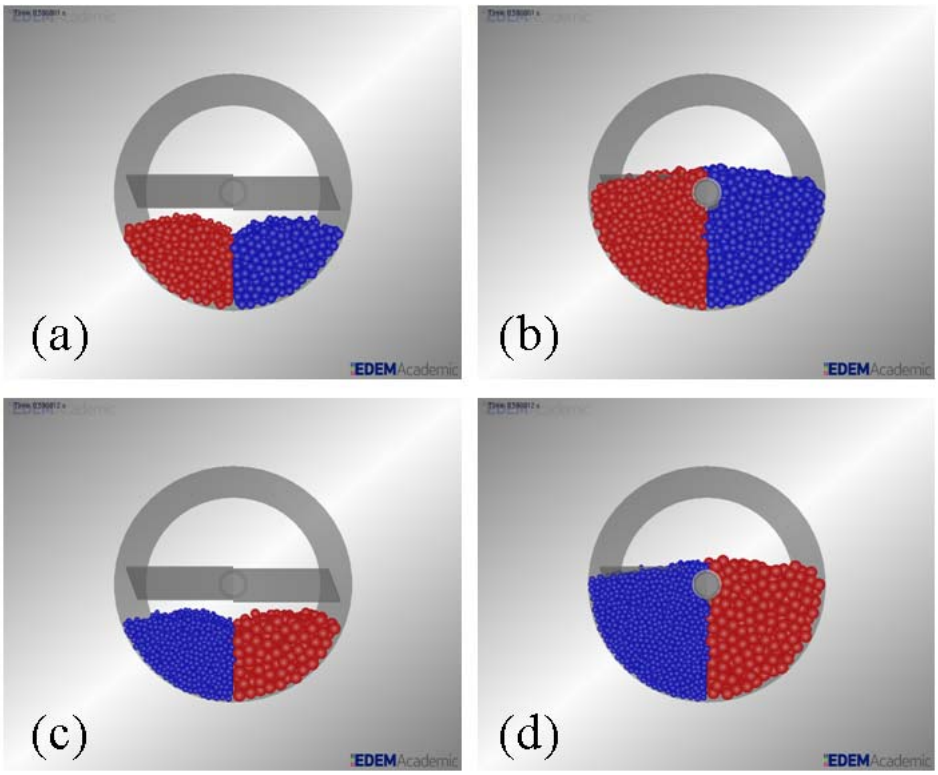

Figure 4.2 Initial loading of batch mixing in periodic section.

(a) 25% fill, non-segregating mixture, (b) 50% fill, non-segregating mixture, (c) 25% fill, segregating mixture, (d) 50% fill, segregating mixture.

Simulations were done at the blade speed of 180 RPM and the volumetric ratio of components 1:1. Two fill levels (25%, 50%), two sampling sizes (0.15 and 0.75 cm^3) and

two mixing pairs (segregating and non-segregating mixtures) were investigated in the study. As a result, four pairs of mixing processes were investigated in two sampling sizes, and were used to model the mixing process for both mixtures. The processes are performed and measured as follow.

4.1.4 Methods

4.1.4.1 Fill level and flow rate

Table 4.2 The number of initial loading particles for the periodic section

Particle number / Fill level	Non-segregating particles		Segregating particles	
	Type 1 (blue)	Type 1 (red)	Type 2 (blue)	Type 3(red)
25%	1120	1120	3840	480
50%	2240	2240	7680	960

In order to be able to match the fill level and the feed rate of the periodic section and the continuous mixer the following definition is used for the fill level:

$$filllevel = \frac{\pi d_p^3 \Delta n / 6}{0.64\pi (D_{mixer}^2 - D_{shaft}^2)/4} \qquad 4\text{-}1$$

where Δn indicates the number of particles per length in the axial direction, d_p the particle diameter, D_{mixer} and D_{shaft} are the diameter of the cylinder and the inner shaft, respectively. The coefficient 0.64 is involved as the random packing solid fraction for sphere. Note that the unit of fill level in equation (4-1) is percentage (%). It defines the (volumetric) fill level as the ratio of the volume occupied by the random packed particles to the volume of the cylinder (excluding the volume of the inner shaft). When the size of the two types of particles are different (mixing case 2), the calculation is made by converting them to only one type of particle by keep constant volumetric occupation. The initial loading number of

each type particles $N = \Delta n l_0 \bar{C}$ in the periodic section can be derived for both fill levels (Table 4.2). Here l_0=*40mm* is the length of one periodic section, and $\bar{C} = 50\%$ is the volumetric fraction of different types of particles.

When batch mixing is complete, the average axial velocity is calculated, which leads to the flow rate F:

$$F = \Delta n v_x \qquad 4\text{-}2$$

where F is measured as number of particles per time. It should be noticed that F also represents the feed rate in the corresponding continuous mixing that leads to the same fill level. Thus, equation (4-2) is used to determine the required feed rates in the corresponding simulations of continuous mixing (Table 4.3).

Table 4.3 The feeding conditions for the corresponding continuous mixer.

Feed rate F (particles/s) / Fill level	Non-segregating particles			Segregating particles		
	v_x (m/s)	Type 1 (blue)	Type 1 (red)	v_x (m/s)	Type 2 (blue)	Type 3 (red)
25%	0.121	3390	3390	0.119	11424	1428
50%	0.104	5820	5820	0.104	19968	2496

4.1.4.2 Measurement and model of variance and RSD

To determine the time-dependent change in the degree of heterogeneity of the mixture, samples are retrieved inside the mixing space. Cubes with the side length 10 mm were divided in both the continuous mixer and the periodic section. In the cases of periodic section (batch mixing), all the samples in each interval of 0.1 sec of the simulation process were considered as the samples of the same time point, which guarantees that enough samples (80 or more) were retrieved in each time point. In the cases of continuous mixing,

the samples located in the same plane perpendicular to the *x* axis were regarded as the samples in the same location. The time interval recorded is also 0.1 sec. In order to investigate the influence of the sampling size, samples were selected based on the number of particles inside each cube. Thus, for the non-segregating case (particle type 1), samples with 7 or 35 particles were selected, respectively, corresponding to the number of particles that can be randomly packed within the sampling sizes of 0.15 or 0.75 cm^3. For the segregating case (particle type 2 and 3), since particle sizes are different, samples with particles volumetrically equivalent to 23 and 118 particles type 2 were selected, to represent different sampling sizes. It should be noticed that both sampling sizes are relatively smaller than in practice, so that their influence on the value of RSD measurement can be clearly distinguished.

After selecting the samples, the variance (σ^2) and the relative standard deviation (RSD) of the volumetric fraction in samples of each time point or location can be calculated and used as a measure of the mixture heterogeneity.

In order to characterize the batch-like mixing process with fewer parameters, the variance profile $\sigma_b^2(t)$ was modeled by the exponential decrease relationship shown below,

$$\sigma_b^2(t) = \sigma_{SS}^2 + (\sigma_0^2 - \sigma_{SS}^2)\exp(-k_b t) \qquad 4\text{-}3$$

where $\sigma_b^2(t)$, σ_{SS}^2, σ_0^2 are the variance in batch mixing of periodic section, the steady state variance of the investigated sampling size, and the initial variance when particles are totally segregated, respectively; and k_b is the variance decay rate of the batch mixing process. Note that similar relationships has been used in previous studies to model V-blenders, bin blenders and other batch systems (Brone et al., 1998; Sudah et al., 2002b).

As $\bar{C} = 0.5$, σ_0^2 can be considered as equal to 0.25 using the following equation:

$$\sigma_0^2 = \bar{C}(1-\bar{C}) \qquad 4\text{-}4$$

which leads to the initial RSD value of 1 by applying equation (2-2).

4.1.4.3 Measurement and model of RTD

In order to characterize particle movement of both the continuous mixer and the periodic section the residence time distribution (RTD) is used in this work. Instead of using the pulse test method by Danckwerts (1953) in the simulation of continuous mixing, RTD was measured by considering the trajectory of particles inside the flow of the mixer, or the periodic section. Figure 4.3 shows the trajectory of one particle in the direction of axial movement in the periodic section. Since the blades in the periodic section are all forward, unilateral movement can be observed for the studied particle. When it reaches the right side of the section (40mm), it reappears at the other side (0 mm). Therefore, the time interval between two transverses at one end of the space can be considered as one sample of the RTD of a single periodic section. As a result, the RTD can be derived using the following equation:

$$E(t_i) = \frac{n_i}{\sum_{i=1} n_i \Delta t} \qquad 4\text{-}5$$

where Δt the sampling time interval, and n_i the number of samples in which the residence time of each sample lies in (t_i, $t_i+\Delta t$). The RTD within sections of a whole continuous mixer is measured in a similar way. However, in this case, one particle reaches the right side of the sections will leave the system, instead of reappearing at the left side. To eliminate noise from the measurements of RTD, around 6000 samples of particle trajectory were retrieved for each RTD measurement. If the same flow rate and fill level are shared by sections in a continuous mixer and the corresponding periodic section, the RTD within the continuous

mixer can also be derived through the convolution of the RTD in one periodic section for several times, which allows more efficient calculation.

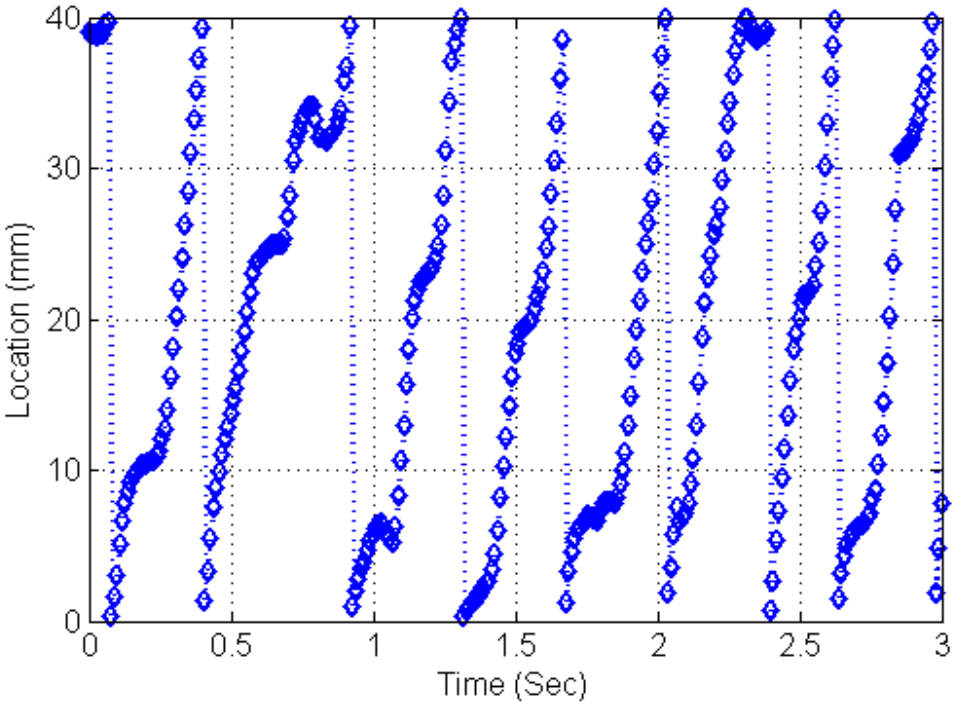

Figure 4.3 Trajectory of one particle inside the periodic section.

To clarify the physical meaning of the statistical RTD obtained above, the Taylor dispersion model (Section 2.2) is applied.

4.2 Periodic section modeling

As indicated in Section 4.1, the decrease of mixture heterogeneity is time-dependent in the batch mixing process of the periodic section, while it is location-dependent in the continuous mixing process. Meanwhile, we assume approximately a constant mixing efficiency through the whole continuous mixer where the fill level is almost the same, except for the last several sections. This indicates that in these first several constant-fill

sections, the continuous mixing process of one cluster of particles depends only on the time the cluster spends inside these sections. In other words, a continuous mixer with a series of constant-fill sections can be considered as a batch mixer, which has the same fill and mixing efficiency, and is operated for a time period equivalent to the RTD in the continuous mixer. Thus, the present model should be designed to link the mixing efficiency of these constant-fill sections, the RTD the clusters of particles stay within these sections, and the heterogeneity decay curve along the continuous mixer. Since the batch mixing in one periodic section should share the fill level and flow pattern with continuous mixing within these constant-fill sections, we assume they share approximate the same mixing efficiency. Based on this assumption, as well as the definitions of RTD and variance in the previous section, the following empirical relationship is proposed:

$$\sigma_c^2(x) = \int_0^\infty \sigma_b^2(t) E(t,x) dt \qquad 4\text{-}6$$

where $\sigma_c^2(x)$ is the variance at different locations x along the axis of a continuous mixer; $\sigma_b^2(t)$ is the variance decay of the batch mixing in the periodic section; and $E(t,x)$ is the RTD in the continuous mixer at location x. Notice that the sampling sizes of the measurement of $\sigma_c^2(x)$ and $\sigma_b^2(t)$ should be the same.

Equation (4-6) is proposed based on the assumption that the variance at each transverse plane in the continuous mixer is the average of the variance of the clusters of particles at the same plane, which may have spent different residence time inside the mixer. Since in most cases, the RTD in the convective continuous mixer is unimodal (single peak), the average variance of these clusters of particles should be close to the variance of the cluster

with the most particles, or the cluster that spends the mean residence time inside the mixer. Based on this observation and equation (4-4), equation (4-6) can be re-written as follows:

$$\sigma_c^2(x) = \sigma_{SS}^2 + (\sigma_0^2 - \sigma_{SS}^2)\exp(-k_c x) \quad 4\text{-}7$$

where σ_{SS}^2, σ_0^2 represent the same parameters as in equation (4-6), and k_c is regarded the variance decay rate along the axis of a continuous mixer, which is calculated as

$$k_c = k_b / v_x \quad 4\text{-}8$$

Equation (4-6) -(4-8) show the potential relationship between the batch mixing of a periodic section and the corresponding continuous mixing, which shares the same fill level with the periodic section. Considering the difficulty on realizing the periodic section experimentally, equation (4-8) provides an alternative to estimate the value of k_b in practice. Since the variance decay and RTD data can be measured in the continuous mixing process, we can achieve the values of k_c and v_x conveniently, and then the value of k_b can be easily calculated. On the other hand, since RSD is usually used as mixing index in practice, we divide equations (4-4), (4-6) and (4-7) by square of the average concentration ($\bar{C}^2$), and the equations are converted to:

$$RSD_b^2(t) = RSD_{SS}^2 + (RSD_0^2 - RSD_{SS}^2)\exp(-k_b t) \quad 4\text{-}9$$

$$RSD_c^2(x) = \int_0^\infty RSD_b^2(t)E(t,x)dt \quad 4\text{-}10$$

$$RSD_c^2(x) = RSD_{SS}^2 + (RSD_0^2 - RSD_{SS}^2)\exp(-k_c x) \quad 4\text{-}11$$

The simulation designs described in the previous section are used in the next section to validate equations (4-9) -(4-11).

4.3 Verification

4.3.1 Non-segregating particle mixture case

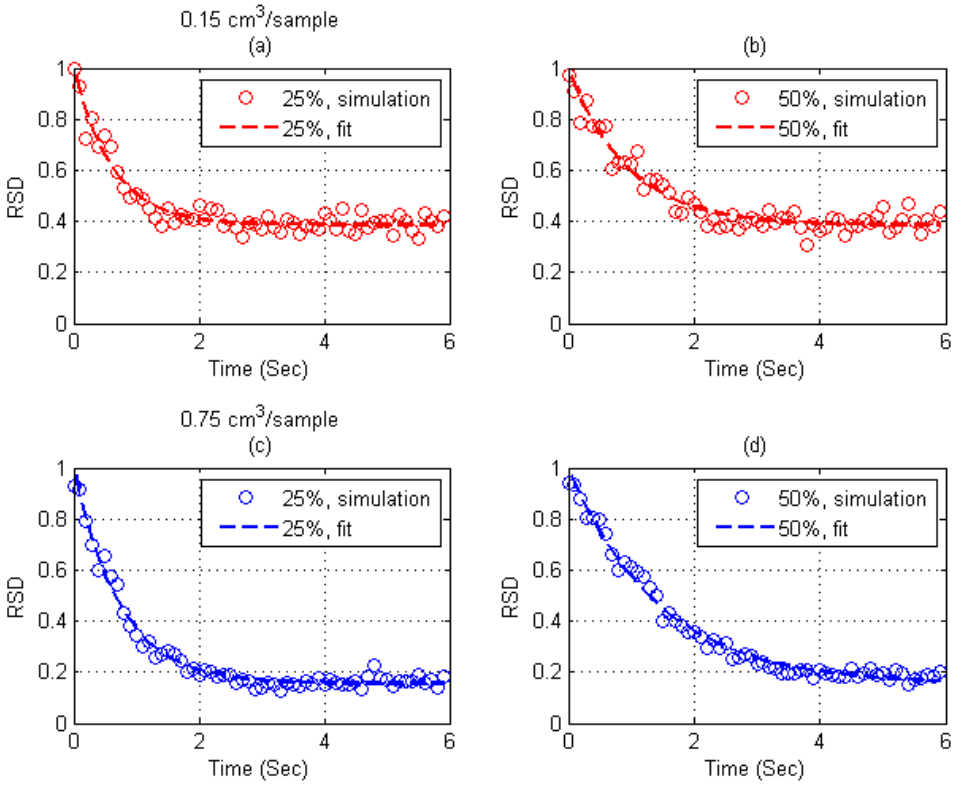

Figure 4.4 RSD-t curves of batch mixing in periodic section of non-segregating particles.

The non-segregating batch mixing results of the periodic section are shown in Figure 4.4. The influence of the fill level and the sampling size can be charcterized. The upper graphs show the RSD decline at the smaller sampling size (7 particles), which indicates larger RSD_{SS} (~0.4). When decreasing fill level from 50% to 25%, the kinetics of mixing improves, i.e., the RSD decays quicker. However, RSD_{SS} is independent of the fill level. This is expected since the final mixing state in non-segregating mixing case represents random packing of the mixture, in which RSD_{SS} is only related to the sampling size. In this

case, it can be calculated using the binomial theorem (Brone et al., 1998). Similar results were observed at the larger sampling size, in which a smaller value (~0.16) was obtained.

In order to identify the model parameters for the batch-like processes, we use the least square method for the error between the simulation of RSD decay and the model for one component in the section. Since the initial state can be calculated using equation (4-4) ($RSD_0=1$), the parameters in present fitting process are only RSD_{SS} and k_b. The curves in Figure 4.4 correspond to the best fits. As expected, almost the same RSD_{SS} are achieved for both fills in non-segregating mixing, while the larger value of k_b in 25% fill indicates faster mixing. In fact, based on equation (4-9), if $(RSD_b^2(t) - RSD_{SS}^2)/(RSD_0^2 - RSD_{SS}^2)$ is plotted logrithmatically vs. time, the batch mixing rate k_b can be defined as the negative slope of the linear relationship. Therefore, only two adjustable parameters are required to capture all process configurations and the fitted, smoothed decay curves can be used in predicting the mixing of the corresponding continuous processes.

The fill level distributions of the non-segregating mixing cases vs. the section number are also plotted (Figure 4.5a). Results indicate similar distributions for both fills. Due to the effect of no weir at the end of the mixer, fill level drops quickly at the right of the 6^{th} section (the vertical dot line). Before that transverse plane, the fill levels are approximately constant. As indicated in the modeling, application of equation (4-11) is valid only within constant-fill sections of the mixer. Therefore, the RTD only within the first six sections are statistically calculated, which are used in the corresponding continuous mixing prediction. The RTD data at 2, 4, 6 constant-fill sections are plotted in Figure 4.6. Since the calculations from continuous mixing and from convolution of single periodic section mixing lead to the same RTD data, only the RTD from the continuous mixing are shown.

Linear increase of the mean residence time, as well as the accumulated dispersion, can be observed with the increase of section number. On the other hand, the decrease of fill level leads to smaller mean residence time and boarder RTD profile. This indicates faster axial mixing and movement at low fill, which is often observed in both batch and continuous mixers (Portillo et al., 2008b). As more space is available at low fill, a single particle experiences more turns-over per blade pass, which facilitates both axial flow and dispersion. The curves of RTD in Figure 4.6 represent the best fit by applying the least square method, and show good accuracy on describing the data.

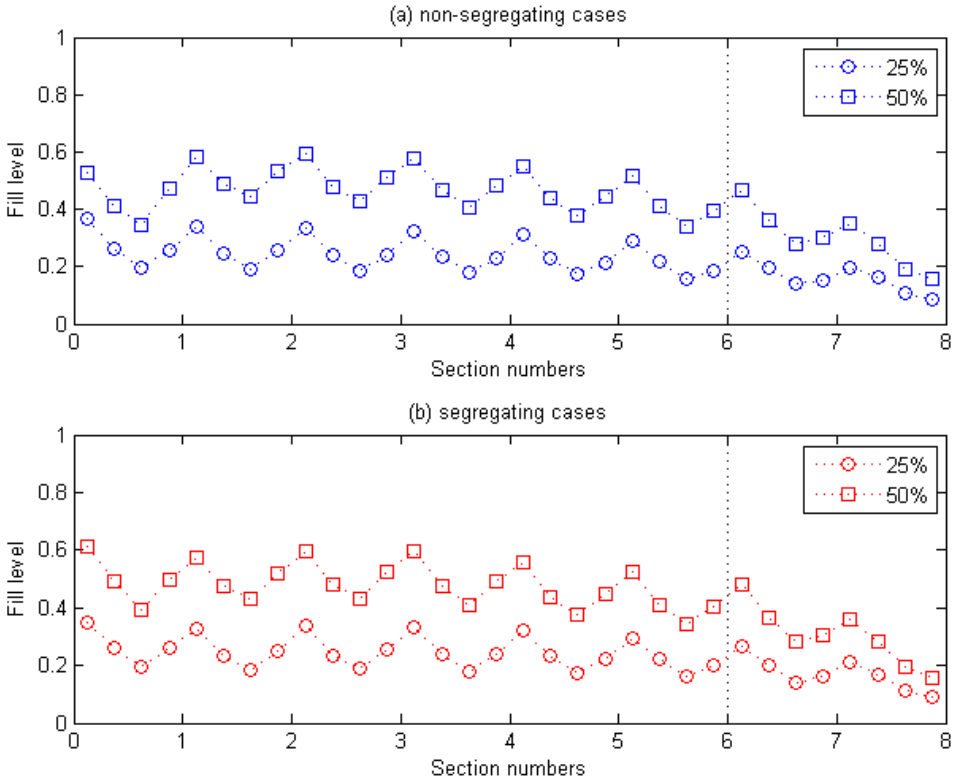

Figure 4.5 The fill level distribution along the mixing axis.

(a) Non-segregating cases. (b) Segregating cases.

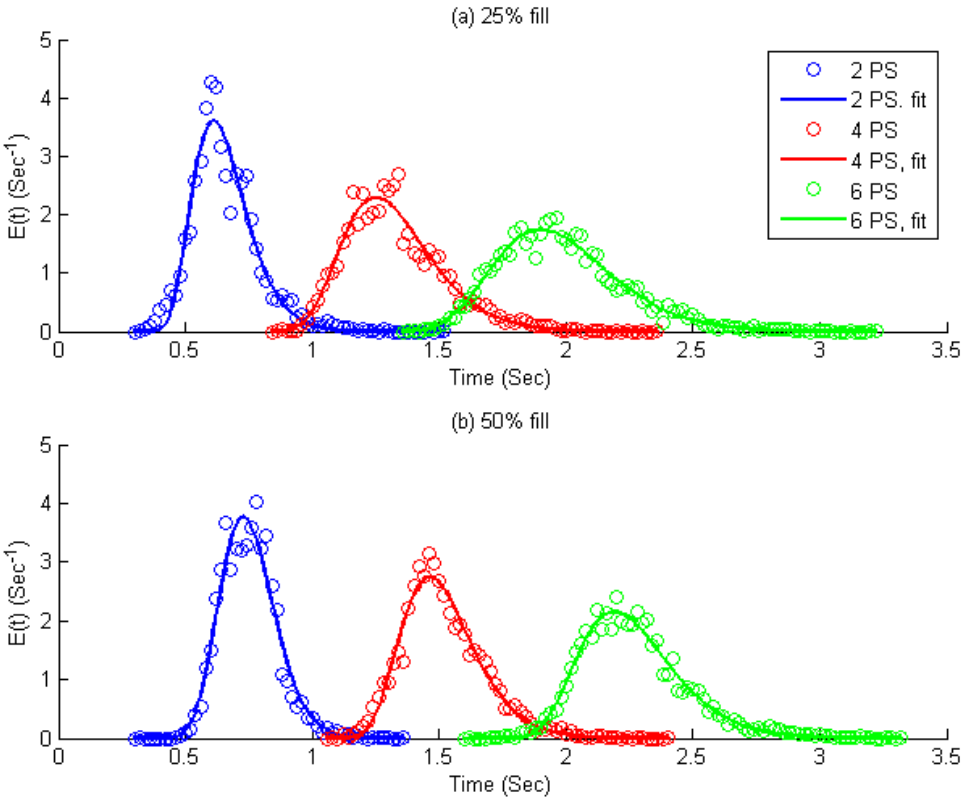

Figure 4.6 RTD data and curve-fitting of 2, 4 and 6 constant-fill sections for non-segregating partilcles.

Figure 4.7 shows the simulated and calculated results of RSD decay in the case of continuous mixing, for the first six constant-fill sections. By using equation (4-10), the model fitted curves of both the batch mixing (RSD-t curve) in the periodic section and the RTD were applied in predicting the RSD decay curve within the continuous mixer. It can be seen that the calculated results could capture very well the simulated results for the constant-fill sections (equation (4-11) leads to almost the same prediction). To compare the RSD decay rate of different fills, the RSD values of 0.5 (for the sampling size of 0.15 cm^3) and 0.25 (for 0.75 cm^3) were considered as the check points. It can be observed at 25% fill,

fewer periodic sections are needed to achieve the same check point, indicating better continuous mixing performance. Based on the obtained RSD-t and RTD information, although at 25% fill mixing is faster, the particles move also faster than that of 50% fill and exit the mixer earlier. Therefore, the influence of batch mixing rate k_b to the RSD decay rate $k_c = k_b / v_x$ is more significant than that of the particle movement v_x in the current mixing case. On the other hand, feed rate at 50% fill is significantly larger than that at 25% fill, which is preferred in high flux manufacture process.

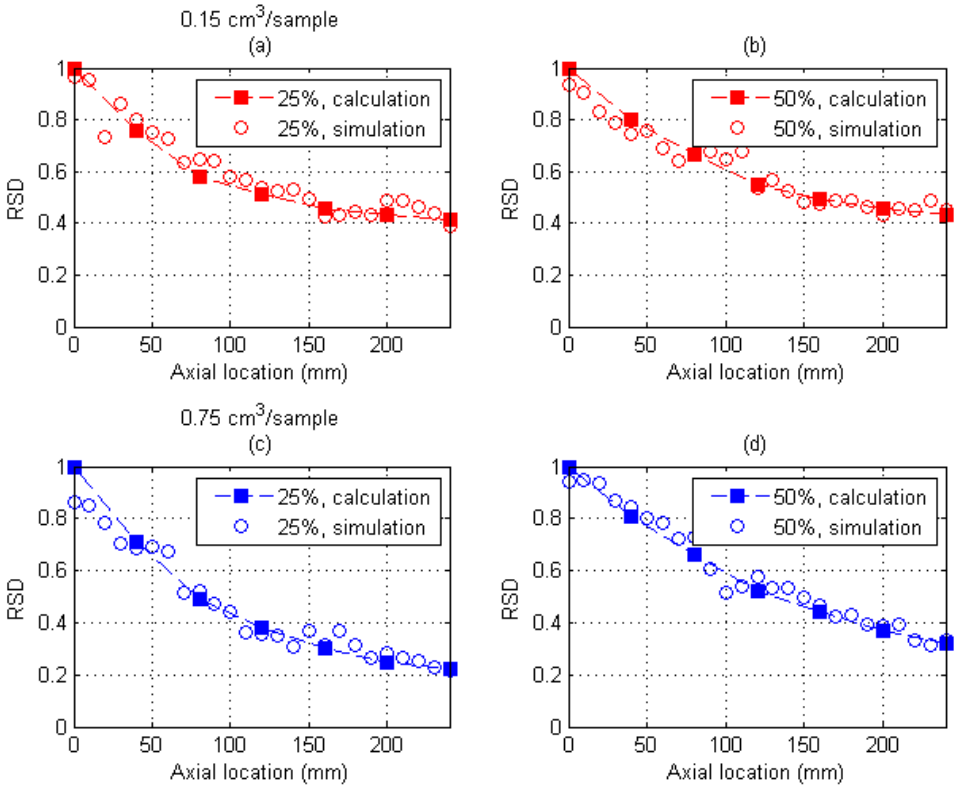

Figure 4.7 Simulation and calculation of RSD-l curves in continuous mixing processes, non-segregating particles.

4.3.2 Segregating particle mixture case

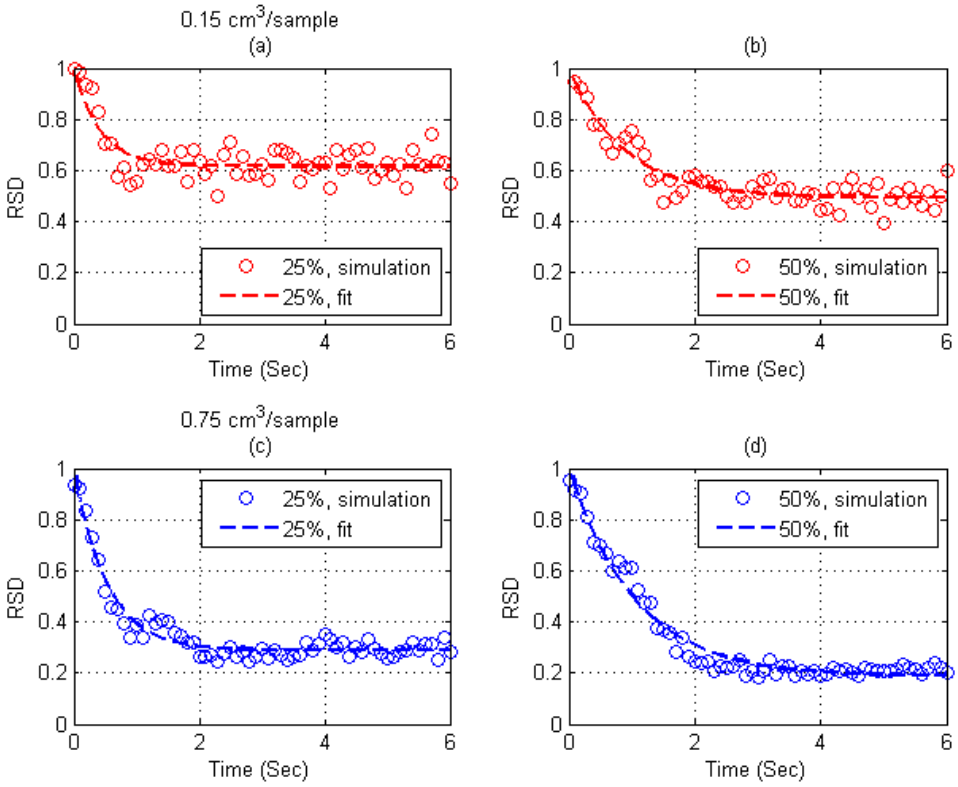

Figure 4.8 RSD-t curves of batch mixing in periodic section filled by segregating particles.

Figure 4.8 shows the batch mixing results for the segregating mixture. As illustrated in the previous section for the non-segretating case, decreasing the fill level allows larger batch mixing rate. However, the important aspect here is the fact that RSD_{SS} are fill level dependent, and in both fills should be higher than the case of random packing. This means that the size and density ratio between the particles induces segregation that the mixer cannot completely eliminate. RSD_{SS} are larger at 25% fills in both sampling sizes, indicating more segregation. This can be explained by the strength of blade disturbance on the segregation. As the fraction of prepelled particles is smaller at low fill, the influence

blade disturbance to the formation of segregation is smaller, leading to a more segregated mixture.

For the segregating cases, the fill level distributions within the continuous mixer processes are almost the same as the non-segregating cases (Figure 4.5b). As a result, the first six sections in the continuous mixer approximately share constant fill level with the periodic section. The RTD calculated at the end of the 2, 4, 6 sections are plotted in Figure 4.9, which shown high similarity to these of the non-segregating cases. This similarity indicates small difference between the bulk flows of materials with different properties, in our current study.

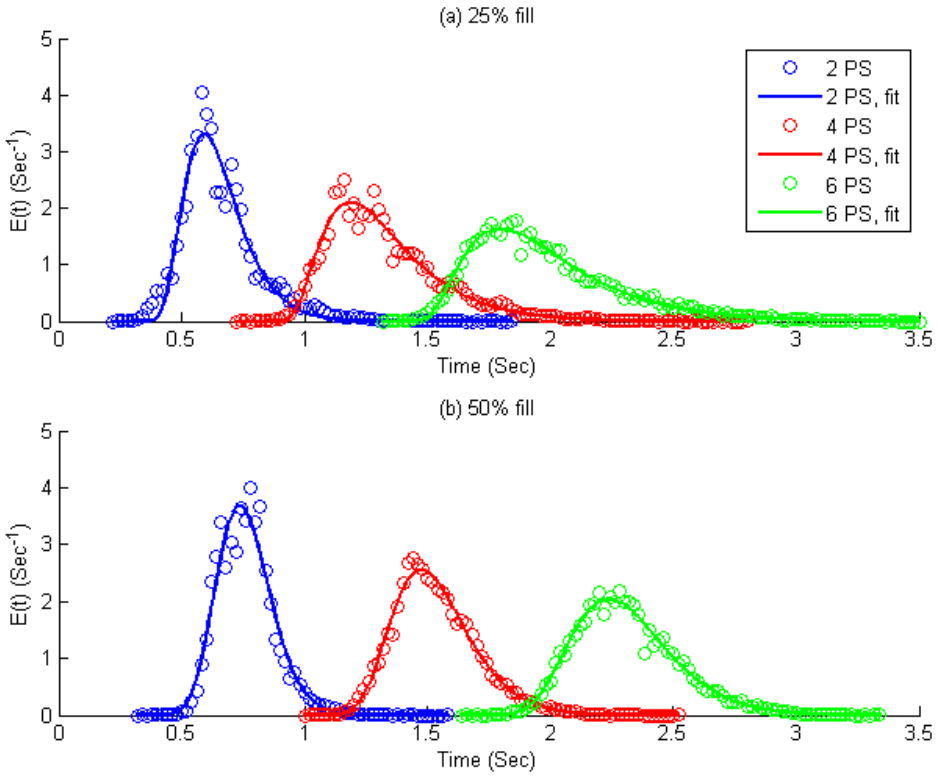

Figure 4.9 RTD of batch mixing in 2, 4 and 6 periodic sections for segregating partilcles.

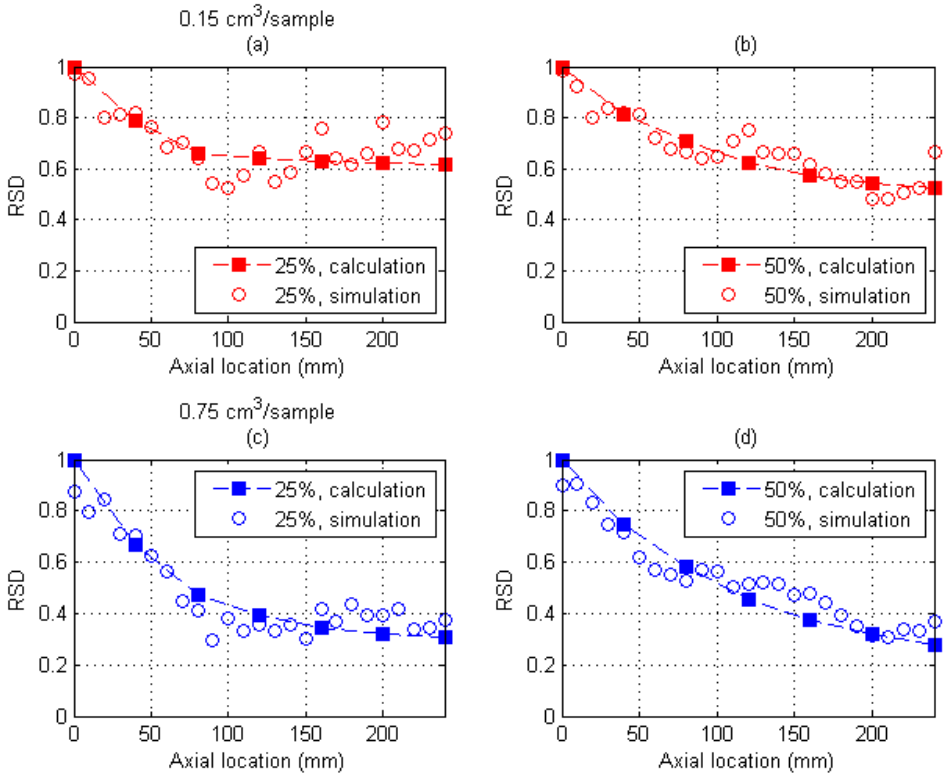

Figure 4.10 Simulation and calculation of RSD-l curves in continuous mixing processes, segregating particles.

The simulated and calculated results of RSD decay along continuous mixing axis can be seen in Figure 4.10. Although fluctuations can be observed on the simulated data, which are caused by random formation of segregation along the direction of particle movement, the calcuated curves predict the simulation trends very well. As mentioned in the batch mixing case, RSD_{SS} is determined by the strength of blade distubance, which is lower at 50% fill. Meanwhile, due to the coupling effects of both mixing and axial motion, RSD of continuous mixing decays quicker in the case of 25% fill, while better mixing is achived in the case of 50% fill. Since 50% fill also leads to higher feed rate and thus larger production

rate, it should be selected for continously mixing of this segregating case, although more sections are needed to construct the desired mixer.

4.4 Summary

In this chapter, we have proposed a model based on the idea that the convective continuous mixing results from the combination of a batch-like mixing and an axial flow of the particles. Based on the empirical relationship between the two processes, the cases of non-segregating and segregating mixing are investigated. The results show that the proposed methodology can describe both cases capturing the main characteristics of the continuous mixing process, including the batch mixing rate (k_b), the axial velocity particles move forward (v_x), and the quality of the steady state mixture (RSD_{SS}). Results show that the necessary number of periodic sections (indicated by k_c , larger k_c leads to less necessary number of sections) in the continuous mixing process is not only determined by the rate of local radial mixing, but also by the velocity how fast the materials are delivered inside the mixer. Therefore, for the purpose of clearly understanding effects of different variables on mixer performance, a separate consideration of mixing and moving is suggested for further study of continuous powder mixing processes.

In the application of the model, direct prediction of the variance (or RSD) decay requires constant-fill sections. If there is a fill level distribution (for instance, no weir at the end), mixing efficiency changes through the mixer, and prediction of the whole mixer through the batch mixing of periodic section at a single fill level is not applicable any more. That is the reason direct calculation using the model requires the exclusion of the sections with a different fill level. To improve this inconvenience, an important idea is that the variance

decay can be calculated in separate subsections with different fills or mixing efficiencies. The decreased variance calculated at the end of one subsection should be used as the initial condition in the calculation of the next subsection. In other word, we can define a multiplicative process for the variance decay, where in each subsection, variance goes down by a factor $F_i = \exp(-k_{c,i}\Delta x_i)$. Here $k_{c,i}$ represents the uniform variance decay rate along axis x within subsection i, and Δx_i denotes the length of the subsection. This requires involvement of mixing rates of the subsections at different fills, and the RTD calculated separately for different subsections. This issue is worthy of investigation and under consideration of future publication.

It should be emphasized that the periodic section modeling work indicates the similarity between the continuous powder mixing and an equivalent batch mixing process. Therefore, the knowledge developed in the field of batch mixing can be applied for the design and optimization of continuous mixers. That means that designs and operations that improve the performance of batch mixer can be conveniently used in the design of a continuous mixer, provided that the axial motion of the materials is slow enough for the equivalent batch mixing to be complete. Also due to the difficulties of experimentally performing batch mixing of the periodic section, knowledge of the similarity between the mixing rate of one periodic section and batch mixers with similar geometries can facilitate the practical estimation of the mixing efficiency of a continuous process, and thus is worth considering. This issue is discussed in the next chapter.

Chapter 5

Blender design based on batch experience

To examine the similarity of blending between batch and periodic section, in this chapter we use the Discrete Element Method (DEM) to investigate a family of simple geometries consisting of a horizontal cylindrical section with periodic end walls, stirred by several blades rotating around an axial shaft. Ideally, it would be desirable to have access to a simple, experimentally realizable system that could be used to study cross-sectional mixing in batch-like geometry in an effective manner. A simple geometry that is experimentally realizable is a cylindrical section with solid end walls. However, the presence of the end walls should be expected to affect the flow pattern, possibly leading to very different mixing performance, potentially rendering the device useless as a validation system. The rest of the chapter is organized as follows: the Discrete Element Method (DEM), and the parametric space examined are described in Section 5.1; in Section 5.2 we describe the results obtained, which show the effects of these designs on the mixing performance. We summarize these effects and present the conclusions of this work in Section 5.3.

5.1 Methodology

5.1.1 Discrete Element Method

Since the blending experiments in a cross section with periodic boundaries are difficult (and perhaps impossible) to perform, we use the Discrete Element Method (DEM) as the tool for examining the effect of blade patterns on flow and mixing for the configurations of interest. Particles simulated are spheres, where the contact forces are calculated using the

default Hertz-Mindlin no slip contact model (Mindlin, 1949). The governing equations for this contact model are summarized in Tables 5.1. As a starting point, the analysis in this work is only focused on the mixing dynamics of free-flowing materials. several geometries are examined: (1) the "all forward" configuration, where two blades push particles in the same direction along the axis (Figure 5.2a); (2) the "all alternate" configuration where one blade pushes the particles forward, and the other moves the particles backwards along the axis (Figure 5.2b); (3) the "partial forward" configuration, where two blades push particles forward and one moves particles backward along the axis (Figure 5.7a); and (4) the "partial alternate" configuration, where two "partial forward" cross sections are symmetrically connected (Figure 5.7b).

Table 5.1 Governing equations in the Hertz-Mindlin no slip contact model.

Force	Formula	Annotation
Normal force	$F_n = \frac{4}{3} E^* \sqrt{R^*} \delta_n^{3/2}$	e coefficient of restitution E^* equivalent Young's Modulus m^* equivalent mass R^* equivalent radius S_n normal stiffness S_t tangential stiffness $\overrightarrow{v_n^{rel}}$ relative normal velocity $\overrightarrow{v_t^{rel}}$ relative tangential velocity δ_n normal overlap $\vec{\delta}_t$ tangential overlap
Normal damping force	$F_n^d = -2\sqrt{\frac{5}{6}}\beta\sqrt{S_n m^*}\overrightarrow{v_n^{rel}}$ $\beta = \frac{\ln e}{\sqrt{\ln^2 e + \pi^2}}$	
Tangential force	$\vec{F}_t = -S_t \vec{\delta}_t$	
Tangential damping force	$\overrightarrow{F_t^d} = -2\sqrt{\frac{5}{6}}\beta\sqrt{S_t m^*}\overrightarrow{v_t^{rel}}$	

Before mixing starts, particles with the same properties are labeled with different colors (red and blue) to simulate an initial side-by-side loading pattern along the shaft. This guarantees that the direction of the studied batch-like mixing process is the same as in the

corresponding continuous process. Blades then start to rotate at 180RPM, and mixing for a period of 6 sec is recorded. Samples are captured by dividing the mixing space into small cubes ($10\times10\times10$ mm^3), in which the cubes with 35 particles were selected to represent the sampling sizes of 0.75 cm^3. Samples in each 0.1 sec time interval of the simulation process were considered as the samples of the same time point, which guarantees enough samples (80 or more) were retrieved in each time point. The RSD is calculated based on the samples retrieved in the interval of each 0.1 sec. All four RSD decay data sets (two fill levels by two sampling sizes) are then fitted. In this way, we can compare the mixing rates of different geometries by using the fitted values of k_b.

5.1.2 Quiver plot of velocity field in a rotating frame of reference

Velocity field analysis, which is routinely used to examine mixing of fluids, has also been used in the investigation of solid mixing process for batch mixers (Alexander et al., 2004; Brone et al., 1997; Jones et al., 2007; Laurent and Bridgwater, 2002; Moakher et al., 2000; Sudah et al., 2002c; Wightman et al., 1998), continuous mixers (Sarkar and Wassgren, 2010; Sarkar and Wassgren, 2009) and both (Manas-Zloczower, 1994). In these bladed geometries considered here, the effect of rotary blades sweeping the mixing space hinders a strict application of flow analysis, because the geometric space of the material flows driven by blades is time-dependent in a stationary frame of reference. This time-dependence makes it difficult to establish a straightforward relationship between flow characteristics and mixing performance in these mixers.

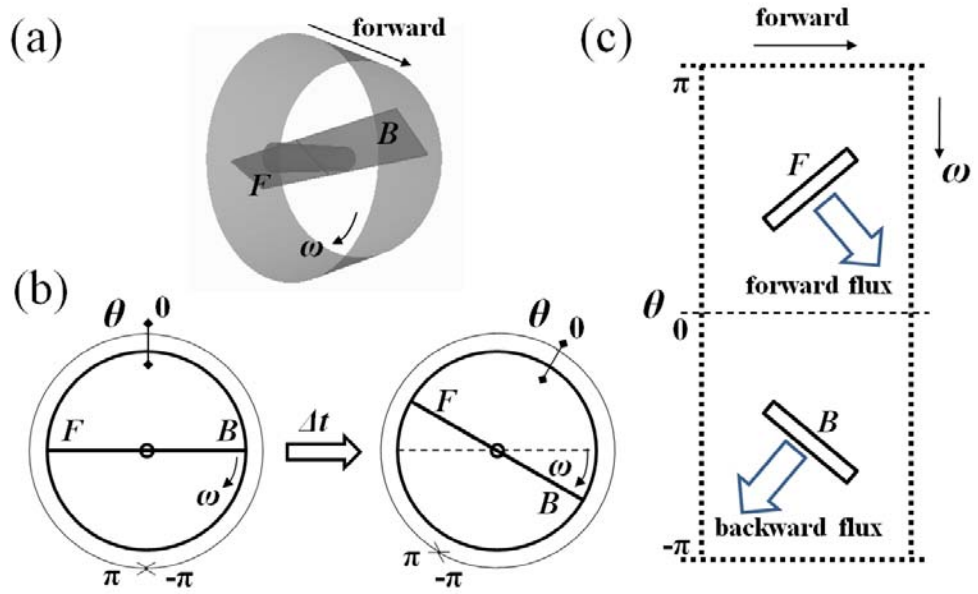

Figure 5.1 The rotating frame of reference.

(a) Side view of one open-ended batch mixing space. F indicates the forward blade and B the backward blade. (b) The rotating speed of the rotating frame equals to the speed of rotating shaft, so that in this frame the location of blades is stationary. (c) The rotating frame view in which quivers of velocity fields are plotted. Notice the forward or backward fluxes pushed by the blades.

To simplify interpretation of flow portraits generated by the passing blades, a rotating frame of reference, similar to the one used by Harvey et al. (1995) in describing the fluid flow in a baffled impeller stirred tank, is introduced in this work. The advantage of this representation is that the geometry determined by the solid boundaries (wall and blades) is steady in this frame of reference. It is important to remark that we do not simulate the velocities in a rotating frame, only represent them in the rotating frame for ease of interpretation.

The rotating frame is set to have the same rotational speed as the blades, so that the blade locations are stationary in this new frame (see Figure 5.1b). Subsequently, quiver plots of the velocity field in this frame are calculated as follow. At time Δt after mixing starts, the rotated angle θ_0 of the reference frame is

$$\theta_0 = \omega \Delta t \qquad 5\text{-}1$$

where ω equals to the angular velocity of the rotating blades. For one particle with location (x, y, z) and velocity components (v_x, v_y, v_z) that are measured in a stationary rectangle coordinate system, its location and velocity in the corresponding cylindrical coordinate system are denoted as (θ', r, x) and $(v_{\theta'}, v_r, v_x)$, respectively. Here x represents the location of the particle in the axial direction, y the location in the side direction and z in the vertical direction in the rectangle coordinate system; θ' the angle in the tangent direction, and r the location in the radial direction in the cylindrical coordinate system. Based on these notations, the location of the same particle in the rotating frame of reference can be denoted as (θ, r, x), in which

$$\theta = \theta' - \theta_0 \qquad 5\text{-}2$$

where $\theta \in (-\pi, \pi)$ represents the angle of the particle in the rotating frame, r and x have the same meaning as these in the cylindrical coordinate system.

In order to facilitate intuitive analysis, one more simplification is needed: we plot the velocity field in angular-axial 2-D coordinates, using color to denote velocity magnitude and arrow to denote velocity direction. Such 2-D plots are more easily interpreted than a full 3-D representation of a vector field. To this end, we average velocities along the radial coordinate; i.e., all particles within the same beam (θ, x) are considered to be at the same

location in the rotating frame. Since the vertical axis (θ) in Figure 3c is the angular coordinate, the angular velocity ω_θ instead of the linear velocity $v_{\theta'}$ is used as the vertical velocity component of the velocity vector field and, as mentioned, is radially averaged once the proper angular expression is denoted,

$$\omega_\theta = v_{\theta'} / r \qquad 5\text{-}3$$

It should be noted that the angular velocity ω of the rotating frame is not subtracted in this representation, which means that the effect of blades on particle fluxes can be observed in the quiver plots. As a result, the vector (ω_θ, v_x) is considered as one sample of the velocity field at location (θ, x), which can then be time-averaged to draw the approximate steady-state quiver plot of velocity field. The amplitude of the velocity at each location in this field is calculated as:

$$v(\theta, x) = \sqrt{\left(\frac{\omega_\theta D_{mixer}}{4}\right)^2 + v_x^2} \qquad 5\text{-}4$$

in which the velocity at half of the radius ($D_{mixer}/4 = r_{mixer}/2$) is used to represent the linear velocity component on the angular direction.

This simpler representation is obviously obtained at a cost: we lose the information describing the radial component of velocity. However, the angular velocity provides a good representation of cross-sectional circulation, while the axial velocity captures the nature of axial net flow as well as axial recirculation. In summary, the usefulness of the plots is to make up for the loss of radial velocity information.

5.2 Case studies

3.1 Case Study 1: effect of end walls

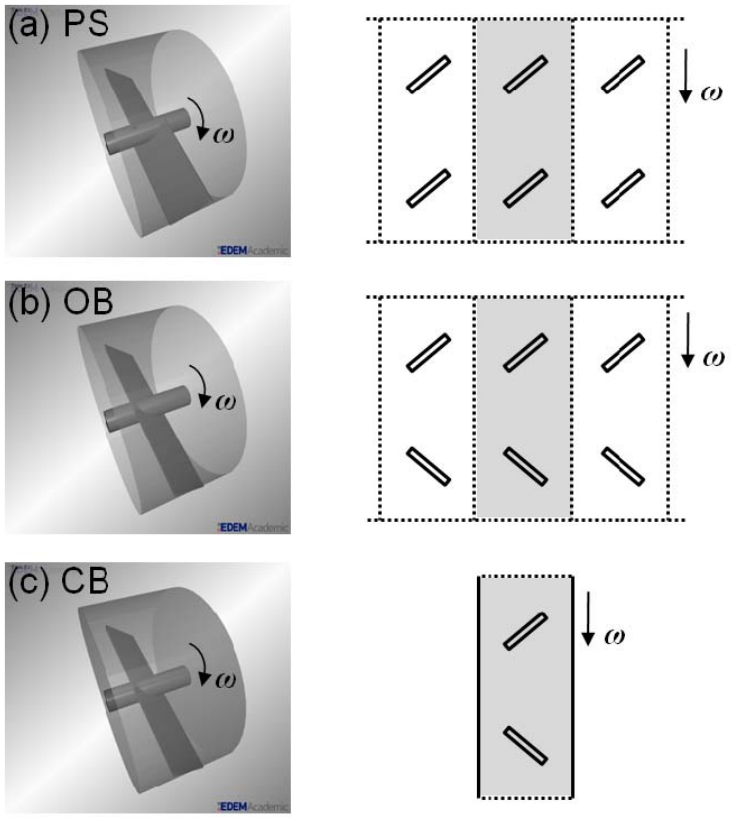

Figure 5.2 Case Study 1: geometries and rotating frame view of blade patterns.

(a) The "all forward" periodic section (PS). (b) The "all alternate" open ended batch section (OB). (c) The "all alternate" close-ended batch section (CB). Dotted lines in the rotating frame are the periodic boundaries, and solid lines indicate end walls.

The effects of geometry designs on the mixing performance of several cross-sectional elements were investigated in three case studies. For our first Case Study, the cross-sectional element representing an "all forward" periodic section (PS) was constructed from a horizontal cylinder (diameter 80 mm and length 40 mm). Two 40° forward blades (20×40 mm^2) were located opposite to one another at the middle of its shaft (diameter 10mm), which was symmetrically placed at the middle axis of the cylinder

(Figure 5.2a). This PS elementary geometry simulate the ideally cross-sectional mixing in an "all forward" continuous mixer that shares the same fill level and flow rate. Based on the geometry of the PS, the corresponding "all alternate" geometries can be designed by changing one blade angle to 40° backward, which allows elimination of the net forward flux. Two geometries were designed to test the influence of end walls: the open-end batch mixer (OB, Figure 5.2b) and the close-end batch mixer (CB, Figure 5.2c), based on the existence of end walls on the two transverse ends of the mixing space. Notice that the OB simulates mixing at the middle of a long periodic batch mixer consisting of a series of linearly connected OB elements, or the corresponding ideally cross-sectional mixing in an "all alternate" continuous mixer when inlet and outlet are involved, while CB simulates the batch mixer consisting of only one such element.

Figure 5.3 shows the velocity quiver plots of simulations performed in these geometries. The blade patterns of adjacent elements are shown below each plot for a better illustration of the velocity field. As the quiver plots are similar for mixing in both 25% and 50% fills, only those of 25% fill are plotted (the same for the other two case studies). Two design issues are involved here: the difference of blade directions, and the existence of end walls. To study the first issue, the PS and OB quiver plots are compared. While similar velocity fields are observed around each blade in both geometries, the velocity fields of the two blades are in the same direction in the PS geometry, but in oppoiste direction in the OB geometry, which leads to the development of a shear zone between the two blades ($\theta = -\pi, 0, \pi$) in the OB geometry. This suggests faster mixing in the OB geometry. Furthermore, when comparing the velocity fields of the OB and CB geometries, convective

recirculation zones are observed between the end walls and the neiboring blades in the mixing space of CB, which suggests even better mixing conditions.

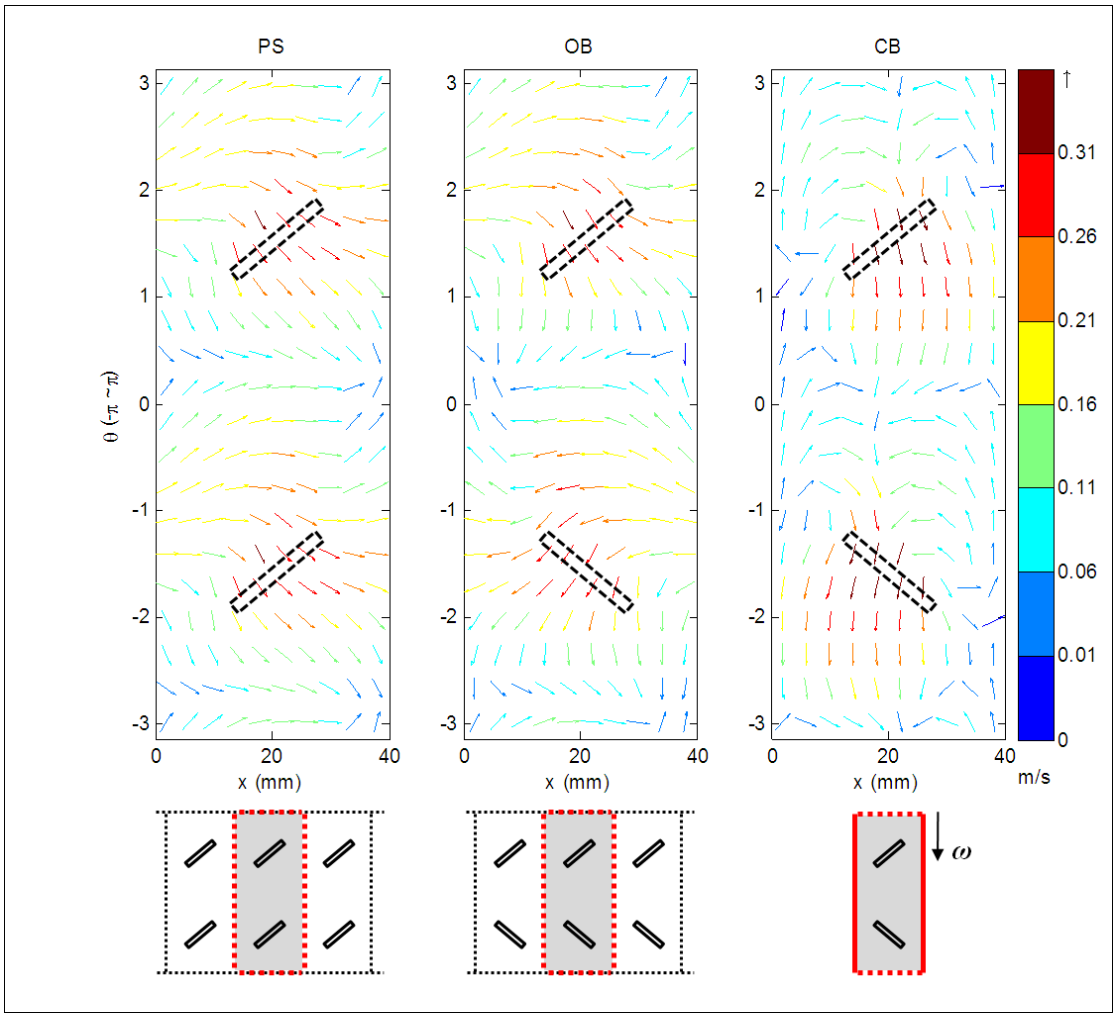

Figure 5.3 Velocity quiver plots of Case Study 1.

The regions enclosed by the red lines are plotted. PS, the “all forward” periodic section; OB, the “all alternate” open-ended batch section; CB, the “all alternate” close-ended batch section.

The fill level profiles of these geometries are drawn in Figure 5.4. Although profiles are similar for different fills in the same geometry, the differences in these fill level profiles,

increase from OB to PS to CB. The low fill at the middle of the mixing space is caused by the blade motions in the same area: fill level decreases as blades continuously propel particles away from the region of blades until conter-current fluxes due to the induced fill level gradient are able to balance the effect of these convective motions.

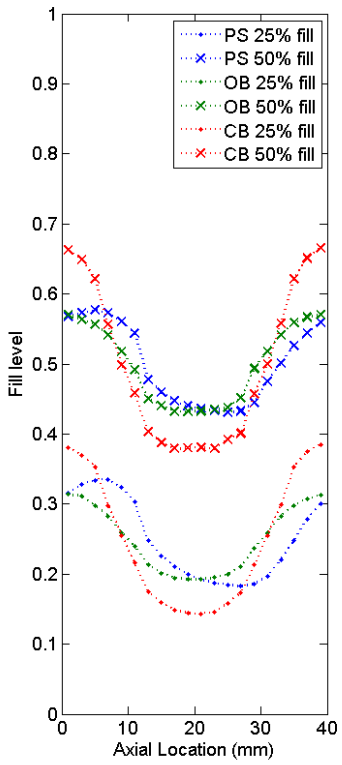

Figure 5.4 Fill level profiles along the axis of the simlated geometries in Case Study 1.

The difference of the fill level profiles can be analyzed as follows. For the PS, the two forward blades provide approximately twice the same forward fluxes in one revolution, leading to a overlapped peak of fill level at 28 mm ahead of the blades, or 12 mm behind, due to the periodicity of the space. This indicates that the peak of fill level due to single blade motion should be 28 mm away from the blade. For the purpose of validation, a

continuous mixing process using the same physical and numerical parameters is simulated, which consists of eight PS elements geometrically similar to those modeled in the current Case Study (Figure 5.5). The used feed rate in the continuous mixer equals to the average flow rate of the mixing in the corresponding PS geometry at 25% fill. Therefore, similar cross-sectioanl mixing conditions are simulated for both the continuous mixer and the PS goemetry, thus similar fill level profile is expected to be observed. Except for the last two PS elements, where materials are being freely discharged from the mixer, and for the first element, where inlet particles lead to a slightly different fill level, almost the same fill level profile is observed in the rest elements of the continuous mixer as in the PS geometry, supporting the applicability of the current studies to the analysis of mixing of cross-sectional elements in continuous mixers.

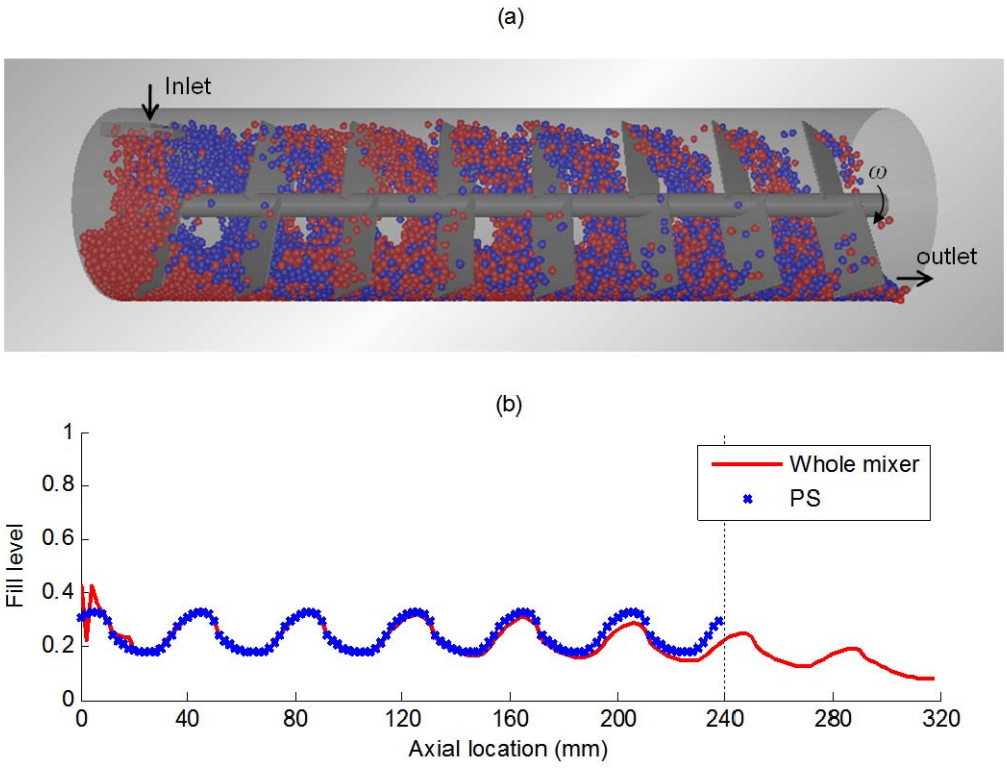

Figure 5.5 Fill level gradient in a continuous mixing simulation corresponding to the cross-sectional PS mixing at 25% fill.

(a) The side view of the continuous mixing process comprised by eight the same PS elements. (b) Comparison of the fill level gradients along the axis of the mixer and in thecross-sectional PS element.

Based on the fill level analysis of the PS geometry, the peaks of fill level in the OB induced by alternate blades should be around two symmetric sites 28 mm away from the middle of the space (or at 8 mm and 32 mm from the left). In Figure 5.4, a single peak is observed at the ends in the OB element, which results from the superpostion of the two partially overlapped peaks due to signle blade motion. For the CB, the same fluxes that pass the two ends of the space in OB now stop at the end walls, where accumulated fill level is even higher than in the PS.

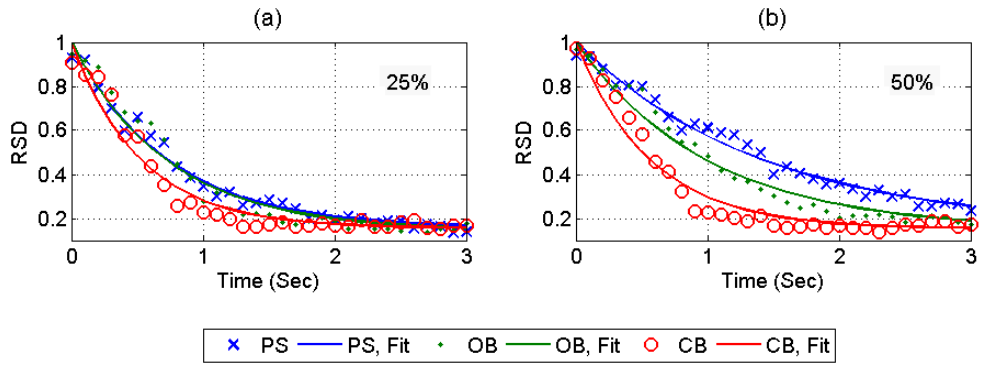

Figure 5.6 RSD decay data and the fitted curves for Case Study 1. (a) 25% fill, (b) 50% fill.

To compare mixing rate of the three geometries, the RSD decay data and the fitted curves were plotted as shown in Figure 5.6. For non-segregating mixtures of identical particles,

the value of steady state RSD_{SS} is determined by the sampling size, and can be predicted by binomial theorem:

$$(c_1 + c_2)^n = \sum_{k=0}^{n} C_n^k c_1^{n-k} c_2^k \qquad 5\text{-}5$$

$$RSD_{SS} = \frac{2}{c_1 + c_2} \sqrt{\frac{\sum_{k=0}^{n} C_n^k \left(\frac{c_1(n-k) + c_2 k}{n} - \frac{c_1 + c_2}{2} \right)^2}{\sum_{k=0}^{n} C_n^k}} \qquad 5\text{-}6$$

where c_1 and c_2 represent values of the two identical particles in the mixture; n denotes the number of particles in each sample, and C_n^k the binomial coefficient, which is a factorial function of n and k. Here we define $c_1=0$ for the blue particles and $c_2=1$ for the red particles, and the expectation of mean concentration of red particles in this mixture is 0.5. We can predict $RSD_{SS}(n=35)=0.16$ for the sample size of 0.75 cm^3, which fit the results very well. The results also indicate the difference of mixing rate k_b for these geometries: mixing rate increases from PS to OB to CB, as has been suggested by the velocity vector portraits. At 50% fill, the exponential mixing rate in CB is almost three times larger than in PS and twice as large as in OB. It is worth noting that the end walls in CB lead to fill level gradient larger than in the other two geometries, which may induce a stronger re-circulating flux to exchange particles between the sides and the middle of the mixing space, potentially explaining the observed faster mixing. However, the fill level gradient in OB is slightly smaller than PS, while the mixing rate is larger, probably due to the shearing flow between the two opposite directed blades. On the other hand, while the plotted velocity field are similar for both fills, mixing at 25% fill is found to be faster than at 50% fill. This is a fairly common observation for batch mixers and has been reported for rotating drums (Sudah et al., 2002a; Wightman et al., 1998; Wightman and Muzzio, 1998), V-blenders (Brone et al.,

1998; Brone et al., 1997), double cones (Brone and Muzzio, 2000), and different types of bin blenders (Arratia et al., 2006; Sudah et al., 2002c).

Due to the velocity fields and mixing processes investigated above, although CB mixes much faster due to the effect of the end walls, mixing rate in the OB is more similar to that in PS. Thus, the batch mixer with end walls is not suitable in estimating the mixing performance of the corresponding PS in the continuous mixing process. On the other hand, Figure 5.3 indicates that the main difference between the OB and the PS comes from the flow patterns, or the backward blade in the OB geometry. To solve this difference, one straightforward method is to introduce similar backward flux into the periodic section, which is discussed as follows.

3.2 Case Study 2: effect of backward blade in the PS

For our second Case Study, we place three blades at 120° from one another around the shaft, and at least one backward blade and one forward blade are always used. In the first configuration examined, one additional 40° backward blade is added into the "all forward" PS (Figure 5.7a). Since an odd number of blades were designed in this "partial forward" PS, the corresponding "partial alternate" batch mixer cannot be constructed just by flipping the blade orientation, as in Case Study 1. Instead, the open-end batch mixer was formed by symmetrically connecting two mirror-image "partial forward" PS elements (OB, Figure 5.7b), in which fluxes due to symmetric pairs of blade motions always counterbalance each other. Based on the OB geometry, a third batch mixer was constructed by rotating the first element of the OB 120° in the direction of ω (OBR, Figure 5.7c).

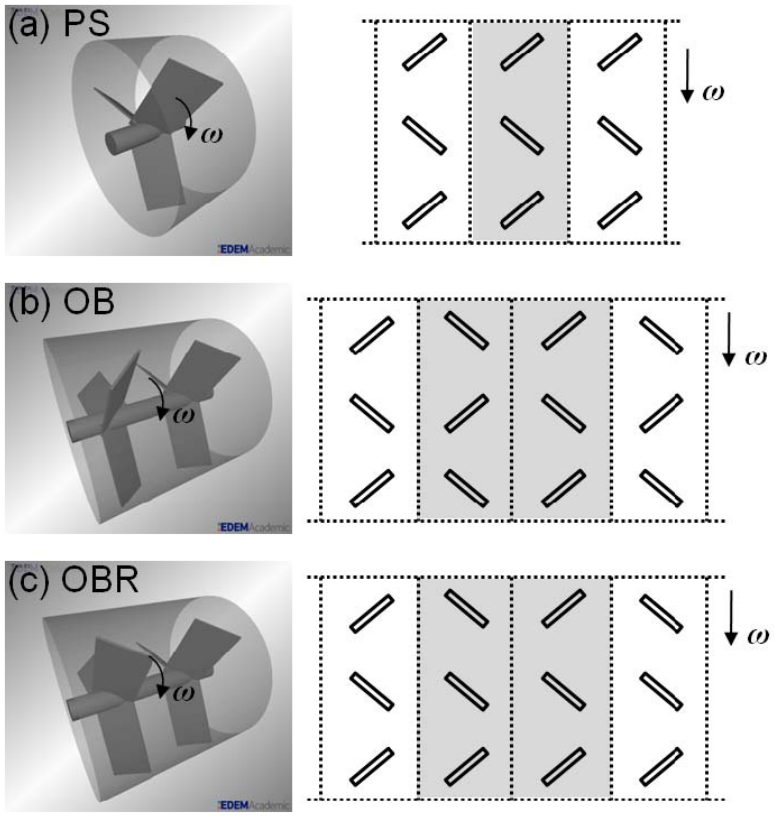

Figure 5.7 Case Study 2: geometries and rotating frame view of blade patterns.

(a) The "partial forward" periodic section (PS). (b) The "partial alternate" open ended batch section, with two PS elements symmetrically connected (OB). (c) The "partial alternate" open-ended batch section, with the first PS element symmetrically connected, and then rotated along the direction of ω for the angle 120° (OBR). Dotted lines in the rotating frame are the periodic boundaries.

The velocity field representations of the three geometries examined in this Case Study are plotted in Figure 5.8. Due to the motion of the backward blade, zigzag velocity fields following the direction of the blades are found in all three geometries. This suggests

improved mixing conditions than in the first Case Study, since the zigzag flux pattern reduces the distance between adjacent convective fluxes.

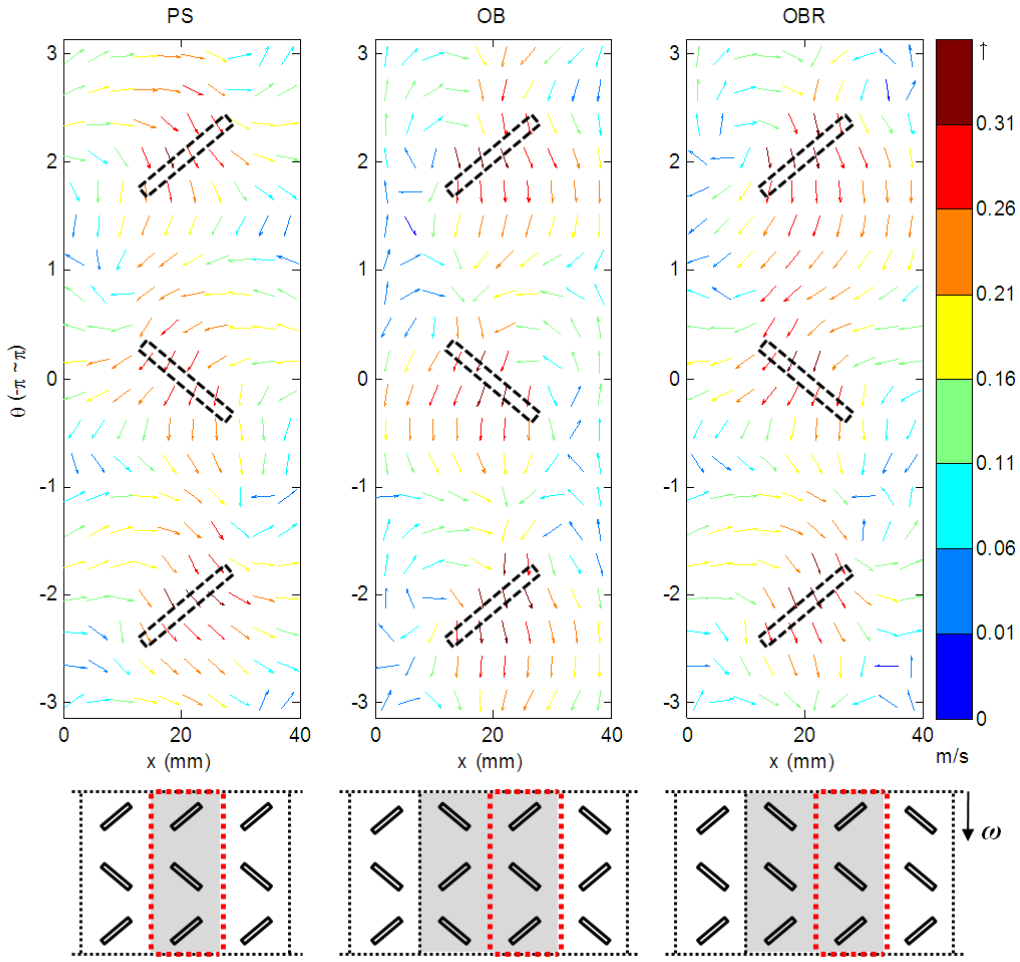

Figure 5.8 Velocity quiver plots of Case Study 2.

The regions enclosed by the red lines in the rotating frame view of blade patterns are plotted. PS, the "partial forward" periodic section; OB, the "partial alternate" open-ended batch section, with two PS elements symmetrically connected; OBR, the "partial alternate" close-ended batch section with the first element rotated $2\pi/3$ in the direction of ω.

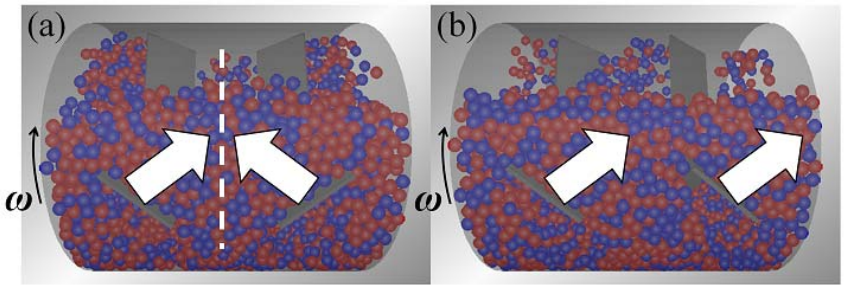

Figure 5.9 (a) Symmetric and (b) parallel blade pairs.

Fluxes of particles impinge in the center of the symmetric blade pairs, leading to the effect similar to a solid end wall between the two blades. This effect is not observed in the rotation of parallel blade pairs.

Different number of symmetric blade pairs are observed in the geometries (Figure 5.7). Three pairs are found in the OB, one pair in the OBR and no pair in the PS. Since the symmetric pairs of blade motion produce symmetric fluxes impinging in the middle of the blades, this leads to an effect similar to that of the end walls in the CB geometry of Case Study 1 (Figure 5.9). As a result, convective recirculation is expected to occur between the symmetric blades and the periodic boundaries in the velocity fields of both the OB and the OBR geometries. The intensity of convective recirculation is expected to be proportional to the number of symmetric blade pairs. Based on the number of convective recirculation, we expect the fastest mixing in the OB, followed by the OBR, and then the PS geometry.

The fill level profiles of the regions enclosed by the red line in Figure 5.8 are calculated and plotted in Figure 5.10. Due to the effect of the backward blade, the peak of the fill level profile in the PS is shifted leftward compared to that in Case Study 1, leading to a more symmetric profile. While two PS elements are oppositely connected in constructing the OB and OBR geometries, the fill level profiles are symmetric through two PS elements. Here,

the profiles of only the second element are plotted. It is found that two peaks are formed in the OB: the high peak at the right end of the space (40 mm) and the low peak at the left end (0 mm). The difference comes from the number of blades pushing particles to those areas. As four forward blades are set directing particles to the right end of the geometry, more particles accumulate there, leading to the formation of the high peak. Similarly, motion of two backward blades forms the low peak to the left end. On the other hand, since only two forward blades propel particles to the right end and no blades propel to the left end, the OBR geometry has detectable influence on attenuating the two peaks than the OB.

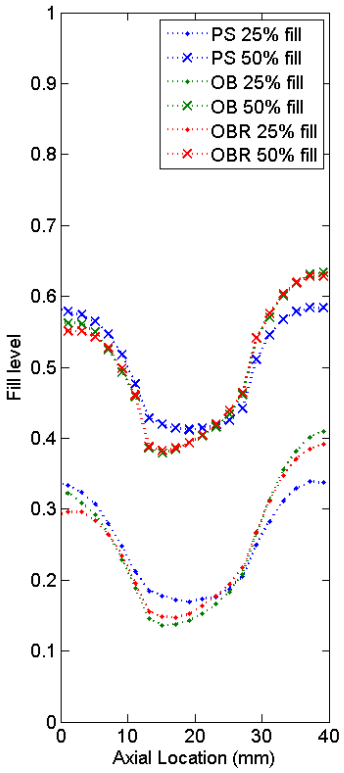

Figure 5.10 Fill level profiles along the axis of the simulated geometries in Case Study 2 for the regions enclosed by the red lines in Figure 5.8.

The RSD decay curves of these geometries in this Case Study are plotted in Figure 5.11. As compared to Case Study 1, introduction of backward blade in the PS geometry increases the similarity of mixing rates in the different geometries: while slight increase of the mixing rates are found in all geometries of this Case Study, the numerical differences of kb between geometries are reduced. At 25% fill, the RSD decay curves almost overlap, while at 50% fill, mixing rate increase slightly from the PS to the OBR and then to the OB, following the number of symmetric blade pairs in each geometry. This suggests that the effect of symmetric blade pairs is significant only at 50% fill, which can be explained that the impinging of particle fluxes in the middle of the symmetric blade pair is similar to the impinging towards an end wall only when that region is highly filled (Figure 5.9). When the local fill level in that region is low, this effect is not significant.

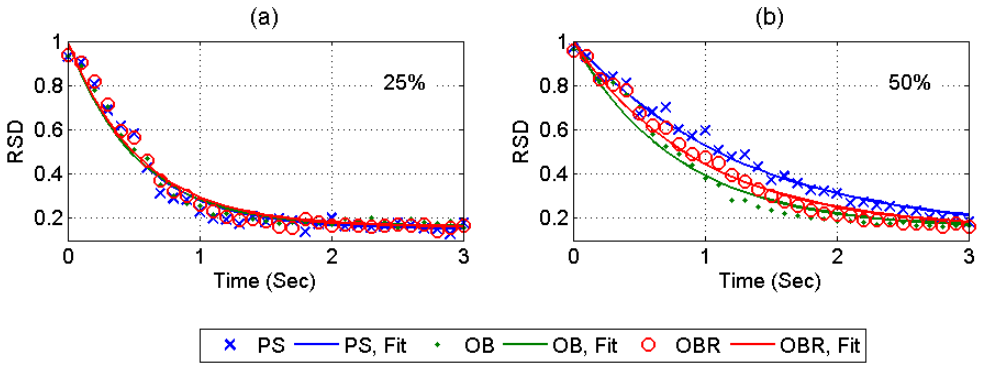

Figure 5.11 RSD decay data and the fitted curves for Case Study 2. (a) 25%, (b) 50% fill.

Based on these results, we believe that introducing backward blade into the PS improves the similarity of mixing performance between the PS and the batch mixers. Symmetric blade pairs in the "alternate" mixing geometries lead to better mixing performance in high fill level mixing cases, which is preferred in the design of continuous mixer with

"alternate" blade patterns. On the other hand, less symmetric blade pairs indicate more similarity between the mixing of the "forward" and "alternate" mixing geometries, and thus can be considered in the design of small batch mixers that could be used for estimating the mixing performance of corresponding continuous mixers consisting of the "partial forward" PS elements.

3.3 Case Study 3: effect of blade axial location

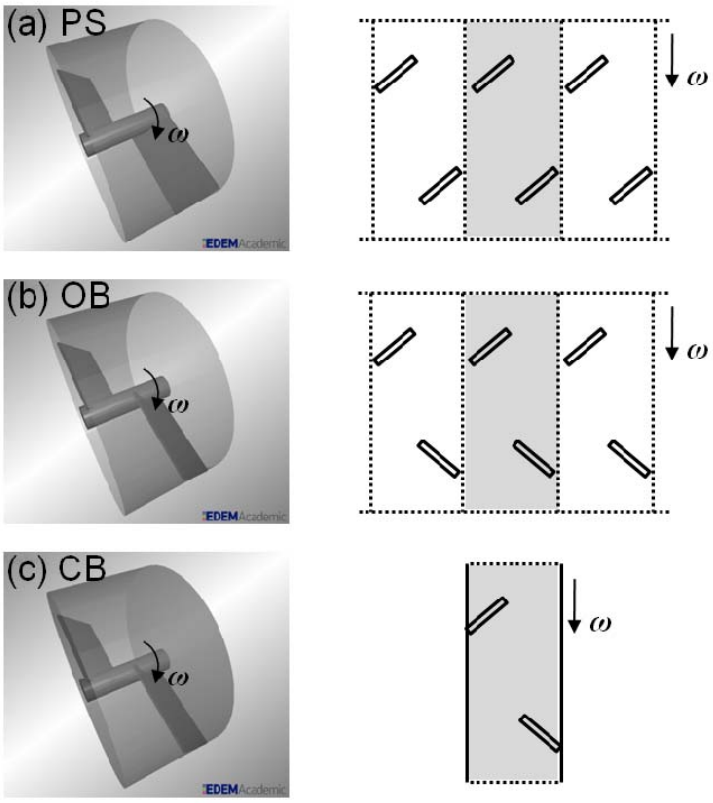

Figure 5.12 Case sutdy 3: geometries and rotating frame view of blade patterns.

(a) The "all forward" periodic section with blades located in different positions (PS). (b) The "all alternate" open ended batch section with blades located in different positions (OB). (c) The "all alternate" close ended batch section with blades located in different positions

(CB). Dotted lines in the rotating frame are the periodic boundaries, and solid lines indicate end walls.

Up to now, all the blades in all the geometries are always located in the middle of each element. This leads to significant heterogeneity of fill level along the axis. The mixing rate in these cases depends not only on the local fill level at the blade axial position, but also on the exchange rate of materials between the blade area and the rest of the element along the axis. When different fill level profiles are formed in these geometries, the exchange rates of materials along the axis may not be the same, which is probably one reason leading to the observed differences in mixing performance. To further examine this effect, the blades were placed at different axial positions, the purpose of which is to form a more uniform fill level profile for both the PS and other geometries. In this Case Study, the geometries of the PS, the OB and the CB are very similar to those in the Case Study 1, except that the two blades are located at different sites (at 10mm and 30mm along the axis of shaft, instead of at 20mm in the middle of each cross-sectional element). The geometries and the rotating frame view of blade patterns are shown in Figure 5.12.

The velocity fields in this Case Study are examined and plotted in Figure 5.13. While the velocity fields of both the PS and the OB in this Case Study are similar to that in Case Study 1, a convergence point at the center of the rotating frame is observed in the OB of the current Case Study, instead of the shear region observed in Case Study 1. This suggests a smaller mixing rate in the OB geometry in the current Case Study. Furthermore, in the velocity field of the CB, the distance for the particles propelled by one blade to reach the opposite end wall is longer (30 mm) compared to that of Case Study 1 (20 mm), which

suggests that fewer particles will impinge directly onto the end walls. Thus, a smaller end wall effect is expected in the current Case Study, which may give rise to the lesser difference between the mixing rates of the PS and the CB geometries.

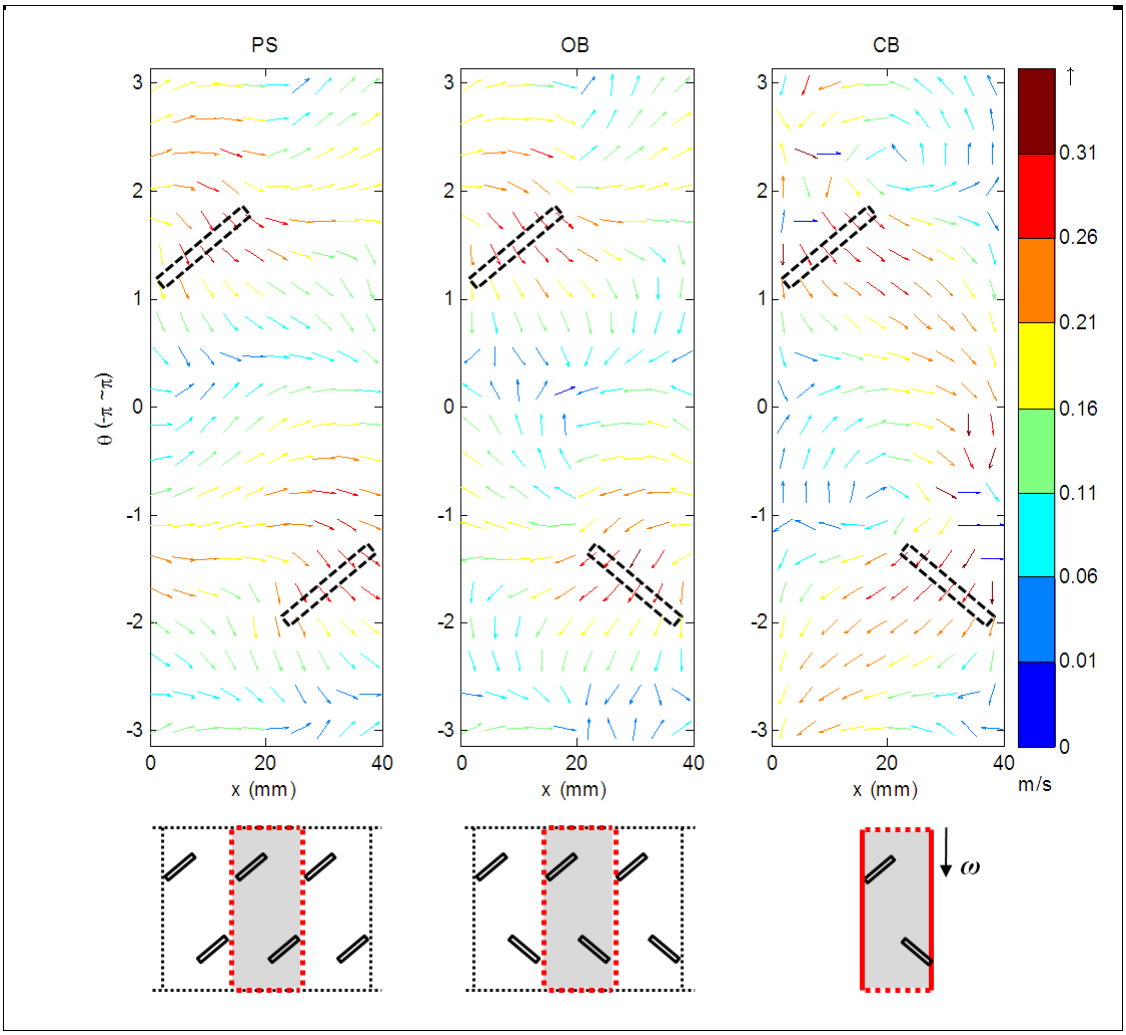

Figure 5.13 Velocity quiver plots of Case Study 3.

The regions enclosed by the red lines in the rotating frame view of blade patterns are plotted. PS, the “all forward” periodic section with blades located in different positions; OB, the “all alternate” open-ended batch section with blades located in different positions; CB, the “all alternate” close-ended batch section with blades located in different positions.

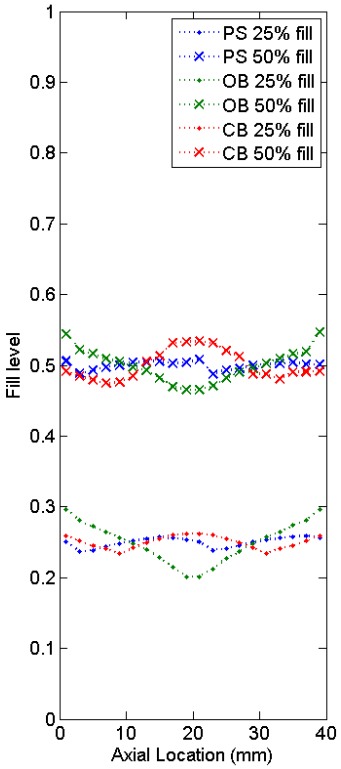

Figure 5.14 Fill level profiles along the axis of the simlated geometries in Case Study 3.

The fill level profiles of this Case Study are plotted in Figure 5.14. Significant decrease of axial fill level fluctuations are observed for both fills, compared to previous Case Studies. Fluxes induced by the blades deliver materials to the next blade in the PS, or transfer materials to the other blade in the OB and the CB, so that local fill level at both blade positions do not vary much. The slight difference between the PS and OB profiles results from the difference between the distance particles are propelled by a single blade motion (28 mm), and the distance of locations of the two blades (20 mm). For the CB geometry, as illustrated above, fewer particles propelled by one blade are expected to reach the opposite end wall; however, since the distance between the blade and the opposite wall (30 mm) is

approximately the same as the average distance that particles move in a single blade motion (28 mm), there is still a considerable number of particles impinging on the end walls and being reflected, which possibly leads to the slightly larger fill level in the middle of the element. For all three geometries, as the fill level profiles are less fluctuated than in Case Study 1, mixing contidions are expected to be more similar in the current Case Study.

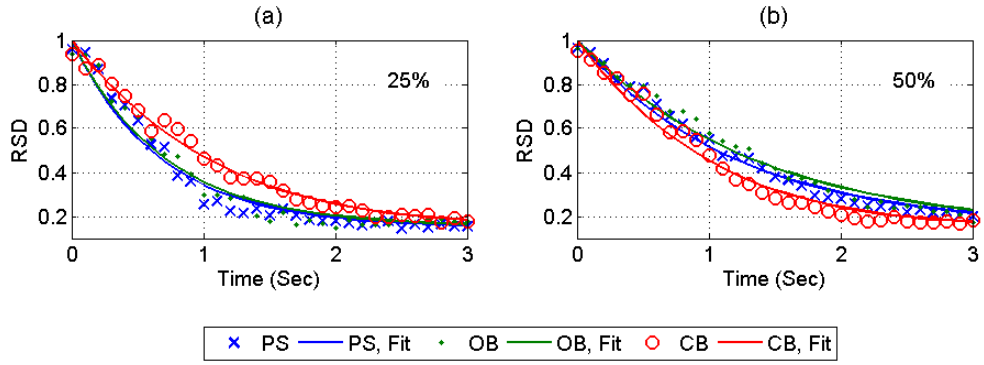

Figure 5.15 RSD decay data and the fitted curves for Case Study 3. (a) 25%, (b) 50% fill.

The results of mixing simulations are plotted in Figure 5.15. It is found that under current sampling size, the CB mixing rate is slightly faster than the other two geometries at 50% fill, but is slightly slower at 25% fill. While the faster mixing at 50% fill level can be explained due to the effect of solid boundaries, the slower mixing at 25% fill level is different from Case Study 1, which may result from the close distance between blades and the ipsilateral boundaries. This effect requires further investigation. By comparing the mixing rate k_b of Case Studies 1 and 3, smaller CB mixing rates are observed for both fills when blades are in different positions, which leads to an increased similarity of mixing rate between the CB and the PS. As suggested above, this increased similarity results from a more uniform fill level profile and a decreased end wall effect in the current Case Study.

On the other hand, RSD decay curves of the OB overlap with these of the PS for both fills. This result shows satisfactory similarity, which suggests that besides the issues of end walls and backward fluxes, keeping uniform fill level profile is also an important issue in achieving similar mixing rates between different cross-sectional elements. Based on these results, by constructing a batch mixer following the issues identified in the three case studies, it is possible to estimate the cross-sectional mixing of a continuous mixing process with similar geometries.

5.3 Summary

This work examines the cross-sectional mixing performance of several elemental geometries in order to determine the effect of blade orientation, and characterize the impact of circulation patterns in continuous powder mixers. An additional goal of the work presented here is to determine whether a physically realizable batch mixer can be used to study the cross-sectional component of the mixing process in a flow-through continuous mixer. Two methods are used to perform these assessments. Two-dimensional quiver plots of the velocity field, averaged in the radial directions, are used to examine qualitatively the motion of particles in the various geometries. The mixing rate, which is represented by the RSD logarithmic decay rate k_b at a given fill level and sampling size, is used as the index to compare mixing performance. In addition, fill level profiles are calculated to examine their possible effects on mixing.

Several effects were readily apparent from the first case study, which examined three elemental geometries with only two blades: (1) The orientation of the blades, and the presence of solid walls, profoundly affected the motion patterns of particles in the elemental geometry. (2) Backward-oriented blades created visible convective recirculation,

characterized by convective backward flux in the axial direction. These blades also clearly enhanced the mixing rate, reinforcing previous observations regarding the achievement of more efficient mixing in spatially periodic continuous mixers with alternate blade configurations. (3) The effect of solid walls at the axial ends of the elemental geometry significantly enhanced mixing performance, indicating that an experimentally realizable batch mixer with an elemental geometry, albeit convenient, would not be a representative system in which to study cross-sectional mixing processes for a continuous system. (4) For this case study, where all blades were placed at the same axial position, significant fill level gradients in the axial direction were observed, in agreement with simulations (and experiments) of spatially periodic continuous mixers

These effects were further studied in the second case study, which examined systems with three blades at each axial position, and where pairs of blades in mirror-symmetric configurations were used to approximate the effect of solid walls. Once again, motion patterns readily revealed the effect of blade patterns on the intensity of recirculation. Moreover, differences in mixing performance, while still present, were significantly less intense than for the first case study, and the mixing rate directly correlated to the number of symmetric blade pairs along the mixer axis. As in case study 1, since all blades were placed at the same discrete positions along the axis, intense fill level gradients were observed.

In the final case study, blade pairs were no longer placed at the same axial location, instead, blades were uniformly distributed along the axis. While flow patterns, once again, showed significant differences depending on blade orientation and on the presence of solid walls, this case study exhibited both a much more uniform fill level profile in the axial direction and a greater similarity in mixing rate among the different geometries.

Throughout all the case studies, an additional significant effect was that much faster cross-sectional mixing was observed at lower fill levels. This effect is in agreement with long-established knowledge in many types of batch mixers that show a slower mixing process as fill level increases. However, for a continuous mixer, a lower fill level also implies a shorter residence time, and therefore, slower axial mixing. Thus, in using the simulation results presented here for the design of experimentally realizable mixers, one should bear in mind two final observations: (1) Due to the presence of solid walls, small convective batch mixers will exhibit faster cross-sectional mixing than periodic sections of continuous mixers, and (2) continuous mixers also need to achieve effective axial mixing. Both observations suggest that small batch mixers could overestimate the mixing rate of continuous systems, possibly leading to inadequate design. These issues will be examined further in future communications.

Chapter 6

Strategies on improving blending performance

In this chapter, the previously developed periodic section modeling is used to determine the influence of operating conditions on the performance of continuous blenders. The influence on either the local mixing efficiency or the axial motion of the mixture is separately considered. To understand the applicability of knowledge from successful mixing cases, we focus on (1) a single blending geometry but four different mixing cases, and examine in detail the performance similarity among these cases, and (2) multiply geometry and operation factors on blending performance. The rest of the paper is organized as follows: the simulations of different mixing cases using factorial analysis are discussed in Section 6.1. The influence of multiple factors is investigated using the Projection of Latent Structure (PLS) and validated experimentally in Section 6.2. The summary are presented in 6.3.

6.1 Optimizing continuous powder blending using factorial analysis

6.1.1 Simulation and Methodology

Due to the difficulty involved in experimentally building a cross section with periodic boundaries, we use the Discrete Element Method (DEM) as the tool for examining the operations and mixing cases of interest. Detailed reviews of the DEM application can be found in (Bertrand et al., 2005; Dubey et al., 2011). In this study, the software EDEM® from DEM Solutions is used to develop the desired geometries. The particles simulated are spheres. The physical and numerical parameters used in this simulation are summarized in Table 6.1. The approach has been used in our previous studies (Arratia et al., 2006; Gao et

al., 2011a; Portillo et al., 2007), as well as in a number of previous efforts (Sarkar and Wassgren, 2010; Zhou et al., 2004) and found to be able to accurately capture the dynamics of mixing processes.

Table 6.1 Physical and numerical parameters used in the DEM model.

Parameter	Value			
	Case 1 (Control)	Case 2 (Lighter particles)	Case 3 (Larger particles)	Case 4 (More cohesive particles)
Particle diameter (m)	3×10^{-3}	3×10^{-3}	4×10^{-3}	3×10^{-3}
Particle density (kg m^{-3})	1×10^{3}	0.2×10^{3}	1×10^{3}	1×10^{3}
Cohesion coefficient k (Jm^{-3}) $F=kA$ F: Cohesive force A: Contact area	0	0	0	5×10^{5}

The cross-sectional element representing a periodic section (PS) was constructed from a horizontal cylinder (diameter 80 mm and length 40 mm). Two 40° forward blades (20 mm ×40 mm) were located opposite to each other at different sites of the shaft (at 10 mm and 30 mm along the axis of the shaft) (Figure 6.1). This PS elementary geometry was tested in previous chapters (Gao et al., 2011a), and was found that lead to more homogenous axial fill level distribution and fewer dead spots. In this chapter, it is used to simulate the ideally cross-sectional mixing in an "all forward" continuous mixer with the same fill level and flow rate.

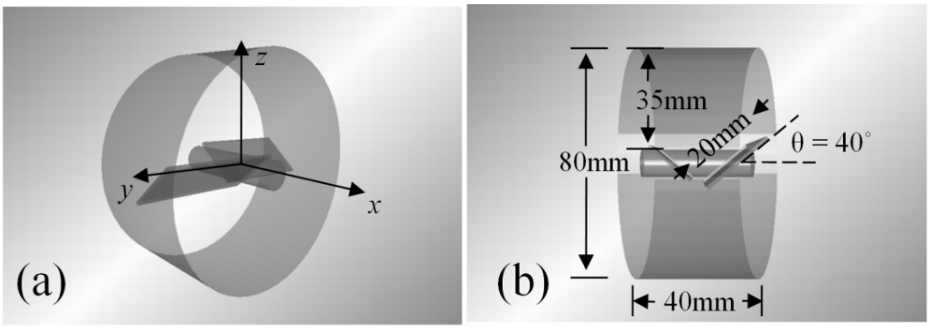

Figure 6.1 Simulated periodic section geometry.

(a) Isometric view of the section. (b) Side view of the section with dimensions displayed.

In order to illustrate similarity among different mixing cases, four kinds of particles different in diameter, density and cohesiveness were used in the simulation (Table 6.1). For simplicity, mixing is performed only using the same kind of particles with different colors, so only non-segregating mixtures are involved in our current study. As shown in Table 1, the first case is considered as the control case, and the other three cases are different based on one particle property. For each of the four cases, three fill levels (25%, 50%, 75%) and four blade speeds (40, 100, 180 and 250 RPM) were simulated, thus a total number of 12 sample points are considered.

Equation (4-8) indicates the two key indices k_b and v_x for continuous powder mixing processes. It was proposed and validated in Chapter 4, where up to 4500 particles per periodic section were simulated. To determine the impact of the number of particles on the validity of this relationship, simulations with a larger number of particles are performed for the same geometry as in the original paper. The geometry is similar to that in our current study, except for the location of the two blades. Eight sections of the same geometry are linearly connected to simulate the corresponding continuous blender. The new particles are

2 mm in diameter, which are 1.5 times smaller than the original ones. As a result, 7560 particles per periodic section are simulated representing a 25% fill level, and the corresponding feed rate in the continuous blender is set as 11440 particles per second for each component. A sampling size of 110 particles was used in the RSD calculations and the results are plotted in Figure 2. While the fitted value of k_b is 1.71 s^{-1}, and RSD_{SS} is 0.0930 under the sampling size of 110 particles, the mean axial velocity v_x is 121 mm/s for both simulations, leading to the predicted value of k_b as 0.0141 mm^{-1}. Figure 6.2b indicates the validity the model when more particles are simulated. It should be noted that the prediction was performed only in the first six sections (0 -240 mm) as fill level decreases dramatically in the last two sections due to discharge effects.

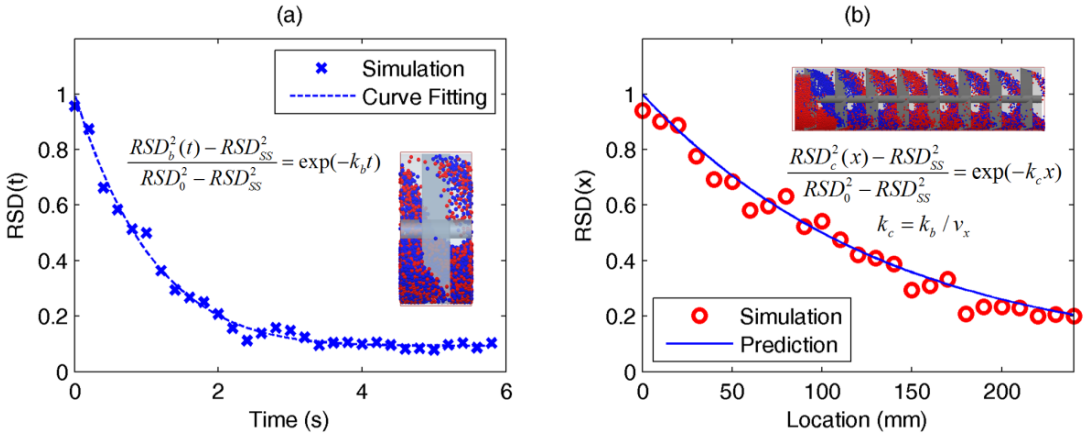

Figure 6.2 Validation of periodic section modeling with more particles.

(a) Batch-like RSD decay data in periodic section. Dot line is the fitted curve. (b) RSD decay data in the corresponding continuous blender. Solid line is the predicted decay curve through the calculation of k_c.

6.1.2 Factorial analysis results

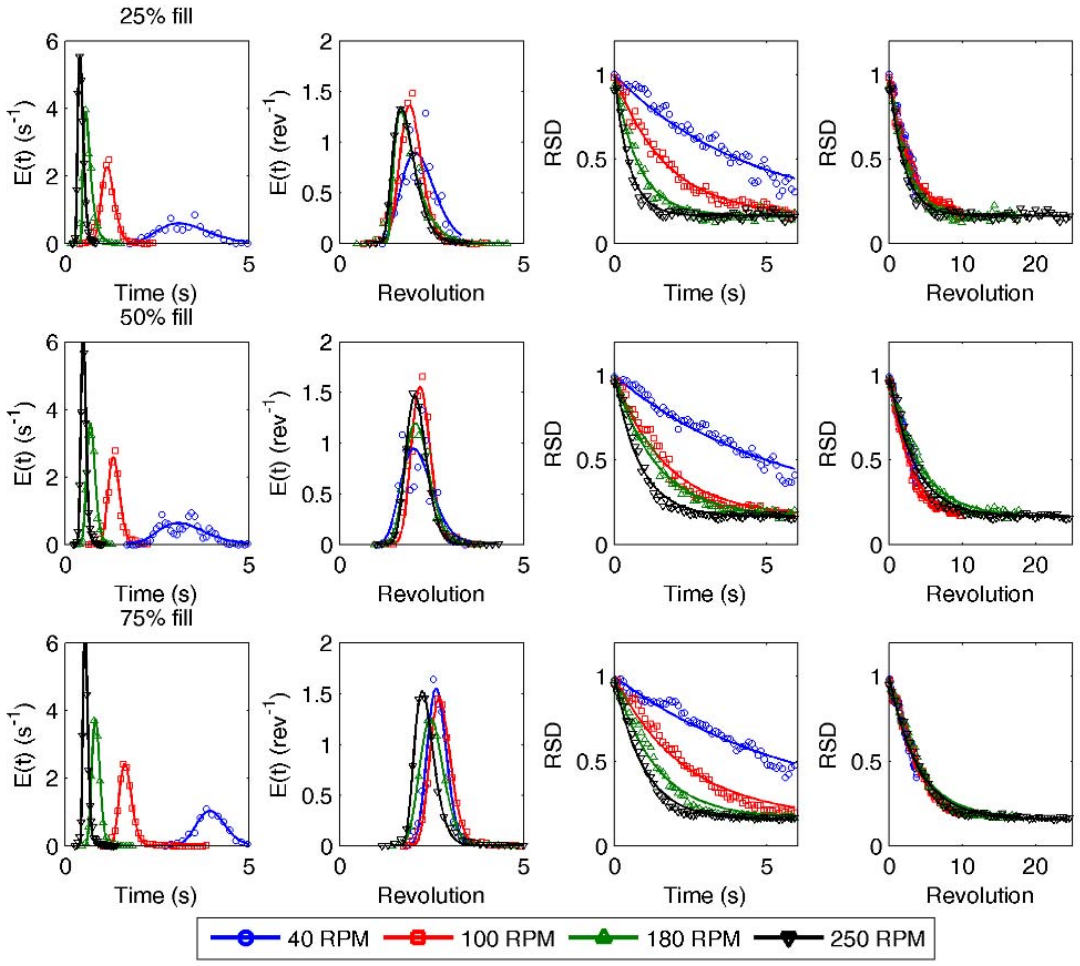

Figure 6.3 The control case: simulated, fitted, and normalized RTD and RSD-t curves for different operating conditions.

Figure 6.3 summarizes the RTD and RSD-t curves of the control case. Using the data derived from the particle-trajectory method and the cube-sample method, v_x and k_b are determined using the least squares method. As shown in recent studies from our group (Portillo et al., 2010; Vanarase and Muzzio, 2011), the mean residence time of continuous blending is approximately anti-proportional to rotary speed of blades. Meanwhile, earlier studies on batch blending (Brone et al., 1998; Brone and Muzzio, 2000) reveal the

proportionality between batch mixing rate and rotation rate of blenders, indicating that a similar relationship should exist between the mixing rate and blade speed in the periodic section blending. To normalize the effects of blade speed on mixing and axial velocity, RTD and RSD-t curves are replotted versus revolution (Figure 6.3, the second and fourth columns), instead of versus time (Figure 6.3, the first and third columns). Results are compared for different blade speeds and fill levels. In the normalized plots, mean residence time and mixing process are independent of blade rotary speed, while both mixing and axial delivery of particles are a little bit faster at low fill levels. The corresponding mean axial velocity and mixing rate, normalized over rotary speed, are calculated as:

$$v_x' = v_x / \omega \qquad 6\text{-}1$$

$$k_b' = k_b / \omega \qquad 6\text{-}2$$

where ω is the blade speed measured as revolution per second. Notice that k_b' measures mixing rate as RSD decay per revolution, and v_x' measures axial velocity as millimeters per revolution. The influence of operating conditions on both indices for different mixing cases is analyzed as follows.

Based on the above results, the influence of fill level and rotary speed on the normalized mean axial velocity is plotted in Figure 6.4. It is noticed that the axial displacement during each blade revolution increases with increasing rotary speed and decreasing fill level. While the first three cases depict similar contour profiles, the more cohesive particle case is found to be slightly different. Due to the cohesiveness in this case, the maximal value of vx' is not as large as in other cases, while the minimal value is found at a moderately low blade speed (100 RPM) and large fill level (50% -75%). However, the overall trend in this case is similar to the other three cases, thus is not affected by the different particle

properties. Results are compared with axial velocity data provided by Sarkar and Wassgren (2009), where flow and dispersion of particles were investigated in periodic slices with similar geometry. Although scales of geometry, particle properties, and operations are much different in their work, similar trends for the normalized axial velocity were observed.

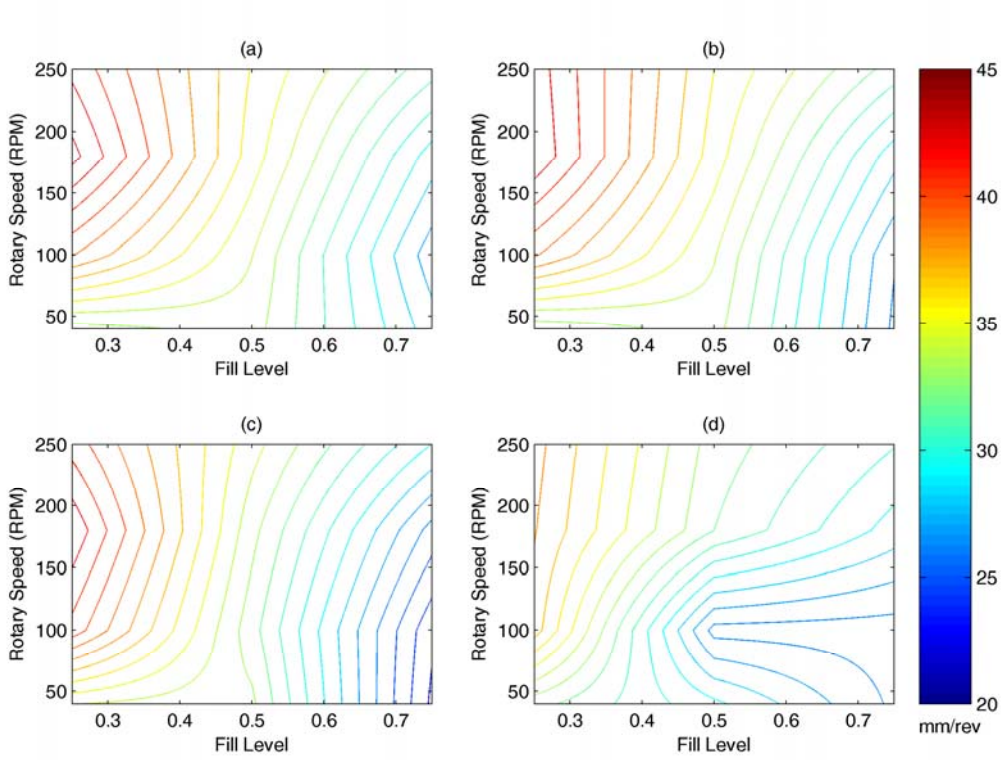

Figure 6.4 Contours of normalized mean axial velocity vx' in the design space of operation.

(a) Control case. (b) Lighter particle case. (c) Larger particle case. (d) More cohesive particle case. Unit: mm/revolution.

Figure 6.5 plots contour of the normalized mixing rate kb' in a periodic section for each blending case. In the interest of clarity, we mainly focus on the region where large value of

kb' are observed. Similar to the analysis of v_x', more efficient local mixing is found with greater rotary speeds and lower fill levels for all four cases. For the first three cases (Figure 6.5a-c), since bulk material tends to rotate with blades as one whole piece when blade speed is high, rapid blade rotation and high fill level lead to slow local mixing. However, slow mixing is also found at low blade speed and high fill for the more cohesive particle case (Figure 6.5d), indicating a significant effect of cohesion in that condition.

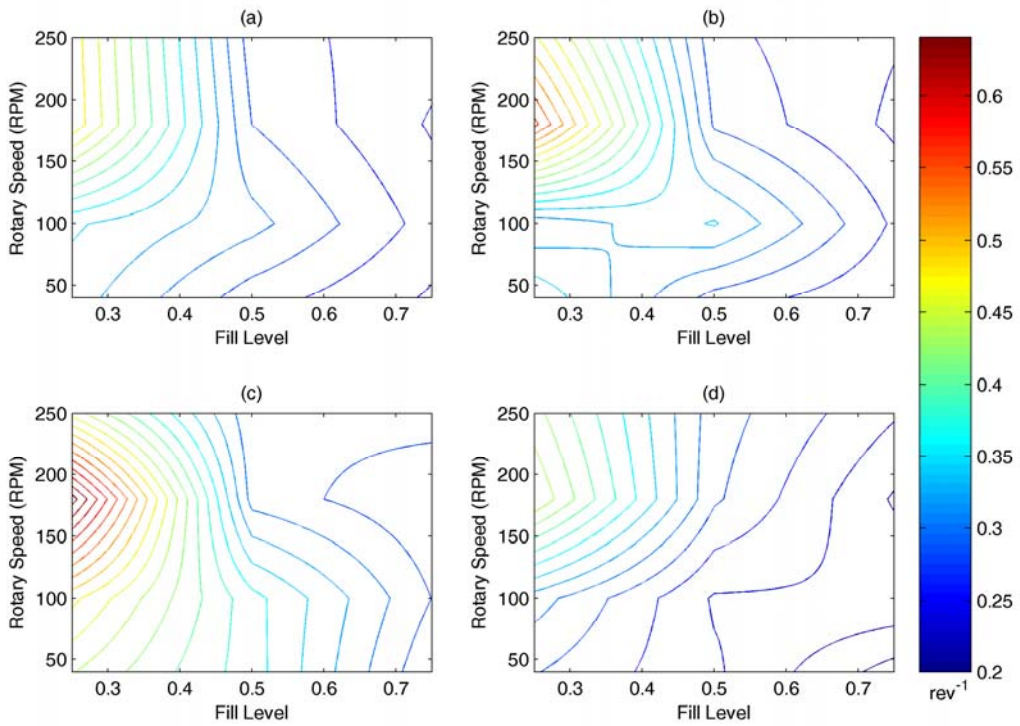

Figure 6.5 Contours of normalized PS mixing rate k_b' in the design space of operation. (a) Control case. (b) Lighter particle case. (c) Larger particle case. (d) More cohesive particle case. Unit: revolution^{-1}.

As Figures 6.4 and 6.5 indicate, while an efficient local mixing rate is observed at high blade speed and low fill level, large axial velocity is also observed. Thus, to achieve the

optimal mixing performance we have to balance those competing trends. As Figure 6.6 shows, large values of kc, representing efficient continuous mixing performance, are found at high rotary speed and low fill level for all blending cases. Since this optimal condition is the same as in the contours of k_b, it indicates the dominant role of local mixing rate in its competition with axial velocity on determining the continuous blending performance. Figure 6 also leads to an interesting point: despite of various local mixing rates and axial velocities, the optimal operating condition is the same for all mixing cases. Thus, when operating conditions are optimized and lead to one successful continuous mixing process, it is possible to apply this optimized condition to new mixing cases, when the same mixer is used.

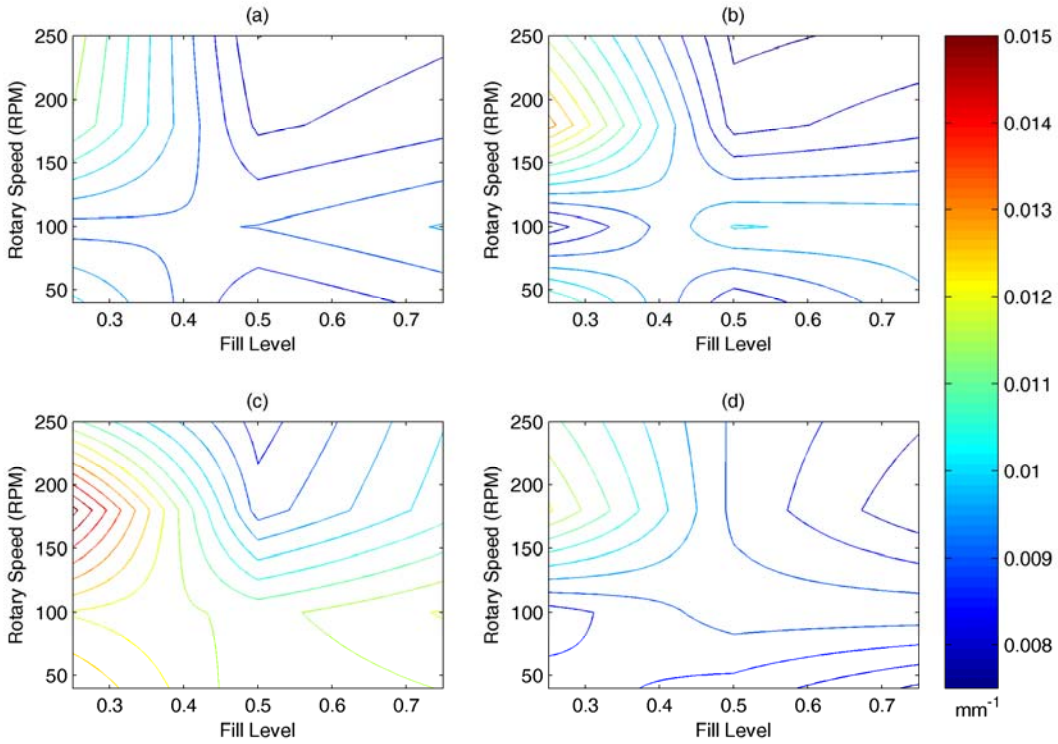

Figure 6.6 Contours of continuous blending rate kc in the design space of operation.

(a) Control case. (b) Lighter particle case. (c) Larger particle case. (d) More cohesive particle case. Unit: mm^{-1}.

6.1.3 Improvement of mixing performance

As indicated above, increase of blade speed leads to an increase of both the local mixing efficiency k_b and the axial velocity v_x. Following the strategy of altering the blade speed, although an optimal operation can be found to maximize the continuous blending rate k_c, there is a significant trade-off between the fast axial motion and the fast local mixing in the optimal operating condition. In other words, the increase of axial velocity along with the ascending blade speed is not preferred in optimizing the continuous blending performance. If we can keep the axial velocity constant through the increase of blade speed, while the increase of the local mixing rate through the same process is not affected, the trade-off effect between the two indices can be eliminated, and the continuous blending performance can be further improved.

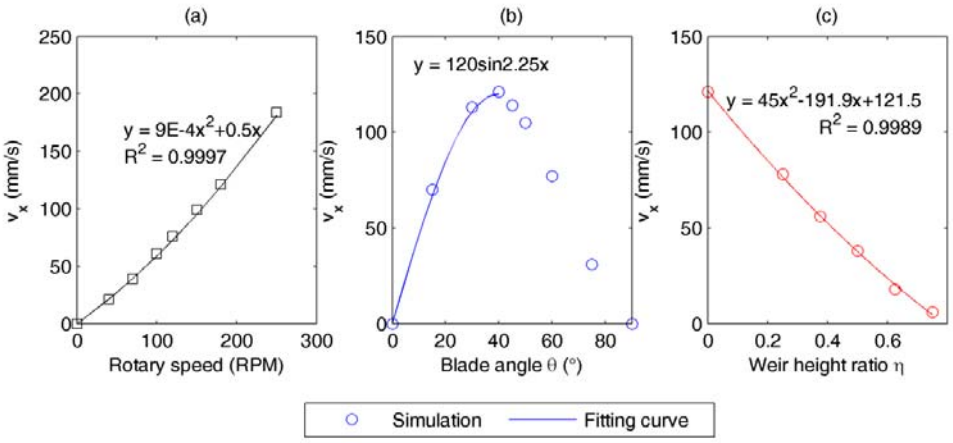

Figure 6.7 Effect of (a) rotary speed, (b) blade angle, and (c) weir height on the mean axial velocity v_x, the control case.

To test the proposed approach for improving the mixing performance, the 25% fill simulations of four blade speeds (40, 100, 180, and 250 RPM) were used as control cases. To counterbalance the increase of axial velocity through the increase of blade speed, we need operations that can decrease the axial forward flux. Our previous study (Gao et al., 2011a) shows the effect of blade angle: axial velocity decreases with decreasing blade angle. Another study (Vanarase and Muzzio, 2011) also indicates the effect of weir at the discharge on hindering axial flow, which leads to a decrease of axial velocity. Based on these studies, two strategies are proposed to improve the continuous blending performance: (1) decreasing blade angle while increasing blade speed; (2) increasing weir height at the end of the PS while increasing blade speed. The key to both strategies is to keep the axial velocity constant through the increase of blade speed. For this purpose, additional simulations were performed. Based on the case of 25% fill, 180 RPM simulation, the effect of blade angle and weir height on the axial velocity were simulated, as plotted in Figure 6.7. The corresponding fitted curves of these effects, as well as the effect of blade speed on axial velocity, are determined. To find the corresponding blade angle and weir height that keeps the axial velocity constant while increasing the blade speed, we assume the effects of blade angle, blade speed and weir height on the axial velocity are independent from each other and can be described as follows:

$$v_x(\omega,\theta,\eta) = f_1(\omega) f_2(\theta) f_3(\eta) \qquad 6\text{-}3$$

where ω is the rotary speed measured as RPM, θ is the blade angle and $\eta=h/d$ the weir height ratio (h the height of the weir and d the diameter of the cylindrical mixing space).

Applying equation (13), the value of v_x *(180RPM, 40°, 0)=121.5 mm/s*, and the fitted equations from Figure 6.7, we get the following relationships:

$$v_x(\omega,\theta,\eta=0)=\frac{1}{121.5}(9E^{-4}\omega^2+0.5\omega)\sin 2.25\theta \qquad 6\text{-}4$$

$$v_x(\omega,\theta=40^\circ,\eta)=\frac{1}{121.5}(9E^{-4}\omega^2+0.5\omega)(48\eta^2-191.9\eta+121.5) \qquad 6\text{-}5$$

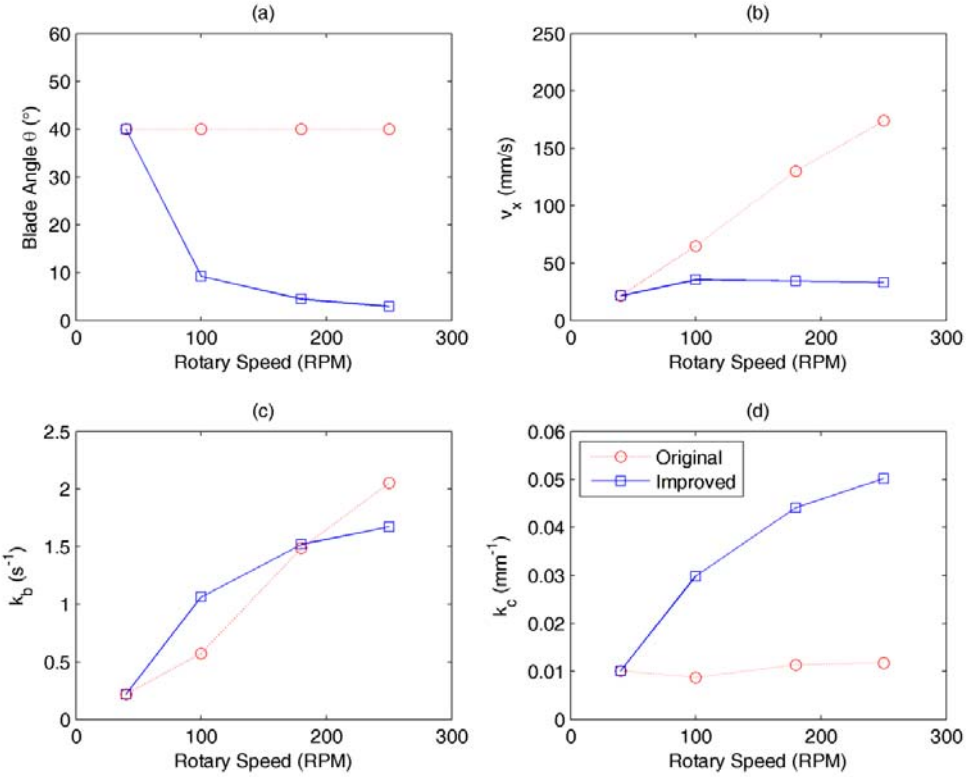

Figure 6.8 Performance improvement strategy 1.

Simulations are compared in (a) design of blade angle, (b) axial velocity, (c) local mixing rate in PS, and (d) continuous mixing rate.

Since the value of v_x *(40RPM, 40°, 0)=21.7 mm/s* is used as the initial value of axial velocity, the same value should be kept constant as the blade speed increases. Using

equations (6-4) and (6-5), the corresponding blade angle and weir height are calculated. As a result, blade angles 10°, 5°, and 3° are considered for the blade speeds of 100, 180, and 250 RPM, respectively in the first performance improvement strategy; and weir height ratios 0.455, 0.615 and 0.67 are considered for the corresponding blade speeds in the second strategy. The six new designs with altered blade angle or weir height were simulated, and the values of k_b, v_x, and k_c were then calculated and compared with the control group.

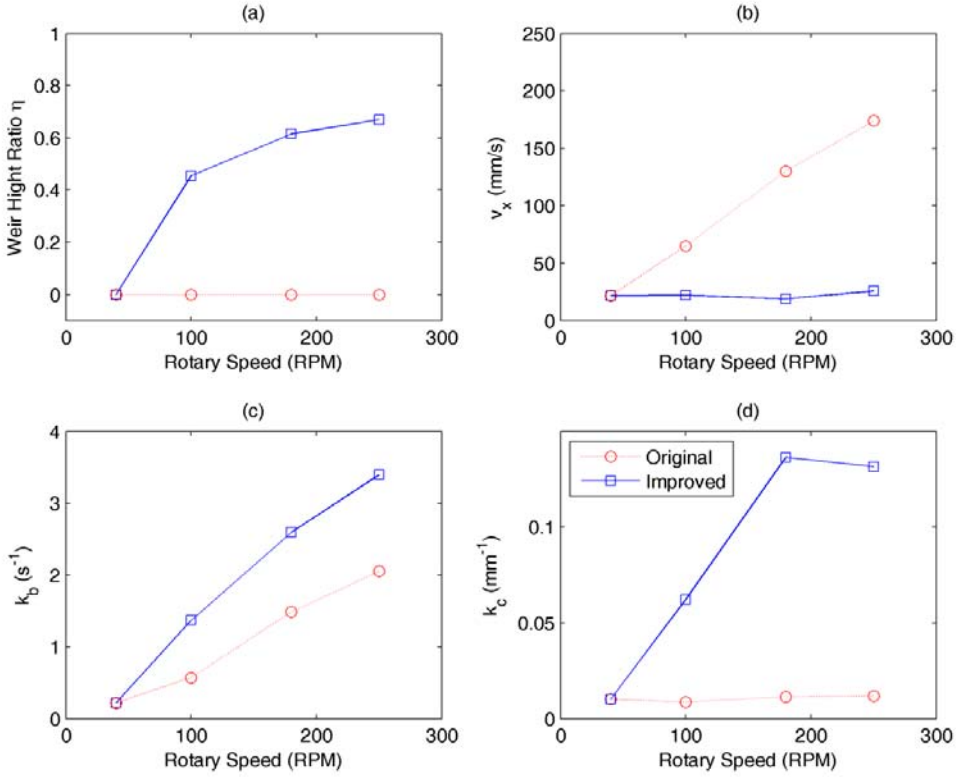

Figure 6.9 Performance improvement strategy 2.

Simulations are compared in (a) design of weir height ratio, (b) axial velocity, (c) local mixing rate in PS, and (d) continuous mixing rate.

Results of both strategies are summarized in Figures 6.8 and 6.9, respectively. As shown in the figures, k_b in the improved cases are almost the same as in the control group in strategy 1 (Figure 6.8c), and is a little bit larger in strategy 2 (Figure 6.9c), which is due to the backward flux introduced by the weir. However, the improved designs lead to a constant value of axial velocity for both strategies (Figure 6.8b, 6.9b), which result in dramatic improvements of the continuous blending performance. As a result, the continuous blending rate k_c increases by five fold in strategy 1 (Figure 6.8d) and nine fold in strategy 2 (Figure 6.9d), which indicates that the necessary sections in the corresponding continuous blending systems can be significantly reduced. Once again, these performance improvement results demonstrate the applicability of the periodic section modeling in understanding the continuous blending performance at various operating conditions and design specifications.

6.2 Application of PLS and experimental validation

6.2.1 Discrete Element Method (DEM)

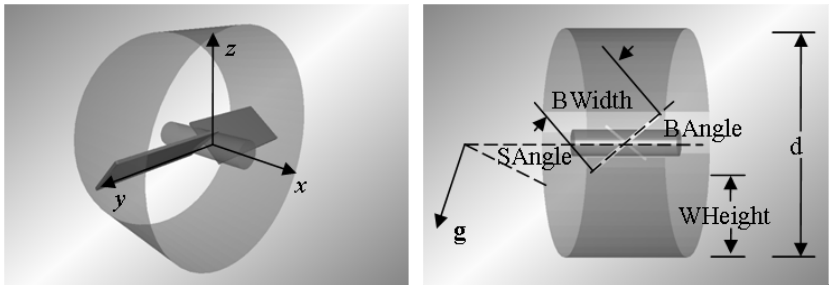

Figure 6.10 Geometry of the periodic section.

(a) Isometric view. (b) Side view. g, gravity. d, diameter. SAngle, shaft angle. BWidth, blade width. BAngle, blade angle. WHeight, weir height.

A periodic section geometry similar to Figure 6.1 is constructed with variable parameters (Figure 6.10). It simulates the ideally cross-sectional blending in an "all forward" continuous blender. To understand the effects of operations and geometry on the blending performance, six factors are investigated: rotary speed, fill level, shaft angle, blade angle, blade width, and weir height (Figure 6.10b). Here the shaft angle indicates the upward or downward direction of the blender (Portillo et al., 2008b); the weir height is designed to control holdup inside the section (Vanarase and Muzzio, 2011). The range of each factor is set following the range applied in previous factorial studies and listed in Table 6.2.

Table 6.2 Range of operation and geometry factors in this paper.

Design parameters	Lower bound	Upper bound
Blade speed (RPM)	40	250
Blade angle (˚)	10	40
Blade width (mm)	10	40
Weir height ratio h_w/d (-)	0%	75%
Fill level (-)	25%	75%
Shaft angle (˚)	-30 (upward shaft)	30 (downward shaft)

6.2.2 Projection to Latent Structure (PLS) regression

The theory of Projection to Latent Structure (PLS) is widely applied to understand the behavior of complicated systems characterized by a large number of variables. It is a generalization of the Multiple Linear Regression, where data that are strongly collinear and noisy can be analyzed. In brief, PLS regression is a method to relate two data matrices, X and Y, the predictor variables and the response variables, while the principle components in each data matrix are also summarized. Two sets of weights denoted w and c are created in order to achieve linear combination of the columns of X and Y so that their linear transformations of variables have maximal covariance (Reiss et al., 2010). Mathematically,

the goal is to obtain a pair of vectors w and c that satisfy the following optimization problem:

$$t = Xw \text{ and } u = Yc \tag{6-6}$$

$$\max_{w,\,c} t^T u$$
$$st.\ w^T w = 1,\ t^T t = 1 \tag{6-7}$$

The optimized vector pair w and c are called loading scores of the investigated system. The relationship between loading scores in each principle component indicates the influence of predictor variables on response variables (Abdi, 2010). The advantage of the PLS regression is that less samples are needed compared to the factorial analysis. For the six-factor system analyzed in this paper, only 64 samples are required to cover the operation and geometry design space, while the same number of samples cover only the upper and lower bounds in a factorial analysis. The Latin-hypercube sampling is applied to achieve homogeneous distributed samples in the six-dimensional design space, in which each sample is the only sample in each axis-aligned hyper-plane containing it. This avoids bias of sample distribution that may influence the PLS analysis result.

For each operation and geometry condition, red and blue particles are loaded side-by-side at the desired fill level in the periodic section. Blending is then simulated for 10 seconds. When the simulation is finished, cubes with a side length of 10 mm were considered in the section. All samples in each interval of 0.5s of the simulation process were considered as the samples at the same time point. The number of particles that can be randomly packed within the sampling sizes of 0.75cm^3 (around 35 particles) is used as the sample size. After enough samples are retrieved, the RSD decay rate k_b and the mean axial velocity v_x are

calculated. When information of the key indices (k_b and v_x) is ready for all simulations, PLS analysis is performed.

6.2.3 Experimental validation

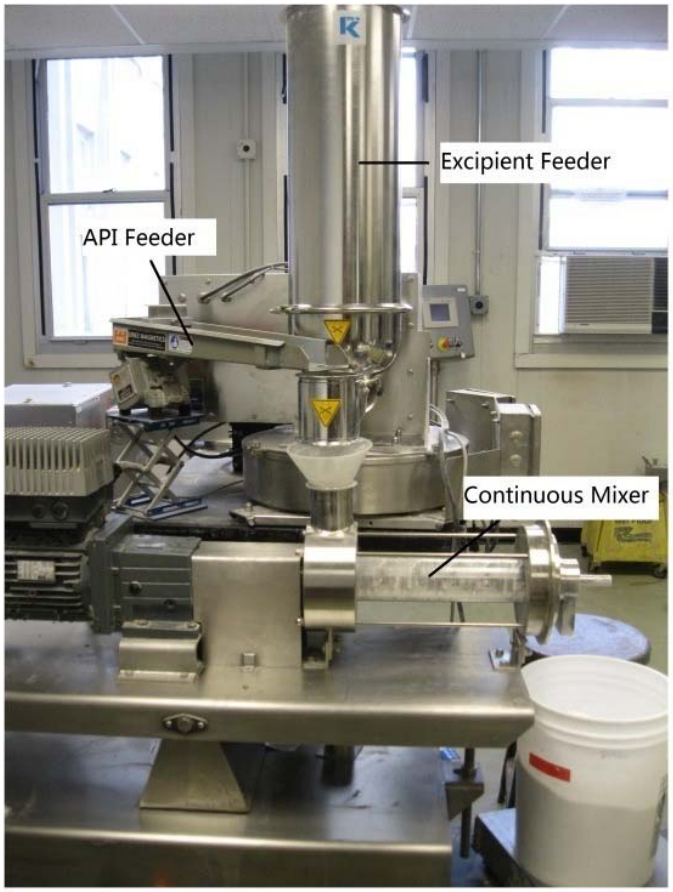

Figure 6.11 Experimental setup.

The setup of the experimental validation is shown in Figure 6.11, similar to the system used in our previous studies (Portillo et al., 2008b, 2009). A commercial continuous blender manufactured by GEA Pharmaceutical Systems is integrated with a twin-screw Loss-In-Weight excipient feeder provided by K-Tron and an ERIEZ vibratory Active Pharmaceutical Ingredient (API) feeder. The cylindrical blending space is 24 cm long with

inner diameter 7 cm. The shaft of the blender is attached by 24 flat triangular blades with the blade angle 37˚ forward. The blade speed and the shaft angle of the blender can be adjusted between [0,300] RPM and [-20, 20]°, respectively. The K-Tron feeder is for lactose feeding, in which feed rate and feeder hold-up are monitored. Lactose 310 provided by Foremost with the bulk density 0.66g/ml is used, and the feed rate is set to 10.23g/s. Acetaminophen pre-blended with 5% (wt) silicon dioxide is used as the API, fed at 0.31g/s. An API concentration of 3% (wt) is expected at the output of the mixer.

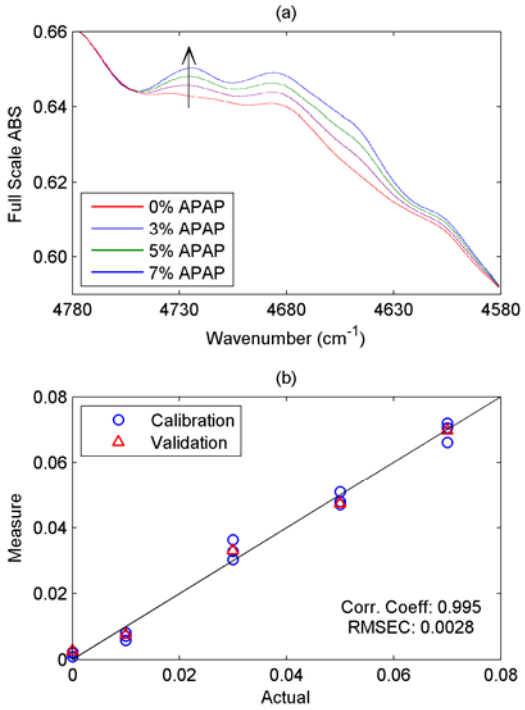

Figure 6.12 NIR spectroscopy method.

(a) Full scale calibration spectra in the range 4780 - 4580 cm^{-1}. (b) Calibration result.

Based on our previous study (Gao et al., 2011c), variance from feeder noise were significantly smaller (around ten folds) than the cross-sectional blending component, thus is not considered in the following blending performance analysis. The hold up in the

blender is calculated as the total mass in both feeders before blending begins minus the sum of the powder remaining in the feeders and at the output when steady state is reached.

For each operating condition, ten vials of output samples are collected when steady state is reached. Each vial contains approximate 1.5 cm^3 material. The API concentration in each vial is determined by using NIR spectroscopy method (Gao et al., 2011c; Vanarase et al., 2010). Lactose samples mixed with 0, 1, 3, 5, 7% (wt) pre-blended acetaminophen is prepared for calibration. A Nicolet Antaris NIR spectrometer provided by Thermo Fisher is used to acquire the absorbance spectra between the range 4000 cm^{-1} to 10000 cm^{-1} wave numbers. Each calibration sample is scanned for four times with re-shake between adjacent scans. Spectral data is collected using the software Omnic, and TQ Analyst is used to develop the calibration model. Full scale absorbance between 4780 - 4580 cm^{-1} is used for the spectral regression, and the software selects the range 4744.03 - 4705.46 cm^{-1} for the calibration model (Figure 6.12a). The root mean square error of calibration (RMSEC) is 0.0028, indicating good fitting of the spectral data (Figure 6.12b). With this NIR method, API concentration of the experimental samples can be determined, which are further applied for the RSD calculation.

6.2.4 PLS regression results

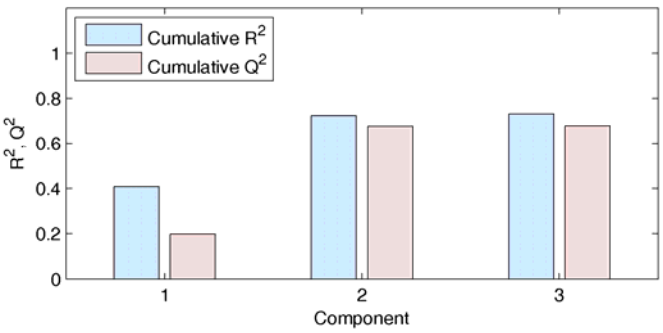

Figure 6.13 R^2 and Q^2 indices of the PLS regression from 1 to 3 principle components.

When the 64 simulations are complete, the achieved key indices k_b and v_x are normalized and used as the two-dimensional response variable matrix. PLS regression results of the 64 periodic section blending simulations are shown in Figures 6.13 -6.16. The linear model of PLS regression suggests two significant principle components (PCs) explaining 72% of the response variance (R^2=0.724, Q^2=0.678). Here

$$R^2 = 1 - \frac{RSS}{TSS}$$
$$Q^2 = 1 - \frac{PRESS}{TSS} \qquad 6\text{-}8$$

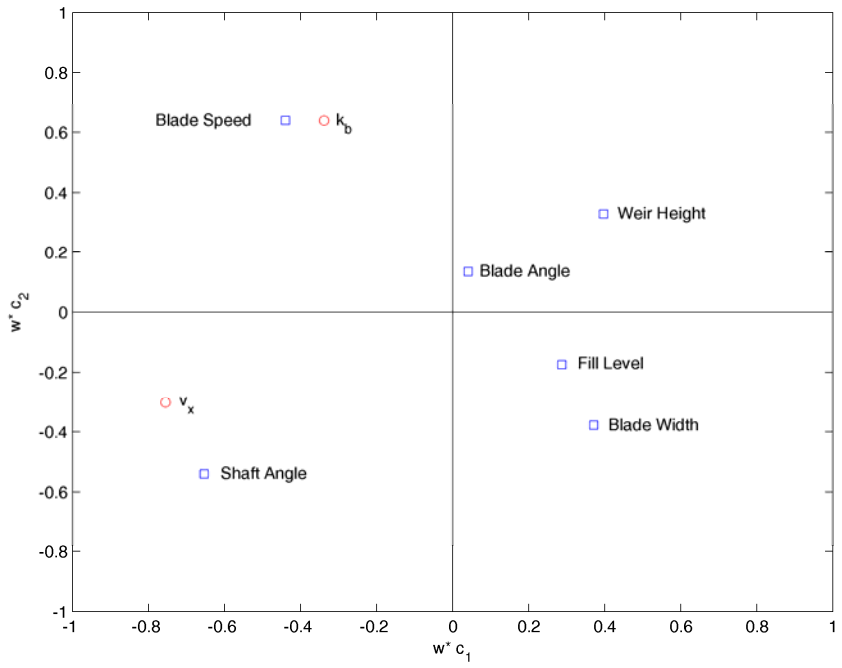

Figure 6.14 The PLS weights *w* and *c* for the two components model.

In equation (6-8) *RSS* is the residual sum square of *X* and *Y* space after the regression, *TSS* the total sum square of *X* and *Y* space, and *PRESS* the predicted residual sum square of X

and Y space by cross-validation. Therefore, R^2 represents the variability fraction of the predictor and response variables that is captured by the regression model; Q^2 is an index of the model's robustness. Since the value of Q^2 is close to R^2, the 72% variance captured in both matrices is systematic, and the model is robust to describe the structure of the design space. Both R^2 and Q^2 do not change when assuming more than two principle components, indicating that two components are enough to describe the system.

For the interpretation of the two-component PLS regression results, the standard way is to plot the loading scores w and c of one principle component against the other. It indicates how the predictor variables influence different response variables. The variables important in the i^{th} component fall far from the origin along the i^{th} axis in the w-c plot. The w-c plot is shown in Figure 6.14. The first PLS component is dominated by shaft angle and blade speed on the negative side, and weir height, blade width on the positive side. The second one is captured by blade speed and weir height on the positive side, followed by shaft angle and blade width on the negative side. The c values of the responses (k_b and v_x) are proportional to the linear variation of the response space explained by R^2. The first component describes the mean axial velocity v_x which sits far to the left in the third quadrant of the plot. For the second one, the local blending rate k_b is the main response variable, which is far upward in the second quadrant.

The significance of one predictor (operation or geometry factor) for the response is proportional to its distance form the origin in the loading score plot (Figure 6.15). Jack-knifing method is used to draw error bar of the loading score (Lopes and Menezes, 2005; Wold et al., 2001). The first principle component (PC1) indicates that the increase of shaft angle and blade speed, or the decrease of weir height can significantly enhance axial

forward flux. PC2 shows that the increase of blade speed or the decrease of shaft angle and blade width leads to more efficient local blending than adjusting other factors. These results agree well with conclusions from previous factorial analysis studies (Gao et al., 2011a; Pernenkil and Cooney, 2006).

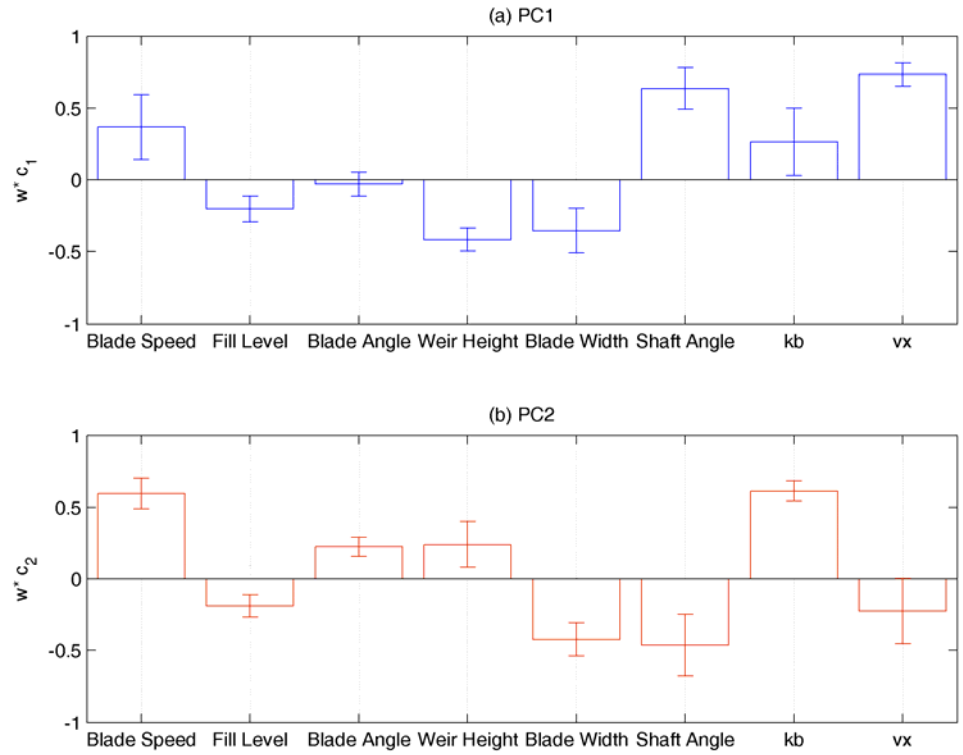

Figure 6.15 PLS regression loading scores. The bars indicate 95% confidence intervals based on jack-knifing.

A summary of the importance of the predictor variables for both the predictors and the responses is given by VIP (Variable Importance for the Projection). It is a weighted sum of square of the PLS loading scores, with the weights calculated from the response variance according to each PC:

$$VIP_{Nk} = \sqrt{\sum_{i=1}^{N} w_{ik}^2 (SSY_{i-1} - SSY_i) \frac{K}{(SSY_0 - SSY_N)}} \qquad 6\text{-}9$$

where N is the total number of principle components, and K is the total number of predictor variables. SSY_i is the sum of square of the response space after component i, and w_{ik} the loading score of variable k in the i^{th} component. This index indicates the significance of the predictors on the responses.

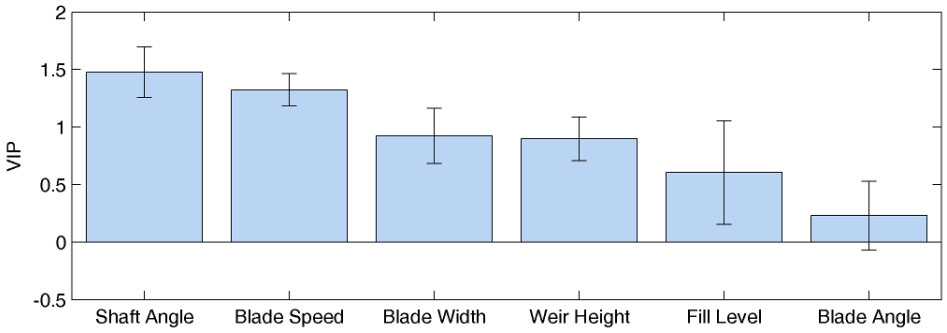

Figure 6.16 VIP of the predictor variables of the two-components PLS regression model.

The VIP plot in Figure 6.16 shows that shaft angle and blade speed are the most influential factors on blending performance in this comprehensive investigation; blade angle is the least important comparing to other factors. Based on the PLS regression results and the conclusions from previous periodic section modeling study (Gao et al., 2012), the most efficient strategy to improve blending performance is to increase blade speed and to decrease shaft angle simultaneously. In this case, hold up and mean axial velocity is kept constant, while the continuous blending rate is only proportional to the increase of blade speed. To investigate this, experimental validation is performed.

6.2.5 Experimental validation

In order to validate the improvement strategy proposed from PLS regression results, blending experiments are performed using pharmaceutical powders. Blender hold up in steady state is measured orthogonally at four blade speeds (40, 100, 180, 250RPM) and four shaft angles (0, -4, -8, -12˚). The hold up contour at these conditions is shown in Figure 8a. By following the light blue contour line in this subplot, a constant hold up of 0.32kg is retrieved through the increase of blade speed. Based on this, two sets of blending experiments are designed (Figure 6.17b). In the original set, blender is kept horizontal while blade speed increases from 40, 80, 120, to 160RPM. In the improved set, the shaft angle is set as 0, -3.77, -6.99, and -11.31˚ for the corresponding blade speed 40, 80, 120, 160RPM, respectively, in order to keep a constant hold up at 0.32kg.

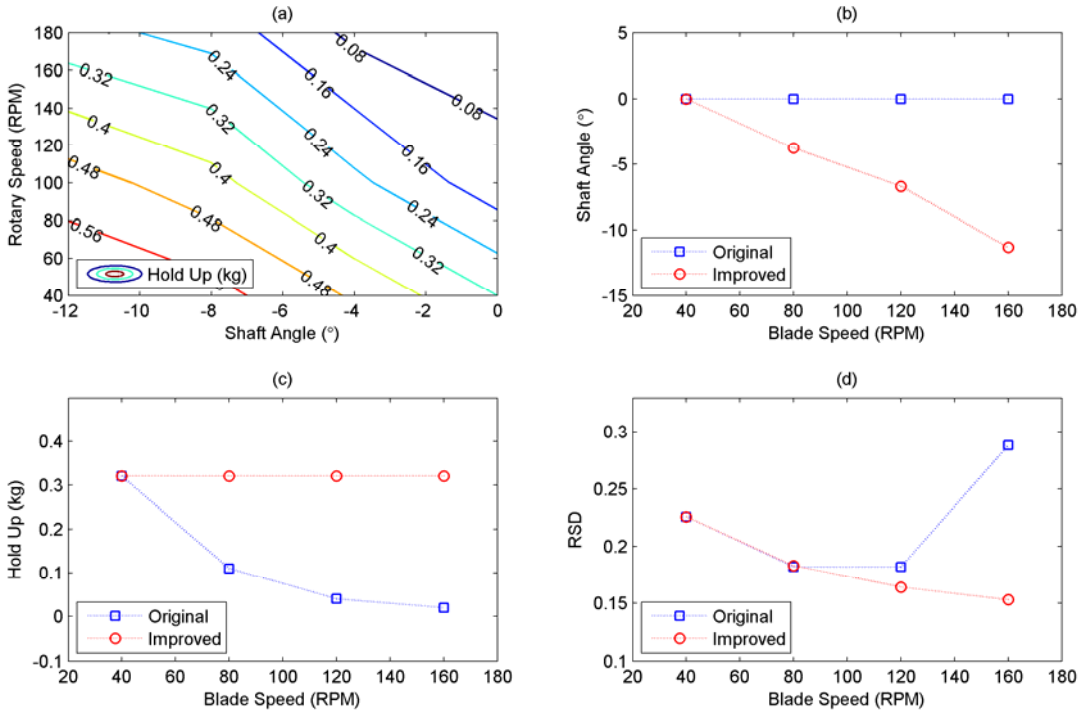

Figure 6.17 Summary of the experimental results.

(a) Hold-up contour in the blender. (b) Design of performance improvement. (c) Hold-up of original and improved sets. (d) Blending performance of original and improved sets.

Blending performance of both experimental sets are measured and compared to show the efficiency of the proposed strategy. As Figure 6.17c shows, hold up of the original set decreases along the ascending blade speed, which leads to shorter residence time and thus worse blending performance at large blade speed (Figure 6.17d). A similar profile has been reported in our previous study (Vanarase and Muzzio, 2011). On the other hand, significant performance improvement is observed at high blade speed in the improved set due to a constant mean residence time. In this case, the number of blade passes that powder experiences is simply proportional to the ascending blade speed. As expected, the RSD decay curve is similar to batch systems, showing exponential decay profile against the blade speed.

6.3 Summary

This chapter investigates the effect of operating conditions on two important parameters of continuous blending: local mixing rate k_b and axial velocity v_x of powders. Factorial analysis shows that, at high rotary speed and low fill level, particles move faster and reside for a shorter time inside the mixer. Faster local mixing is observed in the same range of operations. This competition between k_b and v_x leads to a trade-off on the overall continuous blending performance even under the best operating conditions. Moreover, the same optimal operating conditions are observed for different mixing cases, indicating that these optimal conditions might be universal and could be applied in other cases using the same mixer. The Projection to Latent Structure (PLS) regression analysis is further introduced to clarify the complicate influence of various operation and geometry factors on blending performance. Regression results show that shaft angle and blade speed are the

most influential factors. Blade geometry and fill level show less impact in the investigated range of factors. Based on these results, novel strategies are proposed as follows to improve continuous blending performance. The key is to keep axial velocity constant when increasing the blade speed. This guarantees the variance decay rate along the mixing axis is proportional to the blade speed in continuous blending systems. To achieve this goal, blade angle or weir height was altered along with the ascending blade speed in the factorial analysis. Based on conclusions from the PLS regression, simultaneously changing shaft angle and blade speed, which conveniently increases blending rate while keeps axial velocity constant, is the most efficient strategy suggested for performance improvement. Significant improvements on blending performance were observed in both simulations and experimental validations using pharmaceutical powder. In sum, this work clarifies the significance of various operation and geometry factors in the performance improvement of continuous powder blending unit operation, and provides an efficient guidance on blender design and operation control in practice.

Once more, it should be emphasized that all simulation cases in this chapter are non-segregating. For segregating powders, the optimal operation does not only depend on how fast mixing reaches steady state, but also on whether the steady state mixture can be characterized as “well mixed”. Therefore, before designing continuous mixing system for specific segregating case, batch mixing using a geometry and operation similar to one periodic section of the corresponding continuous blender is recommended (Gao et al., 2011a). If segregation is observed and leads to failure of mixing in the preliminary batch case, it needs to be handled by altering operating conditions before the corresponding continuous process is applied. As a result, previous studies on batch segregation such as

Moakher et al. (2000) and Alexander et al. (2004) can facilitate this study, and should be considered in further investigations on continuous blending of segregating materials.

Chapter 7

Scale-up of continuous powder blending

In this chapter, the theoretical basis of scaling up continuous powder blending is established. Firstly, variance spectrum analysis is introduced to illustrate the influence of sampling size on the relationship between flow pattern similarity and mixing performance similarity, which provides a theoretical means to analyze the scale-up of batch mixing processes and the scale-up of the cross-sectional mixing in continuous mixing processes. Secondly, the periodic section modeling proposed in the previous chapter (Gao et al., 2012) is applied to characterize the cross-sectional blending component, which is considered as the combination of a batch-like blending process and the axial motion of the powder along the continuous mixer. The rest of the chapter is organized as follows. Current limitations on scale-up is discussed in Section 7.1. In Sections 7.2 and 7.3, the variance spectrum,and the simulation designs are introduced. Two methodologies to determine the variance spectrum, the Fourier series and the Lomb Scargle Periodogram, are described. Conceptual simulations with typical mixing cases of non-segregating and cohesive segregating particles are then performed in Section 7.4 to show the applicability of the developed scale-up strategy, followed by the conclusion in Section 7.5.

7.1 Current limitations

Previous work in the area of powder blending scale-up is based on the principle of similarity proposed by Johnstone and Thring (1957). According to this principle, the material flow patterns in two scales of mixing apparatuses are expected to be similar when the dimensions, velocity fields, and force distributions of corresponding points are

proportional to each other. Generally, dimensional analysis is applied to identify these similarity criteria if the process governing equations are unknown, while dimensionless forms are derived if the governing equations are available. Applying this principle, Wang and Fan (1974) investigated the scaling up of tumbling mixers. Their results indicate that the ratio of centrifugal force to the gravitational force, or the Froude number, can be used as the main similarity criterion for the scale-up of a tumbling mixer. Based on hydrodynamic similarity, Horio et al. (1986) developed a scale-up rule for fluidized beds when the similarities in bubble coalescence, bubble splitting, and interstitial flow pattern are satisfied. Surface velocity profiles in rotating cylinders were found to follow simple scaling rules through the normalization of a one-dimensional motion equation with constant acceleration (Alexander and Muzzio, 2005; Alexander et al., 2002).

Of the few studies concerning the scaling up of continuous powder mixing processes, most efforts are spent on the characterization of the axial mixing component, namely, scaling up of the RTD (residence time distribution). Based on dimensional analysis similar to the one used in batch mode studies, Abouzeid *et al.* (1980) applied the *characteristic time* (the ratio of dimensionless hold up and feed rate) as the main scale-up criterion for the RTD of materials flowing in rotating drums. The dimensionless variance of the RTD, which is defined as the second moment of the RTD function (Nauman, 2008), was approximately calculated as a function of Peclet number using the Fokker-Planck dispersion model (Risken, 1996). Similar analysis was performed in the polymer processing of a continuous twin-screw extruder (Meijer and Elemans, 1988), on which the scale-up issues of geometry, heat transfer, and power consumption were discussed. A more complex scaling relationship for rotating drums was developed for particles without considering cohesion

and only for cases where the effect of interstitial fluid is negligible (Ding et al., 2001). In this study, parameters and variables were normalized using governing equations based on the Eulerian approach, which assumes that the properties of the granular materials are a continuous function of position (Johnson and Jackson, 1987; Savage and Hutter, 1989).

Despite the achievements described above, there are still two unresolved issues for developing a quantitative scale-up strategy for continuous powder mixing processes. Firstly, although it is generally believed that similar mixing performances can be achieved in geometries of different scales when the principle of similarity is satisfied, theoretical validation is not available yet. There is no doubt that we can get similar mixing when the scale of mixing measurement, or the sampling size, is proportional to the scale of mixer geometry. However, the key difficulty is that in most cases the sampling size applied for mixing of different geometry scales is constant, as the size of samples is predetermined by the size of the tablets, which is the final product of pharmaceutical manufacturing process. This constant-sample effect on measuring the mixing performance is rarely considered in previous scale-up studies. Secondly, few investigations focus on continuous powder mixing compared to the well-studied batch mixing process. While it is well-known that the continuous powder mixing process is a combination of axial and cross-sectional mixing (Williams, 1976), quantitative modeling for both mixing components, especially for the cross-sectional mixing, has not been well established. Thus, development of quantitative scale-up strategies is difficult for the same process. We will discuss these issues in detail in this chapter.

7.2 Variance spectrum analysis

7.2.1 Fourier analysis

Variance spectrum is defined as the distribution of variance components in different frequency domains, which can be obtained through the application of Fourier transform. Shin and Fan (1978) used the application of discrete Fourier transform (DFT) to investigate the characterization of random and ordered powder mixtures. While the amplitude of the spectrum indicates the intensity of segregation at different frequency domains, the location of the maximum spectrum component illustrates the scale of segregation intuitively (Poux et al., 1991; Weineköter and Reh, 1995).

One-dimensional discrete Fourier series method has been discussed in Chapter 2. The corresponding variance value $\sigma^2(f_s)$ is calculated as the integration of the spectrum from zero to half of the sampling frequency:

$$\sigma^2(f_s) = \frac{1}{2}\int_0^{f_s/2} s(f)^2 df \qquad 7\text{-}1$$

The variance spectrum is only determined by the structure of the mixture, while the measured value of variance depends on the sampling frequency. Therefore, it can be expected that: (i) mixtures with similar structures but different scales will share similar variance spectra; (ii) mixing processes of different scales will share similar amounts of decay within the variance spectra when the principle of similarity is satisfied; and (iii) before the interaction of sampling frequency and variance spectrum decay is clarified, we cannot claim that similar flow patterns always lead to similar variance decay when a constant sampling size is used. Thus, the constant-sample effect of scaling up needs further investigation.

By using the one-dimensional discrete Fourier transform (1D-DFT), Shin and Fan (1978) theoretically confirmed the linear relationship between the decay of the spectrum and the variance for mixing processes obeying the Fickian diffusion equation. However, this

1D-DFT is not applicable in the study of practical powder mixing processes due to the following reasons. First, almost all industrial processes of powder mixing are three-dimensional, which cannot be characterized by one-dimensional Fourier analysis. Secondly, the definition of Fourier analysis requires evenly distributed samples with equal sampling sizes in a cube-shape space. This is usually not satisfied in practice, since most powder mixing spaces are not cube-shaped, and the rotating motions of blades (convective mixers) or mixing apparatuses (tumbling mixers) hinders the formation of evenly distributed samples through mixing processes.

To overcome the first problem, the three-dimensional discrete Fourier transform (3D-DFT) is introduced (Averbuch and Shkolnisky, 2003):

$$X_{h,j,k} = a_{h,j,k} + ib_{h,j,k} = \frac{2}{N^3}\sum_{l=0}^{N-1}\sum_{m=0}^{N-1}\sum_{n=0}^{N-1} x_{l,m,n} e^{-\frac{2\pi i}{N}(hl+jm+kn)} \qquad 7\text{-}2$$

$$s(\mathbf{f})^2 = s(f_1, f_2, f_3)^2 = s(h\Delta f, j\Delta f, k\Delta f)^2 = \frac{\left|X_{h,j,k}\right|^2}{\Delta f^3} \qquad 7\text{-}3$$

where l, m, n are the index of evenly sampled points within the three dimensions of the space domain, and h, j, k are the index of frequency components in the corresponding dimensions of the spatial-frequency domain. The overall variance measured at the sampling frequency f_s^3 (the corresponding sampling size is $1/f_s^3$ in unit of volume) can be expressed as

$$\sigma^2(f_s^3) = \frac{1}{2}\iiint_{f_1+f_2+f_3 \le \frac{3}{2}f_s} s(\mathbf{f})^2 df_1 df_2 df_3 \qquad 7\text{-}4$$

where $f_1, f_2, f_3 \in [0, N\Delta f]$, and the limit $3f_s/2$ is applied to eliminate the effect of aliasing (Gao et al., 2012). As indicated in equations (7-4), the 3D variance spectrum $s(\mathbf{f})^2$ itself is

a three-dimensional function. This makes it difficult to visualize the four-dimensional profile $s(\mathbf{f},t)^2$ in the mixing process when we try to capture the spectrum decay as a function of time. Therefore, it is necessary to convert the 3D variance spectrum to a 1D spectrum by averaging the spectrum components with the same magnitude of frequency. In this work, the variance spectrum values $s(\mathbf{f})^2$ following equation (7-5) are considered to share the same magnitude of frequency f:

$$f_1 + f_2 + f_3 = 3f \tag{7-5}$$

The conversion of the variance spectrum is then expressed as follows:

$$s(f)^2 = \frac{\iint_{f_1+f_2+f_3=3f} s(\mathbf{f})^2 \, dS}{\iint_{f_1+f_2+f_3=3f} dS} = \frac{1}{w(f)} \iint_{f_1+f_2+f_3=3f} s(\mathbf{f})^2 \, dS \tag{7-6}$$

$$\sigma^2(f_s^3) = \frac{1}{2}\int_0^{f_s/2} s(f)^2 w(f) df \tag{7-7}$$

where $w(f)$ is the weight of the averaged 1D variance spectrum $s(f)^2$; dS indicates the infinitesimal area on the plane indicated by equation (7-5) in the averaging process. By using equation (7-6), the variance spectrum decay $s(f,t)^2$ can be visualized in a contour plot. The second issue regarding the application of a Fourier transform is that the particles are not evenly distributed. To overcome this problem, the Lomb-Scargle Periodogram is introduced in the following subsection.

7.2.2 Lomb-Scargle Periodogram (LSP)

To characterize stellar cycles where the observation points are usually unevenly spaced, Lomb-Scargle Periodogram was first proposed in the analysis of astronomical data in order to detect periodic signals hidden in noise (Gilliland and Baliunas, 1987). The Lomb-Scargle Periodogram is equivalent to a linear least-square fit of sine and cosine

functions to the observed signal series, which is an alternative to the Fourier series in estimating the profile of variance spectra (Babu and Stoica, 2010). For one-dimensional unevenly sampled data (t_n x_n), where tn indicates the location of sample x_n, its linear least-square fit of sine and cosine functions can be expressed as follows:

$$x_f(t) = a\cos\omega t + b\sin\omega t = \begin{bmatrix}\cos\omega t & \sin\omega t\end{bmatrix}\begin{bmatrix}a\\ b\end{bmatrix} \quad 7\text{-}8$$

$$E(\omega) = \sum_{n=1}^{N}[x_n - x_f(t_n)]^2 \quad 7\text{-}9$$

Notice that x_n is also with mean of zero. To determine the value of $E(\omega)_{min}$ for the best fitting result, the following relationship should hold:

$$\frac{\partial E}{\partial a} = \frac{\partial E}{\partial b} = 0 \quad 7\text{-}10$$

and the difference of the least square fitting is calculated as follows:

$$\Delta E(\omega) = \sum_{n=1}^{N}[X(t_n)]^2 - E_{\min}(\omega) \quad 7\text{-}11$$

Note that $\Delta E(\omega)/N$ represents the variance component measured at frequency ω. Based on Lomb and Scargle's derivation (Lomb, 1976; Scargle, 1982), an estimation of the variance spectrum $s(f)^2$ can be expressed as follows:

$$s(f)^2 = \frac{2}{\Omega\Delta f}\left[\frac{\left(\sum_{n=1}^{N} x_n\cos\omega(t_n-\tau)\right)^2}{\sum_{n=1}^{N}\cos^2\omega(t_n-\tau)} + \frac{\left(\sum_{n=1}^{N} x_n\sin\omega(t_n-\tau)\right)^2}{\sum_{n=1}^{N}\sin^2\omega(t_n-\tau)}\right] \quad 7\text{-}12$$

$$\tau = \frac{1}{2\omega}\tan^{-1}\left[\frac{\sum_{n=1}^{N}\sin 2\omega t_n}{\sum_{n=1}^{N}\cos 2\omega t_n}\right] \quad 7\text{-}13$$

where $\omega=2\pi f$ is the angular frequency, and Ω represents the dimension of the variance spectrum analysis (Hocke and Kämpfer, 2009). τ is a redundant parameter to simplify the formula of the solution. The value of τ is chosen so that

$$\sum_{n=1}^{N}\cos\omega(t_n-\tau)\sin\omega(t_n-\tau)=0 \qquad 7\text{-}14$$

Equations (7-8) -(7-14) represents the generation of original formula of the Lomb-Scargle Periodogram which is widely used in astronomical research. To apply this concept for the analysis of powder mixing, two aspects of the mathematical formula should be modified to account for a three-dimensional problem structure and an uneven sampling size distribution. To achieve the first modification, all the scalar product ωtn in previous equations are replaced by a dot product of two vectors $\boldsymbol{\omega}\cdot\mathbf{t_n}$, where $\boldsymbol{\omega}=2\pi\mathbf{f}$ (ω_1, ω_2, ω_3) is the angular form of the three-dimensional spatial frequency, and $\mathbf{t_n}$ (t_{n1}, t_{n2}, t_{n3}) is the three-dimensional location of the nth sample unevenly taken in the three-dimensional mixture. The modified equations (7-15) and (7-16) for three-dimensional analysis are then expressed as follows:

$$s(\mathbf{f})^2=\frac{2}{\Omega^3\Delta f^3}\left[\frac{\left(\sum_{n=1}^{N}x_n\cos(\boldsymbol{\omega}\cdot\mathbf{t_n}-\theta)\right)^2}{\sum_{n=1}^{N}\cos^2(\boldsymbol{\omega}\cdot\mathbf{t_n}-\theta)}+\frac{\left(\sum_{n=1}^{N}x_n\sin(\boldsymbol{\omega}\cdot\mathbf{t_n}-\theta)\right)^2}{\sum_{n=1}^{N}\sin^2(\boldsymbol{\omega}\cdot\mathbf{t_n}-\theta)}\right] \qquad 7\text{-}15$$

$$\theta=\frac{1}{2}\tan^{-1}\left[\frac{\sum_{n=1}^{N}\sin 2\boldsymbol{\omega}\cdot\mathbf{t_n}}{\sum_{n=1}^{N}\cos 2\boldsymbol{\omega}\cdot\mathbf{t_n}}\right] \qquad 7\text{-}16$$

To achieve the second modification, the generalized Lomb-Scargle Periodogram (LSP) (Zechmeister and Kürster, 2009) is applied in this chapter, which introduces the weight of

samples in the calculation of variance spectrum. Equation (7-9) is thus modified as follows:

$$E(\omega) = \sum_{n=1}^{N} w_n [x_n - x_f(t_n)]^2 \qquad 7\text{-}17$$

where w_n represents the weight of the nth sample of the three-dimensional mixture. When unevensampling size distribution is present, which is the case in powder mixing, samples with different sampling sizes are assigned different weights. For the samples with the desired sampling size, we set w_n=1; for the samples with sampling size far away from the desired sampling size, we set w_n=0. A simple linear weight distribution is used in this study. The sample weight increases in a manner proportional to the sampling size until the desired sampling size is reached, and then decreases in a similar manner. By introducing the sample weight, the 3D formula of LSP are now expressed as follows:

$$s(\mathbf{f})^2 = \frac{2}{\Omega^3 \Delta f^3} \left[\frac{\left(\sum_{n=1}^{N} x_n w_n \cos(\boldsymbol{\omega} \cdot \mathbf{t_n} - \theta) \right)^2}{\sum_{n=1}^{N} w_n \cos^2(\boldsymbol{\omega} \cdot \mathbf{t_n} - \theta)} + \frac{\left(\sum_{n=1}^{N} x_n w_n \sin(\boldsymbol{\omega} \cdot \mathbf{t_n} - \theta) \right)^2}{\sum_{n=1}^{N} w_n \sin^2(\boldsymbol{\omega} \cdot \mathbf{t_n} - \theta)} \right] \qquad 7\text{-}18$$

$$\theta = \frac{1}{2} \tan^{-1} \left[\frac{\sum_{n=1}^{N} w_n \sin 2\boldsymbol{\omega} \cdot \mathbf{t_n}}{\sum_{n=1}^{N} w_n \cos 2\boldsymbol{\omega} \cdot \mathbf{t_n}} \right] \qquad 7\text{-}19$$

which are the final formulas of LSP that are ready for characterizing the variance spectrum decay in powder mixing processes. Ω^3 represents the dimension of the 3D variance spectrum, and Δf the minimum detectable frequency under the current uneven sampling condition.

As mentioned before, the method of Lomb-Scargle Periodogram is an estimation of the variance spectrum for the case where the standard Fourier analysis cannot be applied. When fewer samples are retrieved, less information is available in the investigation of the mixture structure, which leads to large deviation between the LSP and the real spectrum. Previous studies on astronomical fields have investigated the statistical significance of the spectrum obtained through the LSP method (Foster, 1995; Roberts, 1987; Stoica et al., 2009). However, these works are mainly focused on the ability of the method in detecting solar cycles, namely, how to distinguish single spectrum peaks from the original intensity measurement with a noisy background. As the variance components in most of the frequency domains are considered as white noise and are useless information, their role as the spectrum distribution of variance is seldom referred. As a result, we only summarize a few qualitative conclusions from these works that are useful for our study:

(i) When the mixture is ideally random, the variance spectrum of the mixture is the same everywhere for both the DFT and the LSP method. In this case, the corresponding variance measurement is proportional to the integration interval from zero to half of the sampling frequency, thus being anti-proportional to the sampling size.

(ii) When the concentration in the mixture has a sinusoidal distribution, the variance spectrum derived through DFT shows a sharp peak at the frequency of the sinusoid curve, while its LSP estimation is a smear of the peak at the same frequency. The fewer samples that are used in the LSP method, the more smears the peak looks like.

Examples of these characteristics of the LSP method are discussed within the results in later sections.

7.3 Methodology

Periodic section modeling is used in the study of scaling up continuous mixing processes. The Discrete Element Method (DEM) is applied as the simulation environment for examining the scaling up issue. In order to investigate the effects of different mixing behaviors on the scale-up of continuous blending process, three kinds of particles with the same diameters and densities were used in the simulations (Table 7.1). In the present study, we investigate two case studies: in the first one a mixture consisting of only particles type 1 having different colors is considered whereas in the second case a mixture of particles type 2 and 3 are considered. The first case is representative of a non-segregating mixture, while in the second case the two types of cohesive particles (types 2 and 3) will tend to agglomerate with only the same type of particles, which results in segregation.

Table 7.1 Physical and numerical parameters used in the DEM model.

Parameter	Value		
	Particle 1	Particle 2	Particle 3
Cohesiveness	No-Cohesive $k_1 = 0 J \cdot m^{-3}$	Self-cohesive with $k_2 = 8 \times 10^5 J \cdot m^{-3}$	Self-cohesive with $k_3 = 8 \times 10^5 J \cdot m^{-3}$

The simulation design is shown in Figure 7.1. Two periodic sections with geometries that are similar in shape and scale are constructed within the DEM environment, while the 120mm-scale section has a size that is 1.5 fold larger than the 80mm-scale one in all dimensions. Two fill levels (25%, 50%) were investigated for both geometries. In order to understand the influence of the initial scale of segregation on the scaling up issue, two loading patterns, the half loading and the quarter loading were tested. An overall 50:50 volumetric ratio of particles was loaded for all the simulations (Table 7.2). The empirical

principle of similarity was also considered, which requires a constant Froude number for the mixing of different scales. Based on the expression of Froude number $Fr=\omega^2 r/g$, where ω is the angular velocity of blade rotation, r the radius of blade and g the gravity, 220 RPM is set as the blade speed for all the 80 mm scale mixing cases, while 180 RPM is set for all the 120 mm scale simulations. This leads to a constant Froude number value of 4.35 in both mixing scales.

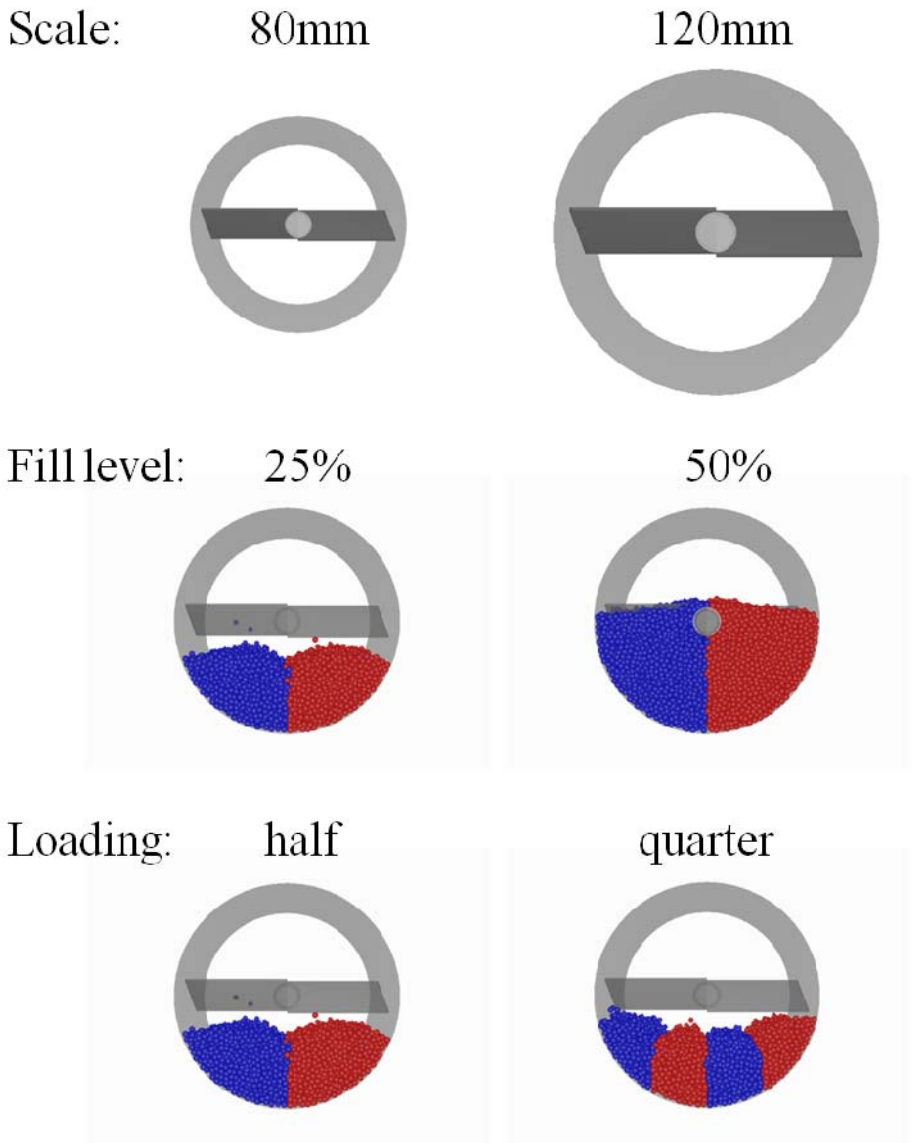

Figure 7.1 Illustration of simulation designs.

Table 7.2 The number of initial loading particles for both mixing cases.

Particle number / Fill level	80 mm scale		120 mm scale	
	Blue (Type 1 or 2)	Red (Type 1 or 3)	Blue (Type 1 or 2)	Red (Type 1 or 3)
25%	1120	1120	3780	3780
50%	2240	2240	7560	7560

The variance spectrum of mixing in the studied periodic sections was calculated as follows. Cubes were divided with a side length of 8 or 12 mm for the mixing cases of 80 mm and 120 mm scales respectively, which leads to a sampling matrix of 5×10×10 for the mixing on both scales. For each time point, all the cubes with at least one particle are count as samples, and the corresponding location t_n, zero-centered concentration x_n are recorded and calculated in sequence. The reciprocal of the mixing scale $\Delta f=1/scale$, the maximum detectable frequency $\Omega\Delta f$, and the weight of sample w_n, which is the ratio of the current sampling size and the maximum number of particles randomly packed in the same cube space, are also calculated. The four-dimensional variance spectra decay $s(\mathbf{f}, t)^2$ as a function of time can be calculated on the interval $[0, \Omega\Delta f]$ for all three dimensions, where Δf is set as the resolution in the frequency domain for this LSP calculation. The 1D formula $s(f, t)^2$ of the 3D-LSP profile is then derived, which is shown in the results section.

To determine the time-dependent batch-like mixing in the periodic section, samples are retrieved inside the mixing space. The mixing space is divided into cubes with the side length of 10 mm, and all the samples in a time interval of 0.1 sec of the simulation process were considered as samples of the same time point. In order to gather enough samples (more than 80) for each time point, samples with 21 particles were selected corresponding to the number of particles that can be randomly packed within the sampling size of 0.45 cm^3. Notice that this sampling size is comparatively smaller than in practice. Based on the

expression of variance σ^2, the relative standard deviation (RSD) of blue particles of each time point can be calculated. The method of determining the residence time distribution (RTD) can be found in previous chapter.

7.4 Scale-up of continuous blending components

7.4.1 Cross-sectional blending

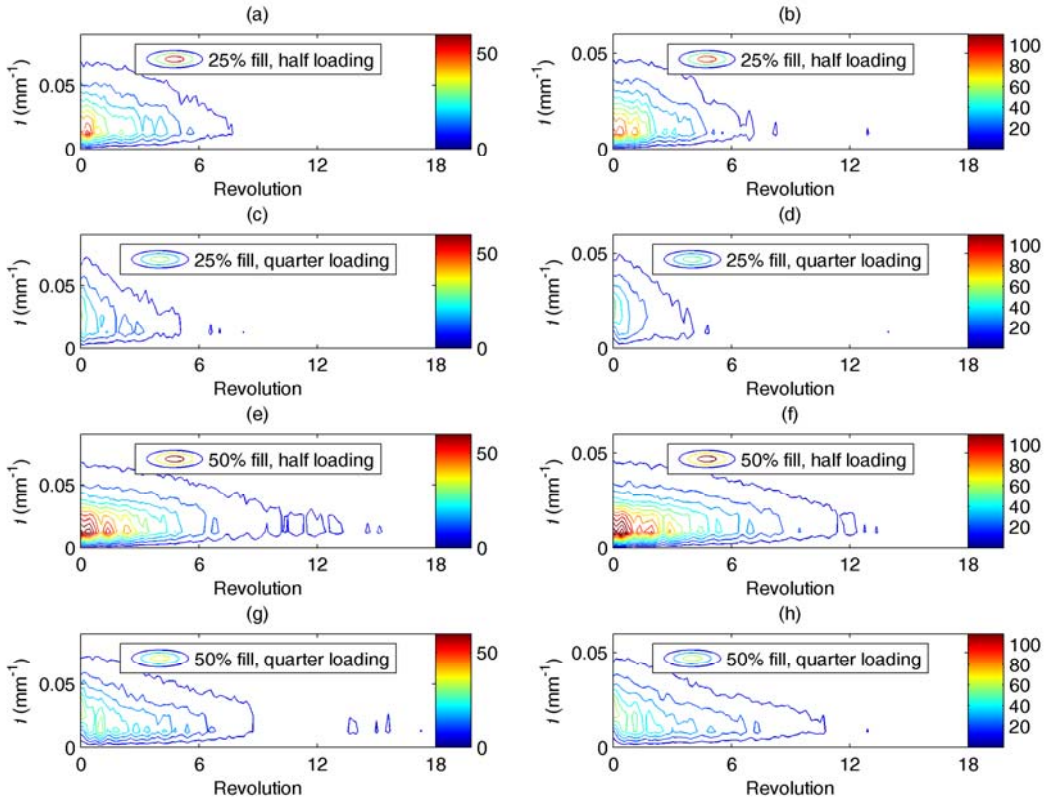

Figure 7.2 Variance spectrum decay contours of non-segregating mixing cases.

The left four plots (a, c, e, g) show the 80 mm scale mixing cases. The right four plots (b, d, f, h) show the 120 mm scale mixing cases.

Figure 7.2 refers to the overall variance spectrum decay contours of non-segregating mixing cases. The left four graphs show the spectrum decay of the 80 mm scale cases,

while the right four show the 120 mm scale cases. The maximum detectable frequency $\Omega\Delta f$ of the 80 mm and 120 mm scales are 0.125 mm^{-1} and 0.083 mm^{-1}, respectively. The limits of the vertical axes are then selected as [0, 0.09] mm^{-1} and [0, 0.06] mm^{-1} in order to cover the main decay characteristics of the two scales. Notice, that a constant Froude number is used, which indicates different blade speeds between the two mixing scales. For comparison purposes, the mixing processes are measured using revolution of blade rotation instead of time.

An accurate ratio of spectrum amplitude can be expected between the two scales. Since mixing on both scales share the same initial variance and similar initial variance spectra, we can claim the following equation:

$$\frac{s_1(f_1)^2}{s_2(f_2)^2} = \frac{scale_1^3}{scale_2^3} \qquad 7\text{-}20$$

where $f_1 / f_2 = scale_2 / scale_1$. Based on this formula, the color maps of the contours in Figure 7.2 are set with a ratio of $(120/80)^{3/2}$ =1.84 for the two scales, namely, the color map interval [0, 60] for the 80 mm scale and the interval [0, 110] for the 120 mm scale. A level step of 6 or 11 is applied for the corresponding color map so that the spectra with different amplitudes can be visually compared.

In order to identify mixing similarity of the two scales, the left four plots in Figure 7.2 are compared with the right four plots. Although the initial amplitudes are different, the variance spectrum decay processes of the two scales are similar for all fill levels and initial loadings. Therefore, we can state that similar flow patterns due to a satisfied principle of similarity lead to similar decay processes of variance spectra for the non-segregating mixing cases. To further illustrate this observation, we plot the initial spectrum profile (at the beginning of the first revolution) and the steady state spectrum (at the end of 18

revolutions) in Figure 7.3. The vertical and horizontal axis ratios are the same as in Figure 7.2. As shown in the plots, the initial variance spectra are very similar for mixing on different scales. When a steady state is reached, the same horizontal spectra, representing ideal random mixtures, is obtained for all plots (dot lines, Figure 7.3).

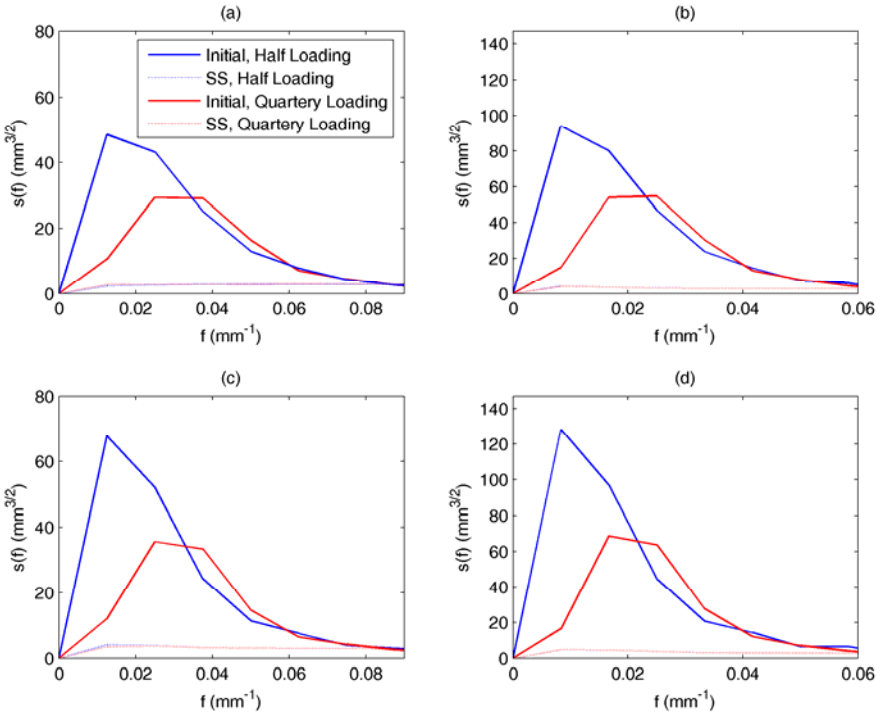

Figure 7.3 The initial and steady state profiles of variance spectrum of the non-segregating mixing cases.

(a) 80 mm scale at 25% fill. (b) 120 mm scale at 25% fill. (c) 80 mm scale at 50% fill. (b) 120 mm scale at 50% fill. Half: half loading. Quarter: quarter loading. rev: revolution.

Figures 7.2 and 7.3 also show the effect of loading pattern and fill level on the initial variance spectrum. A lower peak for the initial spectrum is found in the quarter loading than the half loading patterns, while the frequency of the peak in the quarter loading is

twice that of the half loading. This is due to that the weight *w(f)* of the 1D converted variance spectrum *s(f)* increases with the magnitude of frequency. While a constant overall variance is kept for different loadings, a smaller peak is expected when it is in a higher frequency domain. When comparing different fill levels, fewer smears occur in the spectra with higher fill levels, due to more samples being obtained in that condition. This observation corresponds with qualitative conclusion (iii) in the previous section.

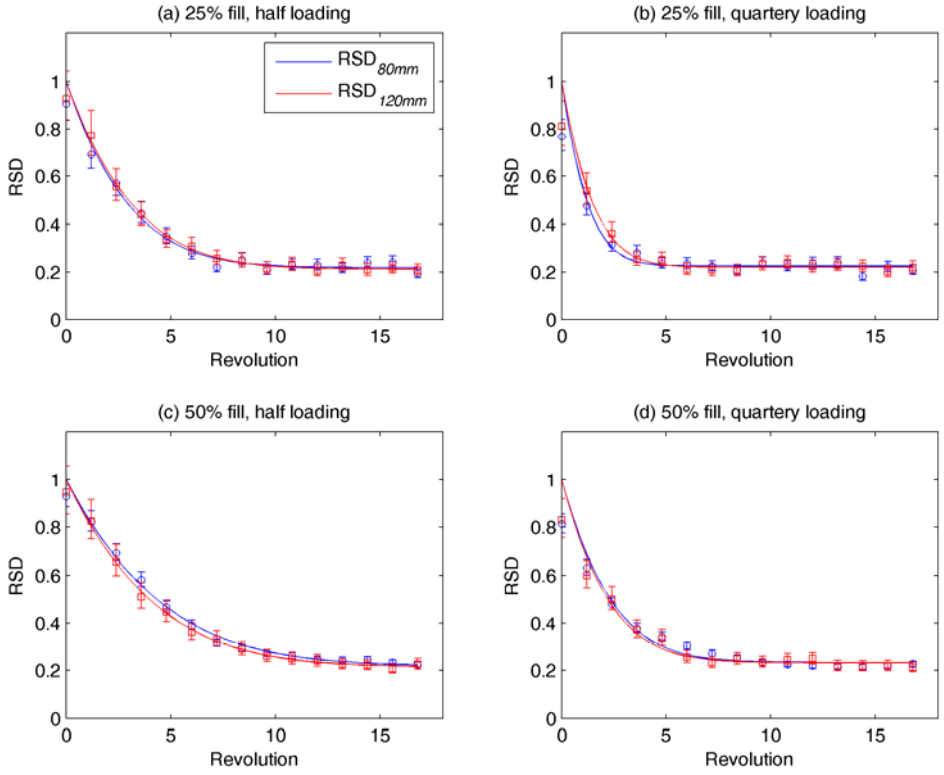

Figure 7.4 RSD-t decay curves measure at sampling size of 0.45 cm^3, non-segregating mixing cases.

(a) 25% fill, half loading. (b) 50% fill, quarter loading. (c) 50% fill, half loading. (d) 50% fill, quarter loading.

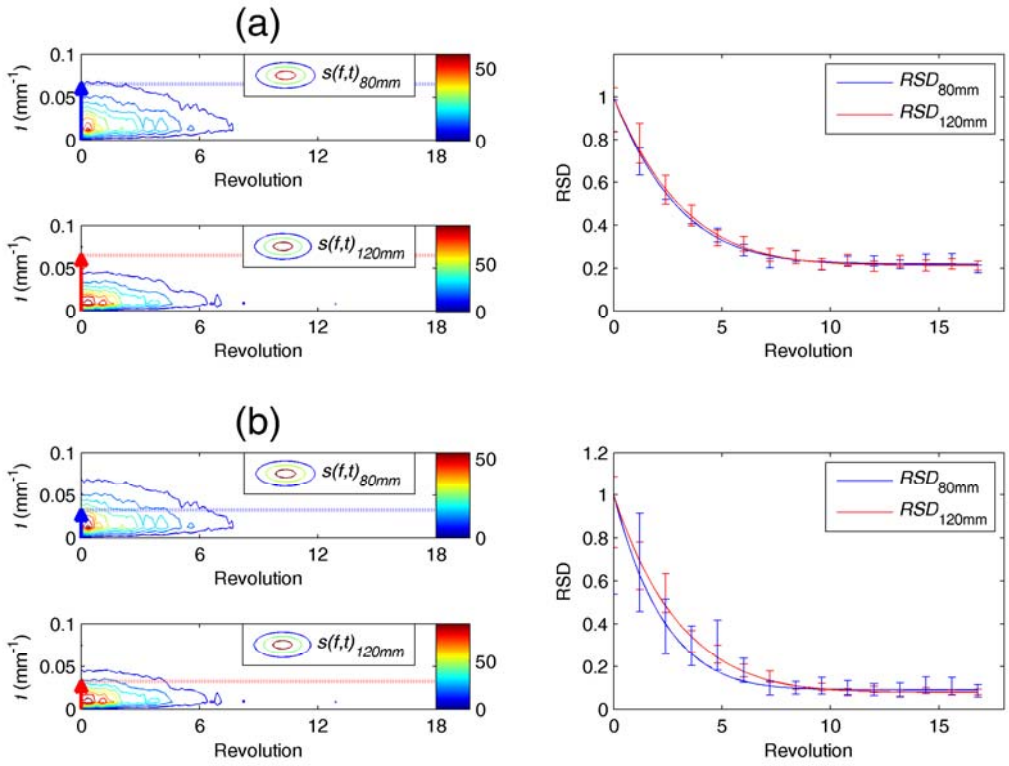

Figure 7.5 Illustration of the constant-sample effect on the scaling up of powder mixing. (a) Sampling size of 0.45 cm^3. (b) Sampling size of 3.6 cm^3. Different integration coverage on the main spectrum decay components produces different RSD-t curves in the case of 3.6 cm^3 sampling size.

An interesting phenomenon is observed in Figure 7.2 when comparing the spectrum decays for different loading patterns. For the half loading cases, the decay of the spectrum peak is always at the lowest detectable frequency $f=\Delta f$, which indicates a decreasing intensity of segregation with the scale of segregation unchanged. However, when the loading is the quarter pattern, the spectrum peak decays as well as shifts from the second lowest frequency domain $f=2\Delta f$ to the lowest one. Therefore, it can be expected that no matter

how the initial variance spectrum appears, the scale of segregation always tends to approach the scale of the overall mixing space in the process of mixing. Due to a similar mechanism of mixing, the same phenomenon is also expected in tumbling and many other mixing processes.

The RSD-t curves measured at the sampling size 0.45 cm3 are plotted in Figure 7.4. Based on the number of particles in each sample, the steady state RSD value of the mixing process can be calculated using the binominal theorem (Brone et al., 1998). Specifically, the steady state RSD is approximately 0.22 for the sampling size of 0.45 cm3 (21 particles per sample). As shown in the plots, mixing is significantly faster in the quarter loading pattern, while it is slightly slower when the fill level is increased. However, the RSD decay curves almost overlap with each other for the two scales of mixing for all conditions, which illustrates good scaling characteristics on mixing performance under current sampling size.

To clarify the constant-sample effect we described in the introduction, the effect of spectrum integration interval on the corresponding RSD decay curve is investigated. The half-loading mixing at 25% fill level (Figure 7.2a, b) is applied for this illustration. To study the constant-sample effect, the same limits of vertical axis of frequency are plotted for both scales ([0, 0.1]). The RSD decay curves measured at a larger sampling size (3.6 cm3) is also involved besides the 0.45 cm^3 cases. The results are shown in Figure 7.5. When the sample size of 0.45 cm^3 is applied, the integration interval of $s(f,t)$ in the variance calculation is [0, 0.065] mm^{-1}. This interval covers all the spectrum decay components for the mixing of both scales (Figure 7.5a). As a result, well fitted RSD decay curves are observed. In contrast, the integration interval in the variance calculation is [0, 0.032] mm^{-1} for the case of 3.6 cm^3 sampling size. In this case, the integration interval covers almost all

the main decay components for the 120 mm scale mixing, while some components in higher frequency domains are missed in the case of the 80 mm scale. This leads to different fitted RSD decay curves (Figure 7.5b). Therefore, with the principle of similarity satisfied, similar mixing performance can be achieved only when the sampling size is much smaller than the scale of both mixing geometries.

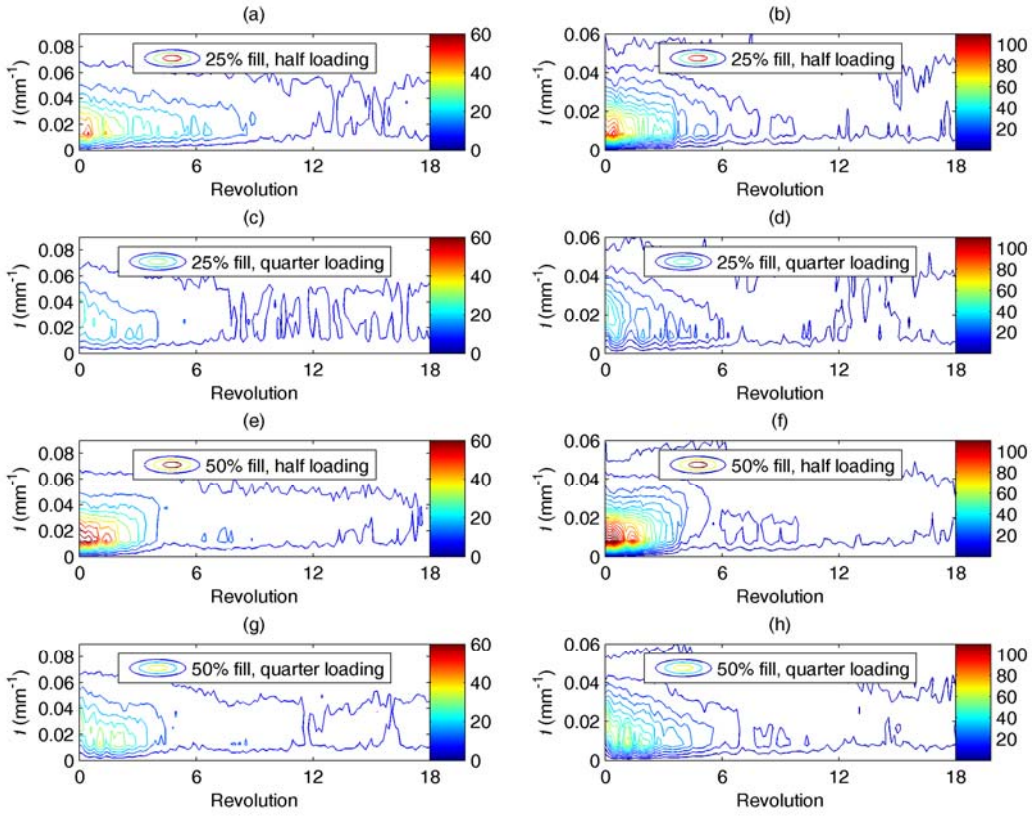

Figure 7.6 Variance spectrum decay contours of cohesive segregating mixing cases. The left four plots (a, c, e, g) show the 80 mm scale mixing cases. The right four plots (b, d, f, h) show the 120 mm scale mixing cases. The same level step of color map is used for all contours to show the spectrum profile of segregation when steady state is reached.

Figure 7.6 shows the overall variance spectrum decay contours of cohesive segregating mixing cases. In order to visualize spectrum profiles of cohesive segregation, the same level step value of the color map (6 $mm^{3/2}$) is used for both scales. As previously, similar spectra decays are found when the contour regions at high amplitudes are compared. On the other hand, when steady state is reached, segregation can be observed, the intensity of which is mainly located in the frequency domain interval between 0.01 and 0.05 mm^{-1} for all mixing cases.

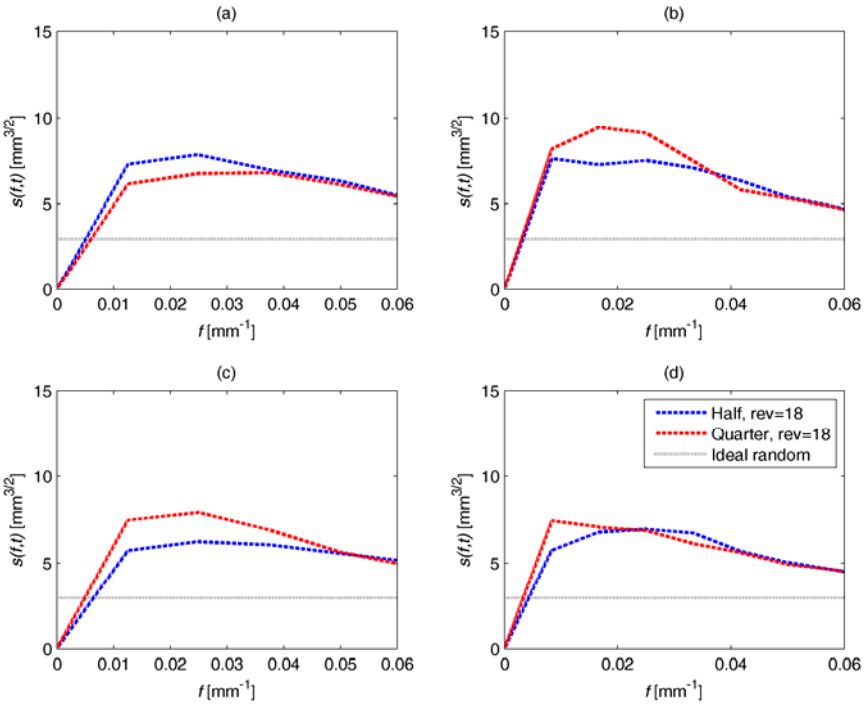

Figure 7.7 The steady state profiles of variance spectrum of the cohesive segregating mixing cases.

(a) 80 mm scale at 25% fill. (b) 120 mm scale at 25% fill. (c) 80 mm scale at 50% fill. (b) 120 mm scale at 50% fill. Half: half loading. Quarter: quarter loading. rev: revolution.

The steady state profiles of variance spectra are plotted in Figure 7.7. The black dot lines indicate the horizontal spectrum of an ideal random mixture. Due to the higher spectrum in the cohesive cases, variance values larger than the one calculated by binominal theorem will be observed. As Figure 7.7 shows, the steady state spectra of cohesive segregation are scarcely influenced by fill level, loading pattern or mixing scale. The corresponding snapshots of steady state mixture can be seen in Figure 7.8, where agglomerations with the same scale are found in all mixing cases.

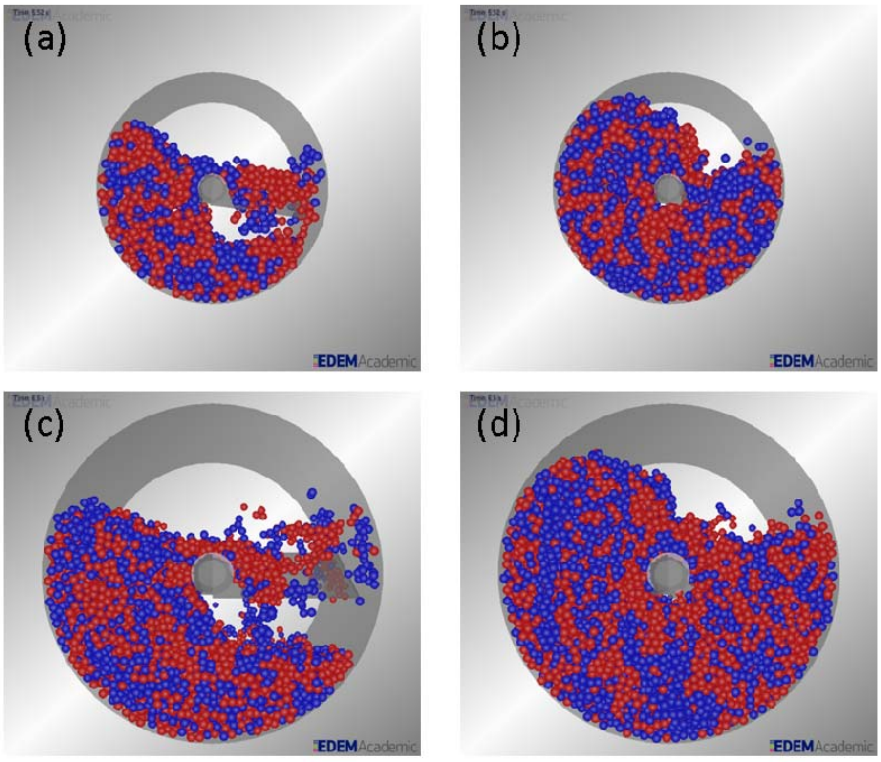

Figure 7.8 The snapshots of steady state mixture in the cohesive segregating mixing cases. (a) 80 mm scale at 25% fill. (b) 80 mm scale at 50% fill. (c) 120 mm scale at 25% fill. (b) 120 mm scale at 50% fill. Agglomerations of the same scale are observed for all four cases.

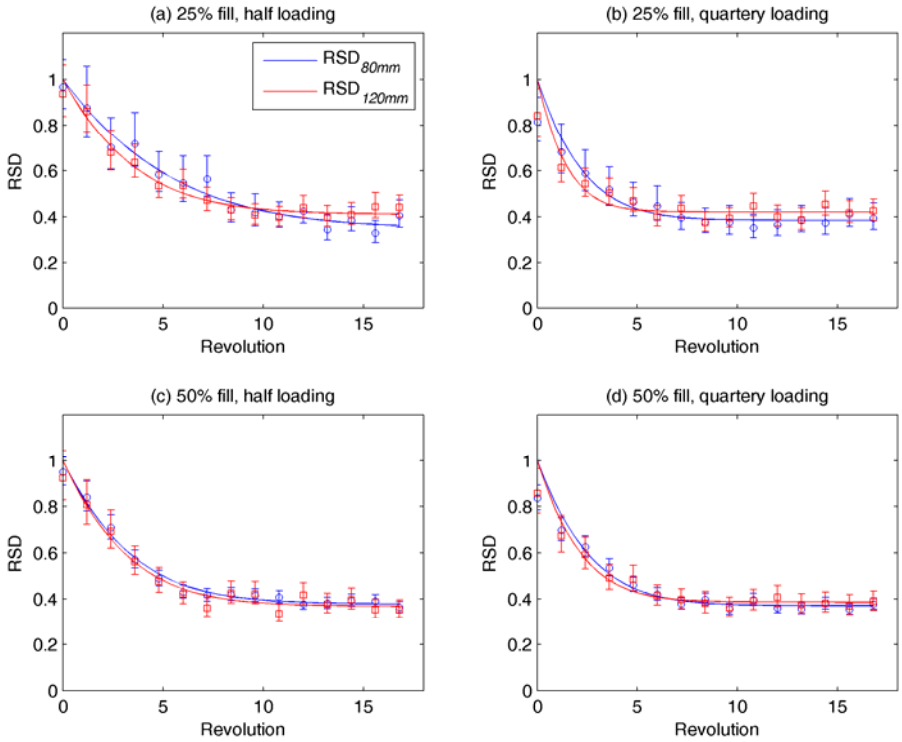

Figure 7.9 RSD-t decay curves measure at sampling size of 0.45 cm^3, cohesive segregating mixing cases.

(a) 25% fill, half loading. (b) 50% fill, quarter loading. (c) 50% fill, half loading. (d) 50% fill, quarter loading.

Similar decays of RSD curves are observed in Figure 7.9 for all cases in despite of some insignificant difference between fitted curves. Notice the larger value of RSD around 0.40 compared to the binominal theorem calculation (0.22) as has been discussed above. In sum, the scaled-up mixing cases of cohesive powders are similar to the original mixing cases in the current simulation design.

7.4.2 Axial blending

The axial blending of the two cases is shown in Figures 7-10. The plots in this figure are rescaled using the unit revolution instead of time for comparison purposes. Since the residence time distribution does not depend on loading pattern, only the cases of half loading are plotted. As illustrated, the RTD in non-segregating cases are similar for both fill levels, indicating good scaling up characteristics of non-segregating particles on axial mixing and motion. Larger RTDs of cohesive mixing is observed in the 80 mm scale mixing, while RTDs in the 120 mm scale mixing cases are similar to those in the non-segregating cases. Therefore, the effect of cohesion on the axial motion of particles is significant only when the scale of mixing space is small, under which condition the cohesive particles move much slower than the non-segregating particles. While the mean residence time is slightly shorter at 25% fill in non-segregating mixing cases, particles stay much longer in 80 mm scale mixing space in the cohesive cases, especially when the lower fill level is used. It is worth to note that the axial velocity measured in 120 mm scale is around 1.5 fold of that in the 80 mm scale due to the scale ratio of mixing space.

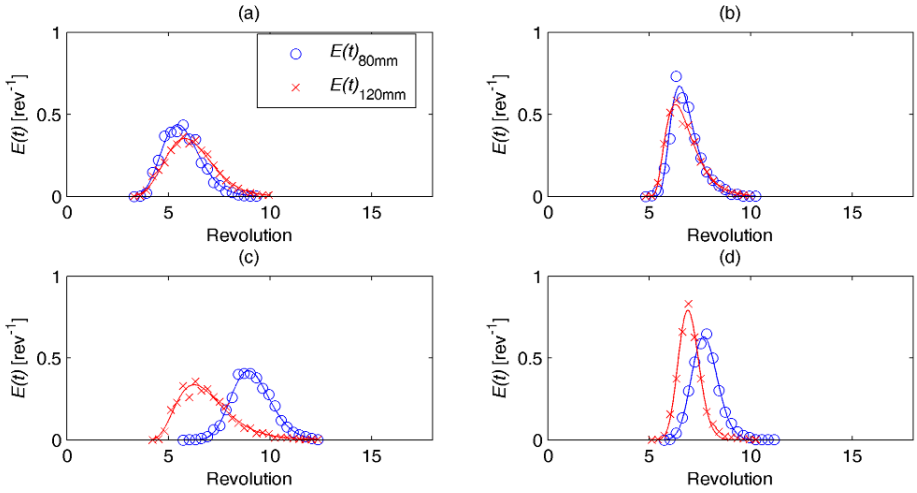

Figure 7.10 Residence time distribution of all mixing cases.

(a) Non-segregating cases, 25% fill. (b) Non-segregating cases at 50% fill. (c) Cohesive segregating cases, 25% fill. (d) Cohesive segregating cases, 50% fill. rev: revolution.

7.4.3 Flow rate evaluation

For similar mixing geometries with scale ratio k and constant Fourde number the flow rates can be estimated as follows:

$$r_2 = kr_1,\ l_2 = kl_1 \qquad 7\text{-}21$$

$$\omega_2 = k^{-0.5}\omega_1 \qquad 7\text{-}22$$

Since the mean residence time distribution measured by revolution ($\omega l/v_x$) is kept the same in the process of scaling up, it follows that:

$$v_{x2} = k^{0.5}v_{x1} \qquad 7\text{-}23$$

The scaling relationship of flow rate can then be derived using the formula $F = \pi v_x r^2$ and be expressed as follows:

$$F_2 = k^{2.5} F_1 \qquad 7\text{-}24$$

Therefore, when a four-fold scaling up is applied on the mixing apparatus, the flow rate of the larger continuous mixer is 32 fold of the original lab scale apparatus, which indicates a tremendous increase in production rate for the continuous powder mixing system. This shows the merit of using the model for continuous powder mixing on the scaling up characteristics.

Similar analysis can be performed on the batch mixing systems, where the production rate can be measured as $F = l^3 k_b$ where l^3 represent the batch volume and k_b the mixing rate. Since similar mixing rates, measured by the reciprocal of revolution (k_b / ω), are achieved, the scaling relationship of mixing rate is expressed as

$$k_{b2} = k^{-0.5} k_{b1} \qquad 7\text{-}25$$

As a result, a scaling up expression of production rate the same as equation (7-24) is derived for the case of batch mixing, indicating the inherent coincidence of batch and continuous mixing processes.

For the cohesive cases, equation (7-24) can be directly used for the scaling up of batch-like powder mixing process, due to the scaling relationship observed in Section 7.4.1. However, larger flow rate will be observed in the scaled-up continuous powder mixing process, due to a relatively fast axial velocity in that case. This effect should be considered in the design of scaling up strategy of cohesive mixing cases.

7.5 Summary

A new methodology based on the concept of variance spectrum has been developed for studying the scale-up of powder mixing in continuous processes. The Lomb-Scargle

Periodogram technique widely applied in astronomical studies has been used to estimate the variance spectrum of unevenly distributed samples in powder mixing processes. The periodic section modeling, proposed in our previous work (Gao et al., 2012), permits us to consider the batch-like cross-sectional mixing and axial motion separately for the scale-up of continuous powder mixing process. Such quantitative investigations are used to clarify the effect of constant sampling size on mixing performance, and the effect of scaling up on both cross-sectional and axial mixing within continuous mixing. For the non-segregating mixing cases, similar scale-up characteristics are observed for both cross-sectional and axial mixing in our simulation results. While a satisfying principle of similarity leads to similar decay contours of variance spectra, a sampling size much smaller than the scales of both apparatuses should be used to achieve similar mixing performance measurements. When non-segregating materials are processed, a 2.5 fold increase in production rate is obtainable for the scale-up of continuous powder mixing. However, in processes where cohesive materials segregate due to a tendency to agglomerate, an even larger increase of flow rate is expected. This results from the effect of cohesion on axial motion especially when the scale of the mixing process is small. Our preliminary simulation results illustrate that the proposed analysis can be used to achieve a successful scale-up strategy for continuous powder mixing processes.

Chapter 8

Conclusions and future Perspectives

8.1 Summary

In this dissertation, a novel predictive model is proposed first to provide strategies and guidance on addressing design, scale-up, and improvement issues in continuous powder blending process. The two main components of continuous blending are considered separately. Fourier series is employed in clarifying the attenuation of feeding fluctuation in the axial blending component. Feeding variance spectrum and blender filtering ability are applied to describe the performance of the feeder blender integration, instead of the fluctuation variance and the residence time distribution commonly used in conventional investigations. An efficient estimation strategy is developed to improve the axial blending when the integrated system is not in its optimal performance. By coupling the continuous blending performance with the batch-like blending with a similar geometry, the periodic section modeling is developed to capture the transitional status in the cross-sectional blending component. The residence time distribution in the continuous blender is used to predict the continuous blending performance from blending process in the periodic section. For both segregating and non-segregating blending cases, designed simulations show accurate predictions by using this model, and indicate that the mean residence time and the batch-like blending rate in the periodic section are the key indices of the cross-sectional blending component.

Due to recent development on powder feeding systems, variability on material flow was significantly reduced in pharmaceutical manufacturing. The cross-sectional blending

component is more significant affecting blending performance than the axial blending component and is focused in this dissertation. In order to apply the knowledge of batch blender in the design and improvement of continuous blender, performance similarity between continuous and similar batch systems is investigated. We use Discrete Element Method to investigate this issue. Mixing and flow of particles are examined in simple geometries consisting of a cylindrical cross-section agitated by impellers. End walls and symmetric blade pairs of the "alternate" blade patterns lead to faster mixing. Non-symmetric elemental systems display both increased fill level uniformity and similar mixing performance for both blade patterns. It demonstrates the need for caution when attempting to use batch mixing information to estimate the cross-sectional mixing rate of continuous powder mixers.

The effects of operation and geometry are examined on two key indices of continuous blending: axial velocity and local mixing rate of the mixture. When the local mixing rate improves at low fill level and high blade speed, particles also move faster in the axial direction and reside for a shorter time inside the mixer. This trade-off between ascending local mixing rate and descending residence time indicates a non-optimal overall blending performance even when the best operating condition is applied. Strategies are performed to further improve the blending performance, which are proposed by increasing the blade speed while keeping a constant axial velocity. These strategies guarantee that the variance decay rate along mixing axis is proportional to the blade speed in continuous blending processes. Dramatic improvements are observed when these strategies are applied in both simulations and experiments, which shows the merit of this work on design and optimization of continuous powder blending process.

Based on the developed predictive model, a quantitative scaling up strategy is introduced that allows the transition from lab to industrial scale. The proposed methodology is based on the variance spectrum analysis, and the residence time distribution, which are key indexes in capturing scale-up of the batch-like mixing, and scale-up of the axial mixing and motion, respectively. The constant-sample effect especially influential in scaling-up the manufacturing of pharmaceutical tablet is clarified by applying the development LSP variance spectrum analysis, which facilitates more comprehensive study on scale-up of blending systems.

8.2 Suggestion for future work

In this thesis, we focus on the development of a theoretical basis to characterize continuous powder blending. The theory can be further expanded to the modeling of other solid or liquid continuous unit operations by coupling the residence time distribution and the local reaction or processing rate in these units. Batch units can be constructed and used to understand the influence of geometry and operations, and improve the performance of the corresponding continuous units.

In addition to the non-segregation cases used in the model development in this work, segregating mixture should be examined where material properties such as cohesion, electrostatics, density, agglomeration influence the blending performance. Measurements should be taken not only on the residence time and variance decay rate, but also on the steady state variance of the mixture inside the blender at variance operation and geometry conditions. The understanding of powder properties can lead to useful guidance to further improve blender design and define optimal operation for the blending of practical pharmaceutical powders.

Reference

Abdi, H., 2010. Partial least squares regression and projection on latent structure regression (PLS Regression). Wiley Interdisciplinary Reviews: Computational Statistics 2, 97-106.

Abouzeid, A.Z.M., Fuerstenau, D.W., Sastry, K.V., 1980. Transport behavior of particulate solids in rotary drums: scale-up of residence time distribution using the axial dispersion model. Powder Technology 27, 241-250.

Abouzeid, A.Z.M., Mika, T.S., Sastry, K.V., Fuerstenau, D.W., 1974. The influence of operating variables on the residence time distribution for material transport in a continuous rotary drum. Powder Technology 10, 273-288.

Alexander, A., Muzzio, F., 2005. Batch Size Increase in Dry Blending and Mixing, Pharmaceutical Process Scale-Up, Second Edition. Informa Healthcare, pp. 161-180.

Alexander, A., Shinbrot, T., Johnson, B., Muzzio, F.J., 2004. V-blender segregation patterns for free-flowing materials: effects of blender capacity and fill level. International Journal of Pharmaceutics 269, 19-28.

Alexander, A., Shinbrot, T., Muzzio, F.J., 2002. Scaling surface velocities in rotating cylinders as a function of vessel radius, rotation rate, and particle size. Powder Technology 126, 174-190.

Arratia, P.E., Duong, N.-h., Muzzio, F.J., Godbole, P., Reynolds, S., 2006. A study of the mixing and segregation mechanisms in the Bohle Tote blender via DEM simulations. Powder Technology 164, 50-57.

Averbuch, A., Shkolnisky, Y., 2003. 3D Fourier based discrete Radon transform. Applied and Computational Harmonic Analysis 15, 33-69.

Babu, P., Stoica, P., 2010. Spectral analysis of nonuniformly sampled data - a review. Digital Signal Processing 20, 359-378.

Beaudry, J.P., 1948. Blender efficiency. Chemical Engineer 55, 112-113.

Bertrand, F., Leclaire, L.A., Levecque, G., 2005. DEM-based models for the mixing of granular materials. Chemical Engineering Science 60, 2517-2531.

Brone, D., Alexander, A., Muzzio, F.J., 1998. Quantitative characterization of mixing of dry powders in V-blenders. AIChE Journal 44, 271-278.

Brone, D., Muzzio, F.J., 2000. Enhanced mixing in double-cone blenders. Powder Technology 110, 179-189.

Brone, D., Wightman, C., Connor, K., Alexander, A., Muzzio, F.J., Robinson, P., 1997. Using flow perturbations to enhance mixing of dry powders in V-blenders. Powder Technology 91, 165-172.

Danckwerts, P.V., 1953. Continuous flow systems : Distribution of residence times. Chemical Engineering Science 2, 1-13.

Danckwerts, P.V., Sellers, S.M., 1951. The effect of hold up and mixing on a stream of fluctuating composition. Industrial Chemist 27, 395.

Ding, Y.L., Forster, R.N., Seville, J.P.K., Parker, D.J., 2001. Scaling relationships for rotating drums. Chemical Engineering Science 56, 3737-3750.

Dittrich, C.J., Mutsers, S.M.P., 2007. On the residence time distribution in reactors with non-uniform velocity profiles: The horizontal stirred bed reactor for polypropylene production. Chemical Engineering Science 62, 5777-5793.

Dubey, A., Sarkar, A., Ierapetritou, M., Wassgren, C.R., Muzzio, F.J., 2011. Computational Approaches for Studying the Granular Dynamics of Continuous Blending Processes, 1 – DEM Based Methods. Macromolecular Materials and Engineering 296, 290-307.

Foster, G., 1995. The cleanest Fourier spectrum. ASTRONOMICAL JOURNAL 109, 1889-1902.

Gao, Y., Ierapetritou, M., Muzzio, F., 2011a. Investigation on the effect of blade patterns on continuous solid mixing performance. The Canadian Journal of Chemical Engineering 89, 969-984.

Gao, Y., Ierapetritou, M., Muzzio, F., 2012. Periodic section modeling of convective continuous powder mixing processes. AIChE Journal 58, 69-78.

Gao, Y., Muzzio, F., Ierapetritou, M., 2011b. Characterization of feeder effects on continuous solid mixing using fourier series analysis. AIChE Journal 57, 1144-1153.

Gao, Y., Vanarase, A., Muzzio, F., Ierapetritou, M., 2011c. Characterizing continuous powder mixing using residence time distribution. Chemical Engineering Science 66, 417-425.

Geng, F., Yuan, Z., Yan, Y., Luo, D., Wang, H., Li, B., Xu, D., 2009. Numerical simulation on mixing kinetics of slender particles in a rotary dryer. Powder Technology 193, 50-58.

Gilliland, R.L., Baliunas, S.L., 1987. Objective characterization of stellar activity cycles: I. Methods and solar cycle analyses, Astrophysical Journal, pp. 766-781.

Goldsmith, P.L., 1966. The Theoretical Performance of a Semi-Continuous Blending System. The Statistician 16, 227-251.

Harris, A.T., Davidson, J.F., Thorpe, R.B., 2002a. A novel method for measuring the residence time distribution in short time scale particulate systems. Chemical Engineering Journal 89, 127-142.

Harris, A.T., Davidson, J.F., Thorpe, R.B., 2003a. The influence of the riser exit on the particle residence time distribution in a circulating fluidised bed riser. Chemical Engineering Science 58, 3669-3680.

Harris, A.T., Davidson, J.F., Thorpe, R.B., 2003b. Particle residence time distributions in circulating fluidised beds. Chemical Engineering Science 58, 2181-2202.

Harris, A.T., Thorpe, R.B., Davidson, J.F., 2002b. Stochastic modelling of the particle residence time distribution in circulating fluidised bed risers. Chemical Engineering Science 57, 4779-4796.

Harvey, A.D., Lee, C.K., Rogers, S.E., 1995. Steady-state modeling and experimental measurement of a baffled impeller stirred tank. AIChE Journal 41, 2177-2186.

Harwood, C.F., Walanski, K., Luebcke, E., Swanstrom, C., 1975. The performance of continuous mixers for dry powders. Powder Technology 11, 289-296.

Hobbs, D.M., Swanson, P.D., Muzzio, F.J., 1998. Numerical characterization of low Reynolds number flow in the Kenics static mixer. Chemical Engineering Science 53, 1565-1584.

Hocke, K., Kämpfer, N., 2009. Gap filling and noise reduction of unevenly sampled data by means of the Lomb-Scargle periodogram. Atmospheric Chemistry and Physics 9, 4197-4206.

Horio, M., Nonaka, A., Sawa, Y., Muchi, I., 1986. A new similarity rule for fluidized bed scale-up. AIChE Journal 32, 1466-1482.

Ingram, A., Seville, J.P.K., Parker, D.J., Fan, X., Forster, R.G., 2005. Axial and radial dispersion in rolling mode rotating drums. Powder Technology 158, 76-91.

Johnson, P.C., Jackson, R., 1987. Frictional–collisional constitutive relations for granular materials, with application to plane shearing. Journal of Fluid Mechanics 176, 67-93.

Johnstone, R.W., Thring, M.W., 1957. Pilot plants, models and scale-up methods in chemical engineering. MacGraw-Hill, New York.

Jones, J.R., Parker, D.J., Bridgwater, J., 2007. Axial mixing in a ploughshare mixer. Powder Technology 178, 73-86.

Larochette, M., Graebling, D., Nasri, D., Léonardi, F.d.r., 2009. Optimization of the Polymer Foam Process by the Residence Time Distribution Approach. Industrial & Engineering Chemistry Research 48, 4884-4891.

Laurent, B.F.C., Bridgwater, J., 2002. Influence of agitator design on powder flow. Chemical Engineering Science 57, 3781-3793.

Levenspiel, O., Smith, W.K., 1957. Notes on the diffusion-type model for the longitudinal mixing of fluids in flow. Chemical Engineering Science 6, 227-235.

Lomb, N.R., 1976. Least-squares frequency analysis of unequally spaced data. Astrophysics and Space Science 39, 447-462.

Lopes, V.V., Menezes, J.C., 2005. Inferential sensor design in the presence of missing data: a case study. Chemometrics and Intelligent Laboratory Systems 78, 1-10.

Manas-Zloczower, I., 1994. Studies of mixing efficiency in batch and continuous mixers. Rubber chemistry and technology 67, 504-528.

Marikh, K., Berthiaux, H., Gatumel, C., Mizonov, V., Barantseva, E., 2008. Influence of stirrer type on mixture homogeneity in continuous powder mixing: A model case and a pharmaceutical case. Chemical Engineering Research and Design 86, 1027-1037.

Marikh, K., Berthiaux, H., Mizonov, V., Barantseva, E., 2005. Experimental study of the stirring conditions taking place in a pilot plant continuous mixer of particulate solids. Powder Technology 157, 138-143.

Marikh, K., Berthiaux, H., Mizonov, V., Barantseva, E., Ponomarev, D., 2006. Flow Analysis and Markov Chain Modelling to Quantify the Agitation Effect in a Continuous Powder Mixer. Chemical Engineering Research and Design 84, 1059-1074.

Markström, P., Berguerand, N., Lyngfelt, A., 2010. The application of a multistage-bed model for residence-time analysis in chemical-looping combustion of solid fuel. Chemical Engineering Science 65, 5055-5066.

Martínez-Delgadillo, S.A., Mollinedo-Ponce, H., Mendoza-Escamilla, V., Barrera-Díaz, C., 2010. Residence time distribution and back-mixing in a tubular electrochemical reactor operated with different inlet flow velocities, to remove Cr(VI) from wastewater. Chemical Engineering Journal 165, 776-783.

McTait, G.E., Scott, D.M., Davidson, J.F., 1998. Residence time distribution of particles in rotary kilns, in: Fan, L.-S., Knowlton, T.M. (Eds.), Fluidization, Durango, Colorado, pp. 397-404.

Meijer, H.E.H., Elemans, P.H.M., 1988. The modeling of continuous mixers. Part I: The corotating twin-screw extruder, pp. 275-290.

Mindlin, R.D., 1949. Compliance of elastic bodies in contact. Journal of Applied Mechanics 71, 259-268.

Moakher, M., Shinbrot, T., Muzzio, F.J., 2000. Experimentally validated computations of flow, mixing and segregation of non-cohesive grains in 3D tumbling blenders. Powder Technology 109, 58-71.

Nauman, E.B., 2008. Residence Time Theory. Industrial & Engineering Chemistry Research 47, 3752-3766.

Pernenkil, L., Cooney, C.L., 2006. A review on the continuous blending of powders. Chemical Engineering Science 61, 720-742.

Portillo, P., Muzzio, F., Ierapetritou, M., 2008a. Using Compartment Modeling to Investigate Mixing Behavior of a Continuous Mixer. Journal of Pharmaceutical Innovation 3, 161-174.

Portillo, P., Muzzio, F.J., Ierapetritou, M.G., 2007. Hybrid DEM-compartment modeling approach for granular mixing. AIChE Journal 53, 119-128.

Portillo, P.M., Ierapetritou, M.G., Muzzio, F.J., 2008b. Characterization of continuous convective powder mixing processes. Powder Technology 182, 368-378.

Portillo, P.M., Ierapetritou, M.G., Muzzio, F.J., 2009. Effects of rotation rate, mixing angle, and cohesion in two continuous powder mixers—A statistical approach. Powder Technology 194, 217-227.

Portillo, P.M., Muzzio, F.J., Ierapetritou, M.G., Pantelides, W.M.a.C., 2006. Modeling and designing powder mixing processes utilizing compartment modeling, Computer Aided Chemical Engineering. Elsevier, pp. 1039-1044.

Portillo, P.M., Vanarase, A.U., Ingram, A., Seville, J.K., Ierapetritou, M.G., Muzzio, F.J., 2010. Investigation of the effect of impeller rotation rate, powder flow rate, and cohesion on powder flow behavior in a continuous blender using PEPT. Chemical Engineering Science 65, 5658-5668.

Poux, M., Fayolle, P., Bertrand, J., Bridoux, D., Bousquet, J., 1991. Powder mixing: Some practical rules applied to agitated systems. Powder Technology 68, 213-234.

Ralf Weineköter, L.R., 1995. Continuous Mixing of Fine Particles. Particle and Particle Systems Characterization 12, 46-53.

Reiss, R., Wojsznis, W., Wojewodka, R., 2010. Partial least squares confidence interval calculation for industrial end-of-batch quality prediction. Chemometrics and Intelligent Laboratory Systems 100, 75-82.

Risken, H., 1996. The Fokker-Planck Equation: Methods of Solution and Applications, 2 ed. Springer.

Roberts, D.H.L., J.; Dreher, J. W., 1987. Time Series Analysis with Clean - Part One - Derivation of a Spectrum. ASTRONOMICAL JOURNAL 93, 968 -989.

Sarkar, A., Wassgren, C., 2010. Continuous blending of cohesive granular material. Chemical Engineering Science 65, 5687-5698.

Sarkar, A., Wassgren, C.R., 2009. Simulation of a continuous granular mixer: Effect of operating conditions on flow and mixing. Chemical Engineering Science 64, 2672-2682.

Savage, S.B., Hutter, K., 1989. The motion of a finite mass of granular material down a rough incline. Journal of Fluid Mechanics 199, 177-215.

Scargle, J.D., 1982. Studies in astronomical time series analysis. II - Statistical aspects of spectral analysis of unevenly spaced data. Astrophysical Journal 263, 835 -853.

Sherritt, R.G., Chaouki, J., Mehrotra, A.K., Behie, L.A., 2003. Axial dispersion in the three-dimensional mixing of particles in a rotating drum reactor. Chemical Engineering Science 58, 401-415.

Shin, S.H., Fan, L.T., 1978. Characterization of solids mixtures by the discrete fourier transform. Powder Technology 19, 137-146.

Stoica, P., Jian, L., Hao, H., 2009. Spectral Analysis of Nonuniformly Sampled Data: A New Approach Versus the Periodogram. Signal Processing, IEEE Transactions on 57, 843-858.

Sudah, O.S., Chester, A.W., Kowalski, J.A., Beeckman, J.W., Muzzio, F.J., 2002a. Quantitative characterization of mixing processes in rotary calciners. Powder Technology 126, 166-173.

Sudah, O.S., Coffin-Beach, D., Muzzio, F.J., 2002b. Effects of blender rotational speed and discharge on the homogeneity of cohesive and free-flowing mixtures. International Journal of Pharmaceutics 247, 57-68.

Sudah, O.S., Coffin-Beach, D., Muzzio, F.J., 2002c. Quantitative characterization of mixing of free-flowing granular material in tote (bin)-blenders. Powder Technology 126, 191-200.

Vanarase, A.U., Alcalà, M., Jerez Rozo, J.I., Muzzio, F.J., Romañach, R.J., 2010. Real-time monitoring of drug concentration in a continuous powder mixing process using NIR spectroscopy. Chemical Engineering Science 65, 5728-5733.

Vanarase, A.U., Muzzio, F.J., 2011. Effect of operating conditions and design parameters in a continuous powder mixer. Powder Technology 208, 26-36.

Wang, R.H., Fan, L.T., 1974. Methods for scaling-up tumbling. Chemical Engineering 81, 88-94.

Weineköter, R., Reh, L., 1995. Continuous Mixing of Fine Particles. Particle and Particle Systems Characterization 12, 46-53.

Wightman, C., Moakher, M., Muzzio, F.J., Walton, O., 1998. Simulation of flow and mixing of particles in a rotating and rocking cylinder. AIChE Journal 44, 1266-1276.

Wightman, C., Muzzio, F.J., 1998. Mixing of granular material in a drum mixer undergoing rotational and rocking motions I. Uniform particles. Powder Technology 98, 113-124.

Williams, J.C., 1976. Continuous mixing of solids. A review. Powder Technology 15, 237-243.

Williams, J.C., Rahman, M.A., 1972a. Prediction of the performance of continuous mixers for particulate solids using residence time distributions : Part II. Experimental. Powder Technology 5, 307-316.

Williams, J.C., Rahman, M.A., 1972b. Prediction of the performance of continuous mixers for particulate solids using residence time distributions Part I. Theoretical. Powder Technology 5, 87-92.

Williams, J.C., Richardson, R., 1982. The continuous mixing of segregating particles. Powder Technology 33, 5-16.

Wold, S., Sjöström, M., Eriksson, L., 2001. PLS-regression: a basic tool of chemometrics. Chemometrics and Intelligent Laboratory Systems 58, 109-130.

Yeh, A.-I., Jaw, Y.-M., 1998. Modeling residence time distributions for single screw extrusion process. Journal of Food Engineering 35, 211-232.

Zalc, J.M., Szalai, E.S., Muzzio, F.J., Jaffer, S., 2002. Characterization of flow and mixing in an SMX static mixer. AIChE Journal 48, 427-436.

Zechmeister, M., Kürster, M., 2009. The generalised Lomb-Scargle periodogram, pp. 577-584.

Zhang, C.-L., Feng, L.-F., Hoppe, S., Hu, G.-H., 2009. Residence time distribution: An old concept in chemical engineering and a new application in polymer processing. AIChE Journal 55, 279-283.

Zhou, Y.C., Yu, A.B., Stewart, R.L., Bridgwater, J., 2004. Microdynamic analysis of the particle flow in a cylindrical bladed mixer. Chemical Engineering Science 59, 1343-1364.

Ziegler, G.R., Aguilar, C.A., 2003. Residence time distribution in a co-rotating, twin-screw continuous mixer by the step change method. Journal of Food Engineering 59, 161-167.

CURRICULUM VITA

YIJIE GAO
Chemical and Biochemical Engineering Department
98 Brett Road, Piscataway, NJ 08854
Rutgers, The State University of New Jersey
Email: yijiegao2006@gmail.com

Education

2012 PhD Rutgers, The State University of New Jersey, Piscataway, NJ
2007 BS Tsinghua University, Beijing, China

Peer-reviewed Journal Publications

1. **Gao, Y.**, Ierapetritou, M., Muzzio, F., 2012. Periodic section modeling of convective continuous powder mixing processes. AIChE Journal 58, 69-78.
2. **Gao, Y.**, Muzzio, F., Ierapetritou, M., 2011. Characterization of feeder effects on continuous solid mixing using fourier series analysis. AIChE Journal 57, 1144-1153.
3. **Gao, Y.**, Vanarase, A., Muzzio, F., Ierapetritou, M., 2011. Characterizing continuous powder mixing using residence time distribution. Chemical Engineering Science 66, 417-425.
4. **Gao, Y.**, Ierapetritou, M., Muzzio, F., 2011. Investigation on the effect of blade patterns on continuous solid mixing performance. Canadian Journal of Chemical Engineering 89, 969-984.
5. Vanarase A., **Gao Y.**, Dubey A., Ierapetritou M., and Muzzio F.. "Chapter 9-2. Scale up of continuous blending", in Pharmaceutical Process Scale-Up, 3rd Ed., 2011. ISBN: 9781616310011.
6. **Gao, Y.**, Muzzio, F., Ierapetritou, M.. Optimizing continuous powder mixing processes using periodic section modeling. *Submitted to* Chemical Engineering Science *Feb 2012*.
7. **Gao, Y.**, Muzzio, F., Ierapetritou, M.. A review of the Residence Time Distribution (RTD) applications in solid unit operations. *Submitted to* Powder technology Technology *Feb 2012*.
8. **Gao, Y.**, Muzzio, F., Ierapetritou, M.. Scaling up strategy for continuous powder mixing process. *Submitted to* Powder technology *Apr 2012*.
9. **Gao, Y.**, Boukouvala, F., Engisch, B., Muzzio, F., Ierapetritou, M.. Continuous powder blending improvement using Projection to Latent Structure regression and experimental validation. *Manuscript in preparation*.